Hybrid Solar Cells from Polymers and Silicon Nanocrystals

A DISSERTATION
SUBMITTED TO THE FACULTY OF THE GRADUATE SCHOOL
OF THE UNIVERSITY OF MINNESOTA
BY

Chin-Yi Liu

IN PARTIAL FULFILLMENT OF THE REQUIREMENTS
FOR THE DEGREE OF
DOCTOR OF PHILOSOPHY

Uwe Kortshagen

December 2009

Acknowledgements

First and foremost, I would like to thank my adviser, Professor Uwe Kortshagen for taking a chance on me when I knew very little about photovoltaic systems at the start of my doctoral studies. I feel very fortunate to have had Professor Kortshagen as my adviser. I am grateful that he allowed me flexibility in conducting my research and his guidance is greatly appreciated. I also thank all of the members of my group whom I have had the pleasure of working with these past few years.

Thank you to Professor Aydil and Professor Frisbie from the Chemical Engineering department for allowing me to use their equipment for my research and for their input. Their kindness and generosity is greatly appreciated.

These years of study were made much easier and extremely entertaining with the help and support of my officemates Zachary Holman and Ryan Gresback. I thank them for their help and advice with lab equipment and experimentation. Discussions with them have helped me work through many difficult research quandaries and I look forward to working with them again in the future.

Many collaborators have helped me a great deal during my doctorate project and I would like to specifically thank Bryan Boudouris, Emil Enache-Pommer, Kurtis Leschkies, and Derek Stevens. I have been very lucky to work with them.

I would like to thank my parents for their continuous support and for encouraging me to further my education. Thank you as well to my future in-laws Dr. and Mrs. Ming Lee for providing me with a second home in California. I would also like to thank Diana, who has supported me from day one and has motivated me to succeed.

Last but not least, a special thanks to a friend who has helped me greatly throughout my education:

最後要特別感謝臺灣妙法寺上如下田師父在人生與學業上的幫助和教誨，讓我能完成學業和找到人生方向。

Abstract

This thesis is concerned with the application of silicon nanocrystals (Si NCs) in photovoltaic devices. Two types of novel solar cells, hybrid solar cells and Si NCs-only thin-film photovoltaic devices, have been developed. Hybrid solar cells are made from polymers and Si NCs. The first hybrid solar cells were fabricated by using poly-3(hexylthiophene) (P3HT) which has a good hole mobility and matches the energy band alignment of Si NCs. The solar cell performance of Si NCs/P3HT devices was studied as a function of the weight ratio of Si NCs/P3HT and Si NC size. Three groups of Si NCs were used in this study: Si NCs 3-5 nm in diameter, 5-9 nm in diameter, and 10-20 nm in diameter. The open-circuit voltage and short-circuit current increased by using the smallest size NCs due to the high surface-area-to-volume ratio and quantum confinement effect. Those results indicate that Si NCs are a good candidate as an electron acceptor in hybrid solar cell application.

To improve the efficiency of Si NCs/P3HT hybrid solar cells, we started to optimize the fabrication conditions by modification of the polymer concentration, usage of post-production heat treatment, and application of different metal electrodes. After optimization, a hybrid solar cell from 50wt% (weight ratio) Si NCs/P3HT annealed at 150 °C for 2 hours with aluminum (Al) electrodes had a power conversion efficiency of 1.47% with a fill factor of 0.47, short-circuit current of 3.8 mA/cm^2, and open-circuit voltage of 0.8 V under air mass 1.5 direct (AM 1.5D) one sun illumination. To understand the hole mobility of P3HT before and after post-production heat treatment, a hole-only device was fabricated by depositing gold (Au) electrodes, which block electron injection from the electrodes to Si NCs. The results suggest that the hole mobility of 50wt% Si NCs/P3HT film increases one order of magnitude after heat treatment, due to improved crystallinity in the P3HT, which can enhance hybrid solar cell efficiency.

Literature has reported that the compatibility of polymers and nanocrystals plays an important role in hybrid solar cell efficiency. Although P3HT is a good hole conductor and light absorber in solar cell applications, other polymers should be tested to find the best compatibility for Si NCs. Knowing this, P3HT was replaced by poly [2-methoxy-5-(3',7'-dimethyloctyloxy)-1,4-phenylenevinylene] (MDMO-PPV) in 3-5 nm Si

NCs/MDMO-PPV hybrid solar cells. Although Si NCs/MDMO-PPV devices have a higher open-circuit voltage than Si NCs/P3HT devices, the power conversion efficiency of Si NCs/MDMO-PPV devices is not as high as that of Si NCs/P3HT devices. To understand the reasons for the low efficiency from Si NCs/MDMO-PPV devices, the hole mobility of MDMO-PPV, energy band alignment between MDMO-PPV and Si NCs, and absorption spectrum of MDMO-PPV were studied and compared to those of P3HT. To measure the hole mobility of MDMO-PPV, Au electrodes were again utilized to block electron injection into the Si NCs. The results show that the hole mobility of MDMO-PPV is lower than that of P3HT. The absorption spectrum of MDMO-PPV (400-600 nm) is narrower than that of P3HT (400-650 nm) so that exciton generation in P3HT is more efficient than in MDMO-PPV under AM 1.5 conditions. Additionally, MDMO-PPV has a lower highest occupied molecular orbital level than P3HT so the efficiency of hole injection from Si NCs into MDMO-PPV may not be as efficient as for P3HT. These reasons explain why the efficiency of Si NCs/MDMO-PPV devices is not as good as Si NCs/P3HT devices.

From Si NC solution processing, we found that 10-20 nm bare Si NCs without any surface modification can form a stable cloudy colloid with 1,2-dichlorobenzene. This colloid can be spin-cast onto an ITO substrate to form a continuous and dense thin film. A Schottky photovoltaic device consisting of a single layer of intrinsic Si NCs was fabricated in a glove box to verify that films can be cast from colloid Si NCs. This photovoltaic device has a sandwich structure with a 250 nm Si NC layer between ITO and Al electrodes. Under AM 1.5D one sun illumination, the Si NC Schottky device showed a significant photovoltaic response with a power conversion efficiency of 0.02%, a fill factor of 0.26, short circuit-current density of 0.148 mA/cm^2, and open-circuit voltage of 0.51 V. This result suggests that the solution processing of bare Si NCs can be a new way to manufacture low-cost and high-quality silicon-based thin films.

Table of Contents

List of Tables

List of Figures

Chapter 1

Chapter 2

Chapter 3

Chapter 4

Chapter 6

Chapter 7

Chapter 1

Introduction

1.1 Background

Due to increasing demand for energy and concerns about global climate change, renewable energy sources are attracting a substantial amount of attention. The sun delivers approximately 1 gigawatt per square kilometer of energy to the earth's surface — the total solar power hitting the earth is thus almost 10,000 times more power than humans presently consume — and solar cells can convert this solar energy into usable electricity.

Silicon has dominated the solar cell market since the first inorganic crystalline silicon solar cell was reported to have a 6% sunlight-to-electricity power conversion efficiency (PCE) by Chapin in 1954 [1]. At present, commercial silicon solar cells can reach 10-20% PCE. However, current solar cell manufacturing processes require high temperatures, vacuum technologies, and high-grade materials, all of which increase cost. As a result, current commercial solar cells remain expensive compared to fossil fuels at around 25-50 cents per kilowatt-hour in the USA (2002) [2].

To reduce the costs of current solar energy technologies, researchers have developed plastic solar cells, also called organic solar cells, which are made from carbon-containing compounds. Plastic solar cells are usually made from a solution so that they can be printed in a process similar to newspaper printing, or sprayed onto surfaces, like paint. Print or spray processing can lower manufacturing costs by avoiding high temperature and high vacuum methods. The cost of organic materials used in plastic solar cells is economical and plastic solar cells are lightweight and flexible, allowing them to be integrated with articles of daily use, such as clothes. Due to these advantages, organic solar cells have become a popular research topic.

To complete an organic solar cell, two types of material, electron donors and electron acceptors, need to be combined to cause dissociation of the electron-hole pairs and produce electricity. Most semiconductor polymers are efficient electron donors and various electron acceptors have been reported for solar cell fabrication, including conjugated polymers, fullerenes, and inorganic nanocrystals. This thesis will focus on the application of nanocrystals in polymer matrices.

1.2 Polymer-Based Organic Solar Cells

1.2.1 Conjugated Polymer

Conjugated polymers are long carbon chains formed by a conjugated backbone composed of alternating double bonds, where the π electron orbitals are delocalized. A carbon atom has 6 electrons ($1s^2 2s^2 2p^2$) and can form localized sp^2 hybrid σ bonds with neighbor carbon atoms or hydrogen. The one-electron p orbital on the chains can form delocalized π bonding systems with a neighbor atom which has a free p orbital. The continuously overlapping π orbitals, which extend on the backbone of the polymer, can provide pathways for electron transport and force the polymer into a planar structure. A conjugated polymer example of poly (para-phenylene) is shown in Figure 1-1.

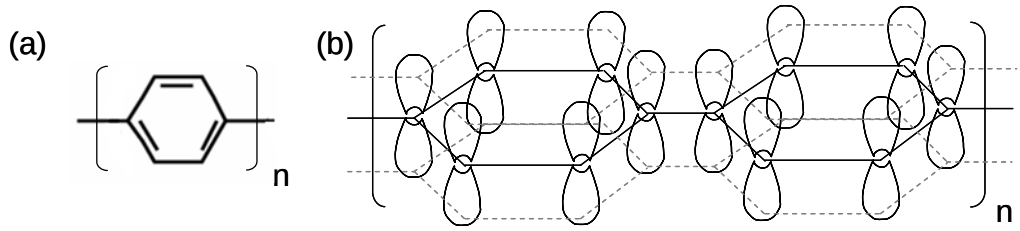

Figure 1-1. The conjugated bonding system of poly (para-phenylene) (a) two dimensional figure of the delocalized π bonding system (b) three dimensional figure of extending delocalized π bonds from $2p_z$ orbitals.

The electronic and optical properties of semiconductors are affected by their band gap. In organic semiconductors, the atoms are connected by covalent bonds which are usually formed from two electrons, one from each atom nearby. The band gap is defined as the difference in energy between the lowest point of the conduction band and the

highest point of the valence band. In conjugated polymers, the band gap is determined by the energy difference between the highest occupied and lowest unoccupied orbitals, where delocalized π electrons are located.

When light is absorbed by the conjugated polymer, an exciton is created by promoting an electron from the π orbital to the π* orbital. The exciton is charge neutral and consists of a pair of Coulomb-attracted electrons and holes. In semiconductors, excitons can be categorized into three types by the binding distance and energy between the electron and hole. From low- to high-binding energy order, they are Mott-Wannier excitons, charge-transfer excitons, and Frenkel excitons. A Mott-Wannier exciton is a weakly bound exciton in which the binding energy is typically smaller than 25 meV and not observed at room temperature [3]. In molecular crystals or polymers, the covalent binding energy within a molecule is stronger than the Van der Walls binding energy between molecules. Therefore, excitons in polymers can be considered as Frenkel excitons in which binding energy is typically on the order of 1 eV [3]. Charge-transfer excitons have less binding energy than Frenkel excitons and can be treated as a weakly-interacting electron-hole pair [4]. After light is absorbed, Frenkel excitons can be formed in the many units of a polymer [5, 6, 7, 8]. It is also possible to form charge-transfer excitons between several units on the polymer, called inter-chain excitons [6, 7, 8]. The scheme in Figure 1-2 illustrates different types of excitons.

Figure 1-3 shows common types of conjugated polymers. Due to the rigid π bonding structure, the conjugated polymers are insoluble in most solvents. To increase the solubility of polymers for solution-process applications, side chains are added to the polymers. Adding side chains also enhances the crystallization of polymers, which increases carrier mobility [9].

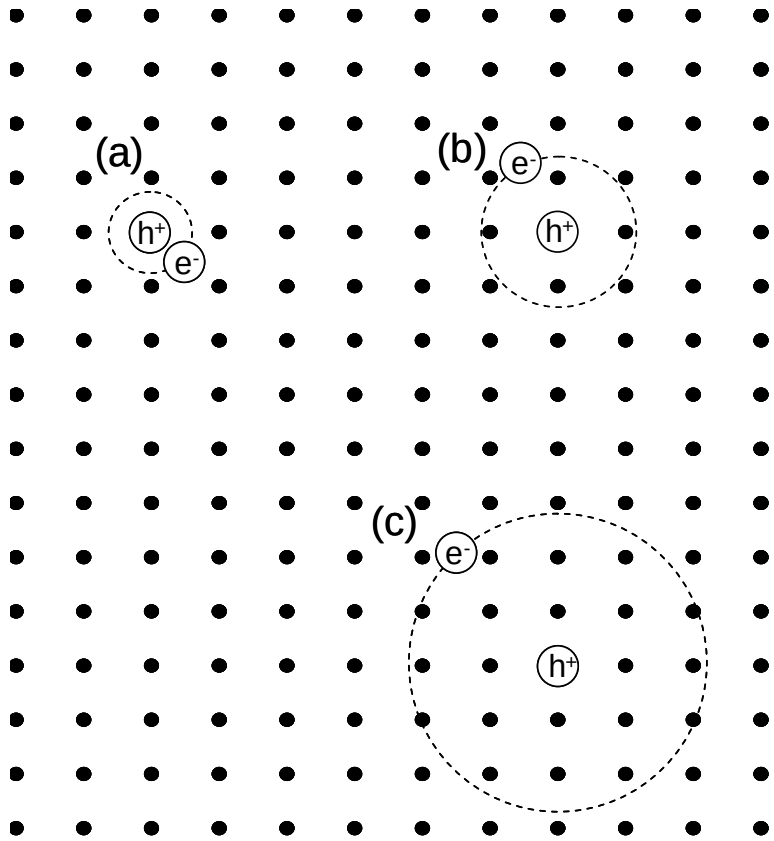

Figure 1-2. Different types of excitons: (a) Frenkel exciton, (b) charge-transfer exciton, (c) Mott-Wannier exciton [3].

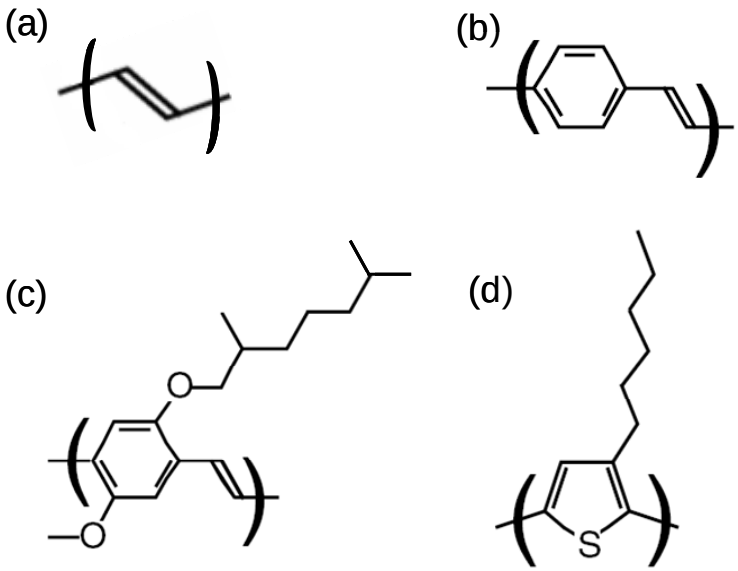

Figure 1-3. Common types of conjugated polymers: (a) trans-polyacetylene, (b) poly(p-phenylene-vinylene), (c) poly[2-methoxy-5-(3′,7′-dimethyloctyloxy)-1,4 -phenylene vinylene] (MDMO-PPV), (d) poly-3(hexylthiophene) (P3HT).

Although current manufacturing processes of semiconducting polymers can be conducted under atmospheric conditions, exposure to an ambient environment has a strong impact on the electrical characteristics of polymer-based devices. Literature reports that oxygen (O_2) [8] and ozone (O_3) [11] may dope polythiophene-based polymers and break the conjugated bond structure, changing their electrical characteristics. Oxygen is not a strong dopant in the absence of light because oxygen needs ultraviolet light (radiation < 240 nm) to form O_3. Ozone is highly reactive with conjugated bonds (unsaturated carbon-carbon bonds) and sulfurs in heterocycles [12]. Therefore, O_3 has a stronger impact than O_2 in ambient environments. The change in chemical structure of polythiophene-based polymers after exposure to O_3 is shown in Figure 1-4. Figure 1-4a shows how an O_3 molecule binds to a polymer backbone which may dissociate and form an S-O_2 group. Figure 1-4b illustrates the attachment of an S-O_2 group and an oxygen atom to carbons in the polymer. The additional oxygen atom formed by O_3 dissociation may also cleave the C-C conjugated bonds. The cleaving reaction is exothermic, so the chemical structures of broken backbones shown in Figure 1-4c are very stable. After O_3 reacts with polymers, negatively charged traps can be formed and hole mobility is reduced in the polymer film.

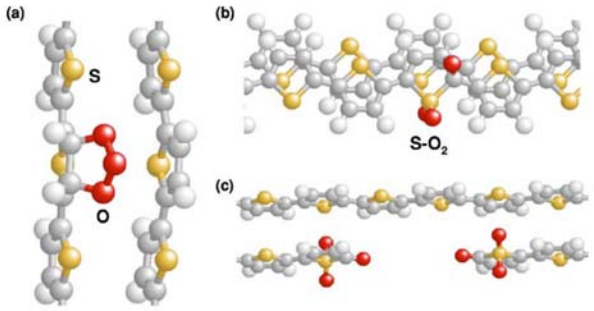

Figure 1-4. (a) O_3 molecule binding on a polythiophene-based polymer backbone. (b) S-O_2 group formation and oxygen atom attachment to carbons in the polythiophene-based polymer after O_3 dissociation. (c) The cleaving reaction of an oxygen atom breaks the conjugated bonds [11].

1.2.2 Organic Solar Cell Concepts

The scheme in Figure 1-5 illustrates how an organic solar cell functions. These devices are diode structures, typically containing light harvesting materials which act as

photon absorbers. In the solar cells, the photovoltaic materials absorb incoming photons which have energy greater than the band gap (E_g) to create an exciton by promotion of an electron from the highest occupied molecular orbital (HOMO) energy level to the lowest unoccupied molecular orbital (LUMO) energy level. The exciton can be considered as an electron-hole pair.

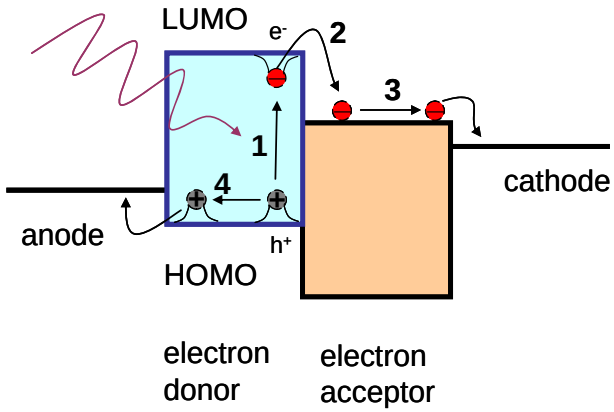

Figure 1-5. Heterojunction energy diagram of an organic solar cell displays (1) light absorption and promotion of an electron from the HOMO into LUMO to form an exciton in the electron donor layer; (2) exciton dissociation in the interface between the electron donor and acceptor and electron transfer from the electron donor into the electron acceptor; (3) electron transport from the electron acceptor to the cathode; (4) hole transport from the electron donor to the anode.

The average length which excitons can diffuse inside a polymer before recombination is called the exciton diffusion length. Typically, the exciton diffusion length is of the order of 5-10 nm, but also depends on the structure of the solar cell. For example, P3HT has ~10 nm exciton diffusion length. The binding energy of an exciton in polymers (> 100 meV) is relatively larger than in most of the inorganic semiconductors (<< 20 meV). Excitons created in bulk inorganic semiconductors may be dissociated with thermal excitations. To dissociate excitons in polymers, it is necessary to incorporate an electron acceptor semiconductor material with lower lying LUMO energy level. If excitons in the polymers can encounter the interface with the electron acceptor material within the exciton diffusion length, the electron can transfer to the electron acceptor material due to the energetically favorable energy level alignment. This process is called

exciton dissociation. After exciton dissociation, electron and holes are driven toward the electrodes by drift or diffusion.

1.2.3 Solar Cell Characterization

Characterization of efficiency is an important step for evaluation of solar cells. There are two basic types of efficiencies used to describe solar cells [13]. The first is power conversion efficiency (PCE), which is defined as the electrical power output per unit of incident sunlight power. The PCE of solar cells is characterized by the open-circuit voltage (V_{oc}), short-circuit current (I_{sc}), and fill factor (FF). Fill factor is defined as the ratio of a solar cell's maximum theoretical power output to its actual maximum power output. Figure 1-6 shows the current density-voltage response of a solar cell under illumination [14].

$$FF = \frac{P_m}{I_{sc} \cdot V_{oc}} \tag{1.1}$$

where P_m is the actual maximum power output.

Power conversion efficiency can be defined as

$$PCE = \frac{P_m}{P_0} = \frac{FF \cdot I_{sc} \cdot V_{oc}}{P_0} \tag{1.2}$$

where P_0 is the incident optical power.

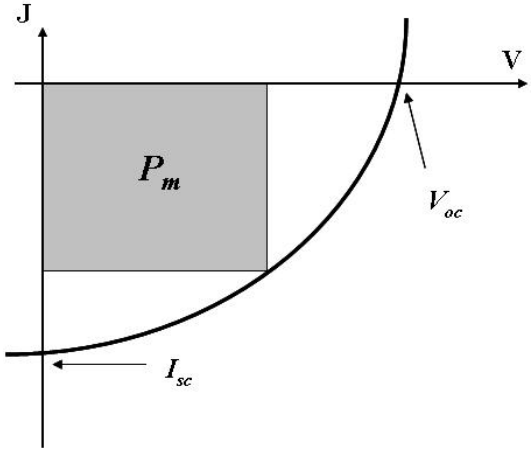

Figure 1-6. Current density-voltage response of a solar cell under illumination. The open-circuit voltage (V_{oc}), short-circuit current (I_{sc}), and actual maximum power output (P_m) are illustrated.

The second efficiency used to characterize solar cell performance is external quantum efficiency (EQE), which describes how many incident photons are converted into collected electrons and holes. External quantum efficiency, also know as the incident-photon-to-current-conversion efficiency (IPCE), can be defined as [15]

$$IPCE = \frac{n_e}{n_{ph}} = \eta_A \eta_{Diff} \eta_{Diss} \eta_{Tran} \eta_{cc} \tag{1.3}$$

where n_e is the number of photogenerated electrons and holes that are collected, n_{ph} is the number of incident photons, η_A is the photon absorption efficiency, η_{Diff} is the exciton diffusion efficiency, η_{Diss} is the exciton dissociation efficiency, η_{Tran} is the charge carrier transport efficiency, and η_{cc} is the charge collection efficiency. The five efficiencies are from the process of charge generation and transport which can be described in five steps. The five consecutive steps are shown in Figure 1-7. η_A is determined by the material optical absorption coefficient and the film thickness. η_{Diff} represents the exciton diffusing ability in the material before recombination. Excitons have a finite lifetime and they can vanish in different ways during the diffusion process. For example, the exciton can recombine to re-emit a photon, called radiative decay. η_{Diss} is the probability with which excitons are dissociated into free charge carriers. After holes and electrons are separated, the free charges must be transported toward the electrodes to produce photocurrent from the device. η_{Tran} describes carrier hopping and transporting events in the materials, which is affected by impurities or defects. Impurities and defects may trap the carriers and decrease the carrier transport efficiency. The farther the carriers travel, the higher the probability that they can be trapped. However, although a thin film may provide lower defect densities than a thick film, the absorption of the thin film is lower than the thick film. η_{cc} represents the charge injection ability from the material to the contacts which can be affected by the geometry, topology, interface formation, and work function.

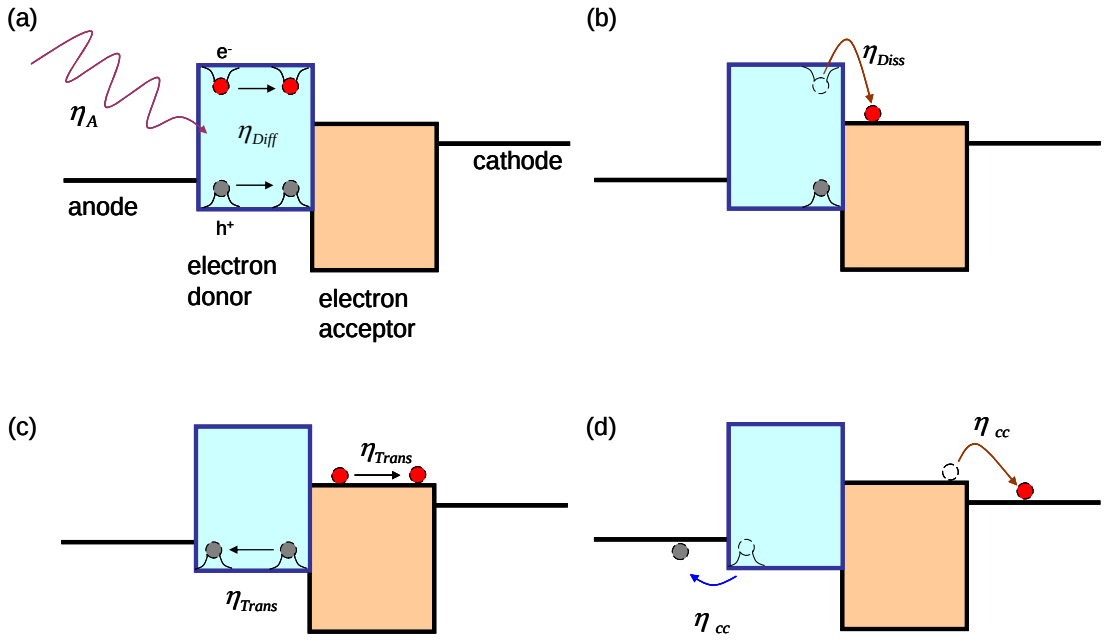

Figure 1-7. The process of photocurrent generation and transport. (a) photon absorption and exciton diffusion efficiency (b) exciton dissociation efficiency (c) carrier transport efficiency (d) charge collection efficiency [15].

Air mass 1.5 (AM 1.5) spectra are used extensively for characterization of solar cell performance. Air mass refers to the distance through the atmosphere which solar radiation passes to reach the ground. With the sun overhead (at zenith), the distance is AM 1.0. When the angle of sun from the zenith is 48.2° or 60.1°, the paths are called AM 1.5 or AM 2.0, respectively. The sun radiation paths are shown in Figure 1-8. The solar spectrum at the earth's surface combines light from several sources. Direct radiation is straight from the sun. Diffuse radiation comes from scattering from the sky and surroundings. There are two common AM 1.5 conditions (Figure 1-9), called AM 1.5G (global) and AM 1.5D (direct). AM 1.5G refers to the spectrum including direct radiation and diffuse radiation. AM 1.5D spectrum only considers direct radiation. The AM1.5G and AM 1.5D spectra are shown in Figure 1-10.

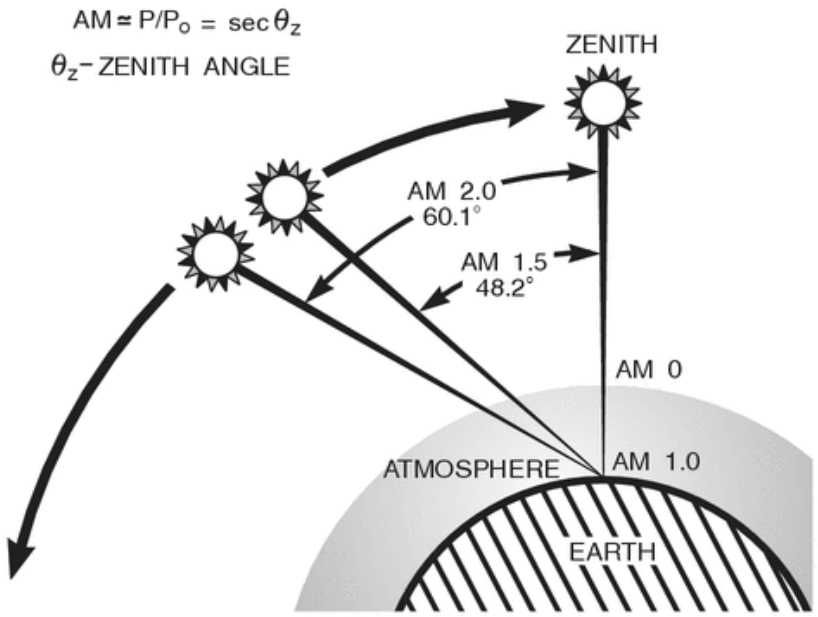

Figure 1-8. Schematic of path length change with zenith angle in air mass condition [16].

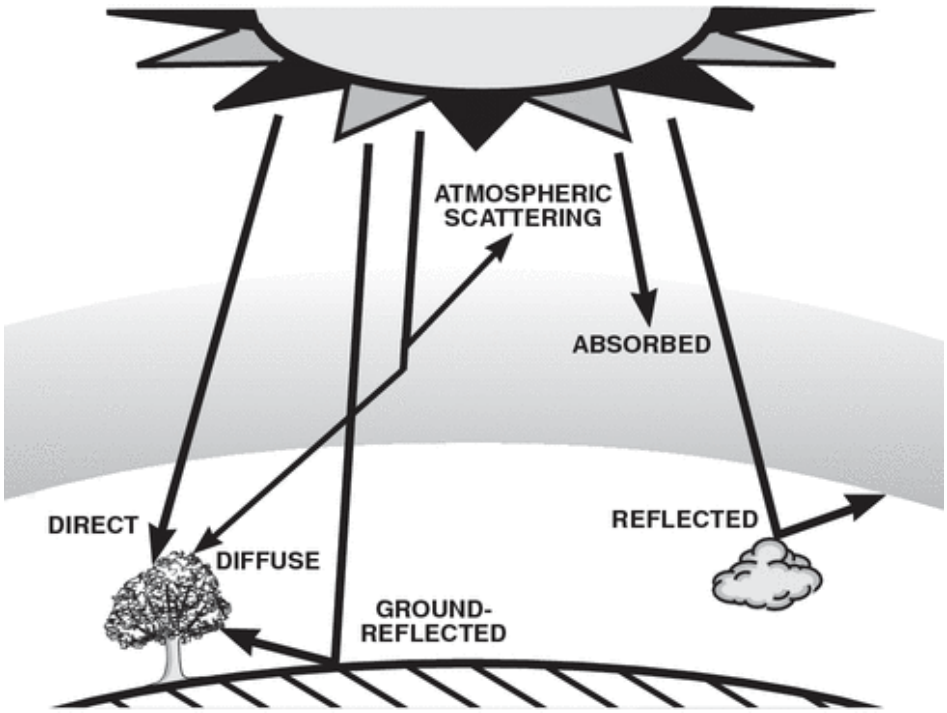

Figure 1-9. Direct radiation, diffuse radiation, and ground-reflected radiation of sun [16].

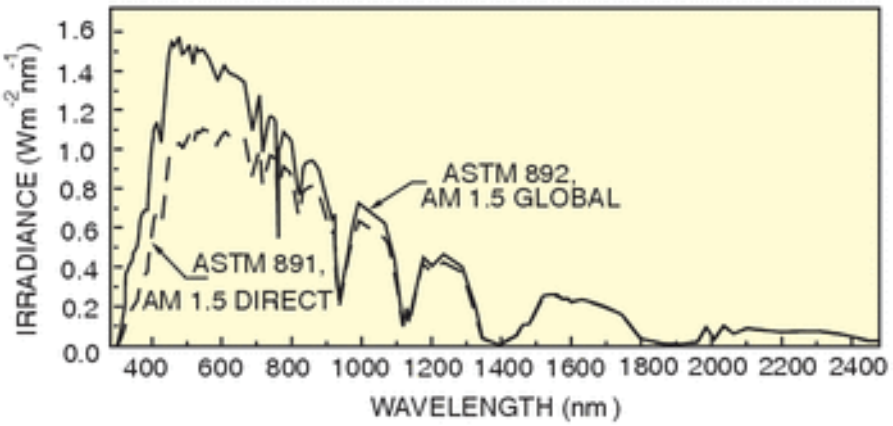

Figure 1-10. AM 1.5G and AM 1.5D solar spectra. ASTM refers to American Society for Testing and Materials [16].

1.2.4 Development of Organic Solar Cells

The first observation of photoconductivity in conjugated polymers was in the beginning of the 19th century [17, 18]. Conjugated polymers have many attractive properties for application in photovoltaic devices. Solution processing of conjugated polymers has great potential for low-cost manufacturing. Low-cost manufacturing may not come from the material cost, but can be achieved by printing or coating processes instead of wafer-based manufacturing. Also, the absorption spectra of conjugated polymers based on *trans*-poly(acetylene)(t-CH_x) match the solar spectrum well. Additionally, polymers are cost-effective in solar cells since their strong absorption means only thin films (< 300 nm) are required.

In 1984, the Schottky-diode structure solar cell (Figure 1-11a) made by t-CH_x was reported by Kanicki *et al.* [18]. This cell had a 0.1% power conversion efficiency (PCE) with 200 μA/cm^2 I_{sc}, 0.65 V V_{oc} and 0.3 FF under illumination of a 50 mW/cm^2 xenon white light lamp. There were also some groups reporting Schottky solar cells based on polythiophene [19, 20]. Those cells also did not show promising efficiencies. The excitons in the polymer are Frenkel excitons and due to their high binding energy, the excitons can only dissociate at the interface between the polymer and the metal contact. The exciton diffusion length is short (~10 nm) so that excitons produced far from the electrodes may not have a chance to separate before recombination. Additionally, a single

layer polymer film may not provide sufficient absorption. These reasons may explain why the Schottky-diode structure cannot have good performance.

To solve the aforementioned problems, a heterojunction bilayer structure (Figure 1-11b) is applied. The design of a heterojunction bilayer structure consists of an electron transport layer (n-type) and a subsequent hole transport material (p-type) between two electrodes, which allows charge separation only at the interface. This design can provide good carrier transport efficiency but has poor exciton diffusion and dissociation efficiencies. The additional advantage of a heterojunction device is that carrier transport and absorption in the two materials can be optimized separately. The exciton diffusion length inside the organic materials is on the order of 5-10 nm, and only the excitons generated nearby the interface have a chance to reach and dissociate at the interface. Thus, the heterojunction structure is exciton-diffusion limited. In 1992, Sariciftci *et al.* reported photoinducted electron transfer from a conducting polymer to buckminsterfullerene (C_{60}) [21]. Buckminsterfullerene was discovered by Kroto *et al.* in 1985 [22] and synthesized in bulk by Krätschmer *et al.* in 1990 [23]. Buckminsterfullerene is a strong electron acceptor and can take up to six electrons in its threefold degenerate LUMO [24]. In 1993, Sariciftci *et al.* reported a bilayer device using poly (2-methoxy, 5-(2′-ethyl) - hexyloxy-1,4-phenylenevinylene) (MEH-PPV) as a p-type material and buckminsterfullerene (C_{60}) as an n-type material. The layer of MEH-PPV was spun onto ITO-glass substrates and C_{60} was subsequently evaporated onto the MEH-PVV under vacuum to form the p-n heterojunction [25]. This method can avoid dissolving the first polymer during a second spin-coating. The MEH-PPV/C_{60} device showed 0.04% PCE with 0.5 V V_{oc}, 2.1 $\mu A/cm^2$ I_{sc}, and 0.48 FF under 1 mW/cm^2 light intensity at 514.5 nm.

In 2002, Drees *et al.* tried to create a graded polymer-fullerene interface by thermally controlled interdiffusion [26]. They spun 90 nm MEH-PPV on substrates and deposited a 100 nm C_{60} film subsequently. The composite film was annealed at the temperature around the glass transition temperature (T_g) of MEH-PVV to induce C_{60} to diffuse into the MEH-PPV film. The glass transition temperature of polymers is the temperature at which the amorphous portions of the polymer soften [27]. The crystalline portion of polymers remains crystalline at T_g. The device after annealing showed a

dramatic decrease in photoluminescence and increase in the short-circuit current. These results indicated that the increased proximity of C_{60} molecules to MEH-PPV led to the enhanced photovoltaic efficiency.

The best organic photovoltaic devices have been fabricated by using a polymer blend as the active layer, which is called a bulk heterojunction (Figure 1-11c). A bulk heterojunction structure has a similar electron donor-acceptor concept, but blends two materials to form the film and exciton dissociation interfaces are distributed through the entire film. Due to the decreased distance between the interfaces, exciton diffusion and exciton dissociation efficiencies can be higher than in heterojunction bilayer structures. In a bilayer structure, the electrode can selectively contact the electron donor and acceptor, but electrodes of bulk heterojunction structures contact the electron donor and acceptor at the same time. This causes an increase in the electron-hole recombination probability. In 1995, Yu *et al.* reported a 3.2% PCE device under 10 $\mu W/cm^2$ illumination by blending MEH-PPV and C_{60} [28]. In 2001, Shaheen *et al.* utilized screen printing technology to fabricate bulk heterojunction solar cells from a blend of MDMO-PPV and [6,6]-phenyl-C_{61}-butyric acid methyl ester (PCBM, a fullerene derivative of the C_{60} buckyball) [29]. When a MDMO-PPV/PCBM weight ratio of 1/4 was used, the device showed a 4.8% PCE under illumination of 488 nm monochromatic light. The corresponding V_{oc}, I_{sc}, and FF were 0.84 V, 3.16 mA/cm^2, and 0.44. In 2005, Ma *et al.* reported a 5% PCE P3HT/PCBM blend solar cell which had a weight ratio of 1/0.8 by applying a post-production thermal annealing process and using chlorobenzene, a high boiling point solvent [30]. Thermal processes can improve nanoscale morphology, crystallinity of P3HT, and interface quality between the metal electrode and active layers. The best device, which was annealed at 150 °C for 30 minutes, showed 9.5 mA/cm^2 I_{sc}, 0.63 V V_{oc}, 0.68 FF, and 5% PCE under 80 mW/cm^2 AM 1.5 illumination. The I-V curves of the best device reported by Ma *et al.* and a schematic of hole and electron transport are shown in Figure 1-12. Currently, Plextronics Inc. holds the world record of 5.4% PCE organic solar cells which is certified by National Renewal Energy Laboratory.

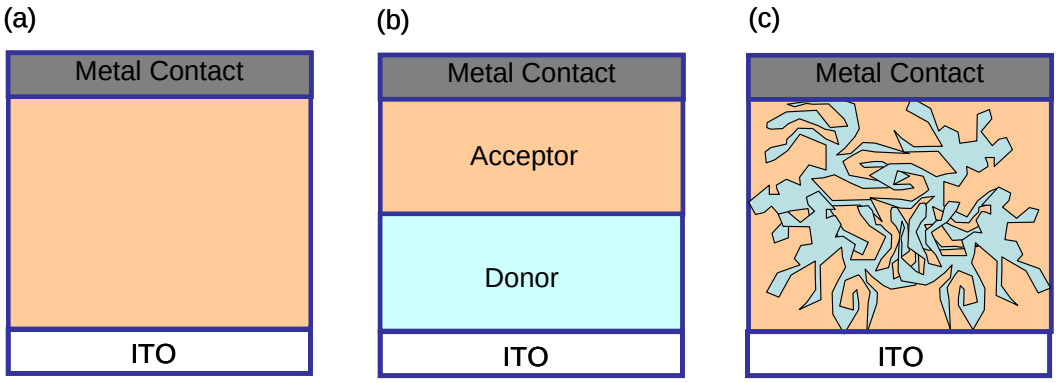

Figure 1-11. The most common organic solar cell structures. (a) Schottky-diode structure, (b) heterojunction bilayer structure, and (c) bulk heterojunction structure.

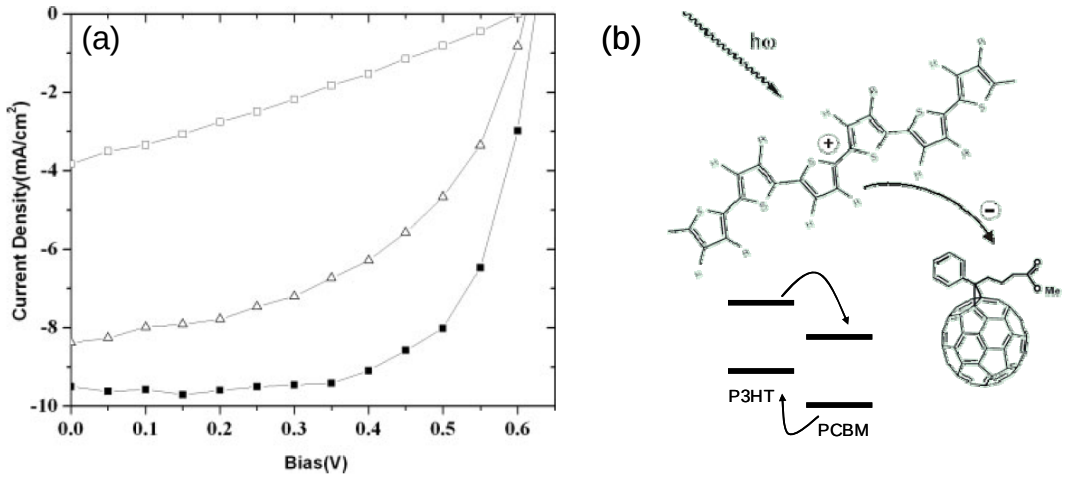

Figure 1-12. (a) I-V curves of P3HT/PCBM devices with different annealing temperatures under 80 mW/cm^2 AM 1.5 irradiation. Open triangles and filled squares represent devices with 70 °C and 150 °C annealing for 30 minutes, respectively. Open squares show the control device without annealing [30]. (b) Schematic of P3HT/PCBM solar cells. Most of the light is absorbed by the P3HT causing generation of excitons. The excitons can dissociate at the interface of P3HT and PCBM. The inset shows the energy diagram of P3HT and PCBM [31].

1.3 Hybrid Polymer/Nanocrystals Solar Cells

1.3.1 Semiconductor Nanocrystals

Semiconductor nanocrystals, also called quantum dots due to quantum confinement effects, refer to nanoparticles which are typically made up of hundreds to thousands of atoms and have different optical or electrical properties from the bulk semiconductors. Semiconductor nanocrystals started to attract attention in the mid 80's because of variation in their physical, spectroscopic, and thermodynamic properties, and possible use

in nanometer-scale devices [32, 33, 34]. For example, the melting temperatures of cadmium sulfide (CdS) nanocrystals can vary from 1600 down to 400 °C. The band gap of CdS nanocrystals can be tuned from 2.4 to 4 eV [35]. Property changes of nanocrystals are primarily caused by two mechanisms: free energy variation and quantum confinement. Nanocrystals which only contain a few hundred atoms have a very high surface-area-to-volume ratio and a large fraction of the atoms are at the surface atoms. In any material, the surface atoms make a proportional contribution to the total free energy. In bulk materials, the percentage of surface atoms is small, but the number of surface atoms is a large fraction of the total number of atoms in nanocrystals. Since a large fraction of nanocrystal atoms are on the surface, most of the surface atomic bonds are unsaturated and there is a large energy related to the surface. The free energy variation is the major reason for significant variation in thermodynamic properties of nanocrystals. In nanocrystals (solid phase), rigid-bonding can cause a high-energy edge and corner atoms. Less thermal energy needs to be added to melt the nanocrystals than bulk materials. In other words, the total surface energy can be reduced by melting. Therefore, melting temperature is depressed in nanocrystals. The melting temperature depression of CdS nanocrystals is shown in Figure 1-13 [36].

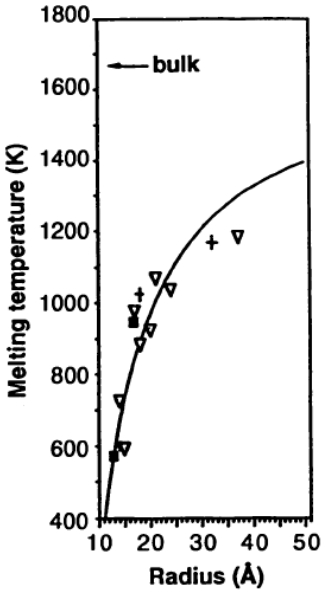

Figure 1-13. The melting temperature change in size-dependent CdS nanocrystals [36].

1.3.2 Quantum Confinement

The most notable property of semiconductor nanocrystals is the tunable absorption and emission spectra through quantum confinement effect. In bulk semiconductors, the band gap is defined as the energy required to promote an electron from the valance band to the conduction band (creating a hole in the valence band). The electron and hole are far enough apart so that the Coulomb attraction is negligible in bulk semiconductors. In nanocrystals, where dimensions are less than the Bohr radii of the electrons and holes, not only the periodic potential but also the interaction of the electron-hole pair should be considered. The quantum confinement of electrons and holes leads to a discrete density of states (Figure 1-14) and causes size-dependent electronic energy levels [37].

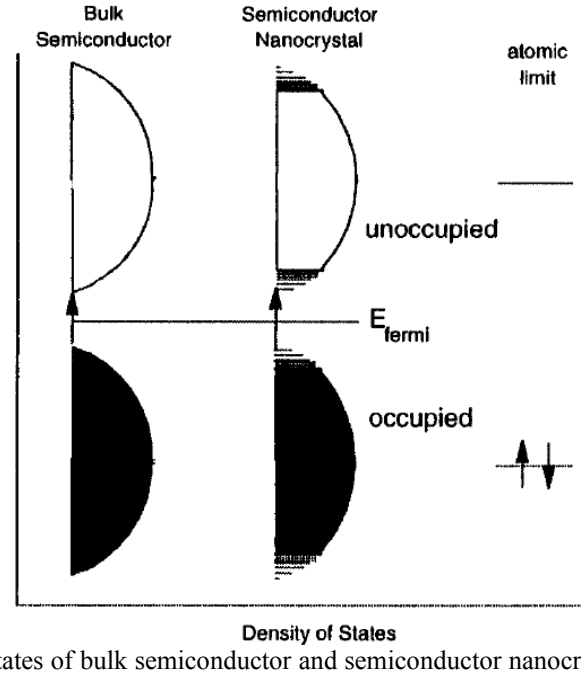

Figure 1-14. Density of states of bulk semiconductor and semiconductor nanocrystals. The Fermi level lies between the conduction and valence bands. The density of states becomes discrete at the band edges in semiconductor nanocrystals. The band gap increases when the size of semiconductor nanocrystals decreases [37].

An analytical expression which describes the change of band gap energy in a spherical nanocrystal with its radius was developed by L. E. Brus in 1996 [38]. The band gap energy of nanocrystals can be expressed as

$$E_g^{NC}(R) = E_g + \frac{\hbar^2 \pi^2}{2R^2}[\frac{1}{m_e} + \frac{1}{m_h}] - \frac{1.8e^2}{\varepsilon R} \quad (1.4)$$

where E_g is the bulk material band gap, $\hbar$ is the reduced Planck constant, R is the radius of the nanocrystal, m_e and m_h are the effective masses of electrons and holes, ε is the dielectric constant of the nanocrystal, and e is charge of electron. In the equation, the predominant energy term is the second term on the right-hand side, especially at small R. This term describes quantum confinement of the electrons and holes. The third term on the right-hand side of Equation 1.4 describes the Coulomb interaction of the electron-hole pairs [39]. As the radius of nanocrystals decreases, the quantum confinement term and electron-hole pair term both increase. When the nanocrystal size is sufficiently small, the quantum confinement term will dominate the equation. As a result, the band gap of a nanocrystal will increase with decreasing nanocrystal size. Despite the assumptions of this equation, this equation can clearly explain the effect of size on the optical properties of nanocrystals.

II-VI semiconductor nanocrystals are the best-characterized nanoparticles to date because of their simple solution-phase synthesis [40, 41, 42, 43]. Since II-VI semiconductors nanocrystals are direct band gap materials in which light absorption and emission do not need phonon interactions, they are widely used in devices, such as light-emitting [44] and photovoltaic [45] devices. The absorption of different sizes of cadmium selenide (CdSe) nanocrystals is shown in Figure 1-15a, and a photoluminescence spectrum of 35 Å diameter CdSe nanocrystals is shown in Figure 1-15b.

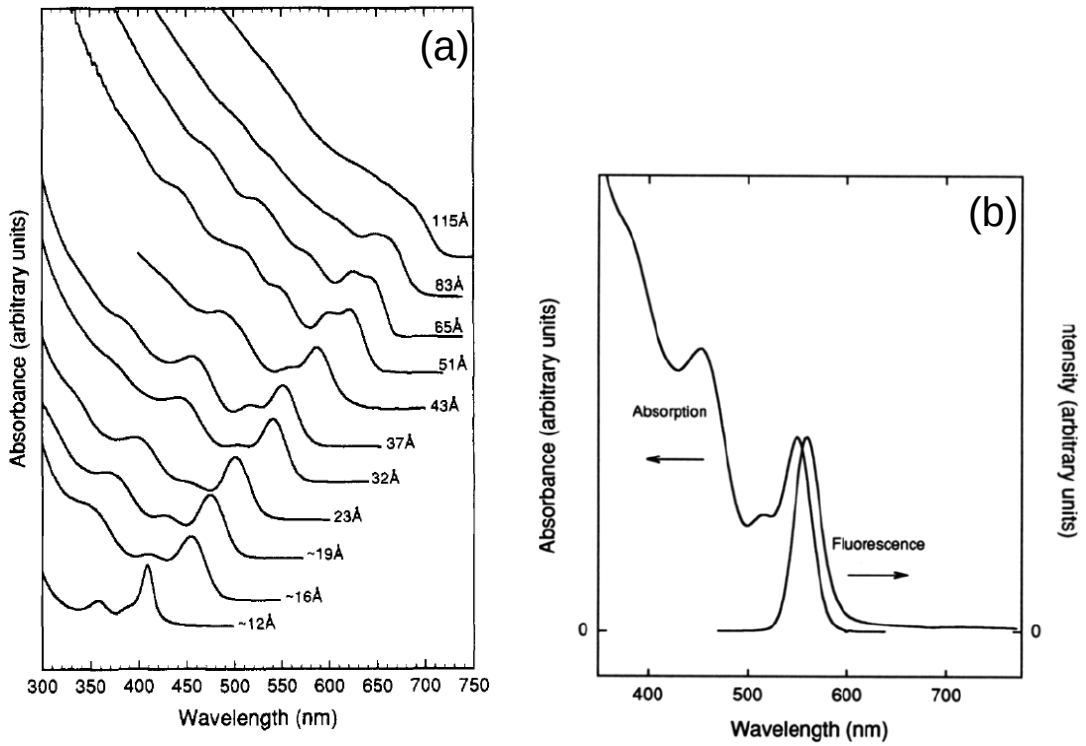

Figure 1-15. (a) Room temperature absorption spectra of different size CdSe nanocrystals from 12 Å to 115 Å (b) Room temperature absorption and photoluminescence spectra of 35 Å diameter CdSe nanocrystals [43].

Nanocrystals may open a new route for photovoltaic application due to their high surface-area-to-volume ratio, and tunable light absorption. One impressive application of nanocrystals is titanium dioxide (TiO_2) nanoparticles-dye sensitized photoelectrochemical solar cells, which have 7% PCE, made by O'regan *et al.* [46]. This cell utilized high surface-area-to-volume ratio TiO_2 nanocrystals to increase the exciton dissociation area. Because TiO_2 is a wide band gap material and cannot absorb sufficient light in the visible spectrum, the band gap tuning properties of the nanocrystals were not used. By optimizing the dye performance, Bai *et al.* reported a dye-sensitized solar of 11% PCE in 2008 [47].

1.3.3 Hybrid Polymer/Nanocrystals Solar Cells

In polymer-based solar cells, the nanostructure (morphology) plays an important role in determining the PCE. To optimize the nanostructure, much research has been focused on studying annealing processes, kinetics of solvent removal, and phase

separation. However, nanocrystals can be efficient electron acceptors/donors for organic solar cells and nanocrystals in a polymer matrix provide an alternative approach for large-scale and low-cost photovoltaic devices. A hybrid solar cell contains polymer and inorganic materials in order to utilize their advantages in combination with each other. Polymers are efficient light absorbers and have the potential for low-cost manufacturing due to their solution-based processing properties. Additionally, polymers are cost-efficient due to strong visible absorption so that only thin films are required in solar cells. For nanocrystals, the properties of bulk materials change due to quantum confinement. It is possible to change the size of nanocrystals in order to advantageously change a film's optical properties without compromising the polymer-based solar cell fabrication process.

In 1996, Greenham *et al.* reported the first polymer/nanocrystals solar cell made by dispersing CdSe or CdS nanocrystals into the conjugated polymer, MEH-PPV [48]. The best efficiency cells were obtained by using a 90wt% (weight ratio) nanocrystals, with a corresponding volume ratio around 50%. Although the best cells only had an efficiency lower than 0.1% under AM 1.5 one sun conditions and 10% EQE at 514 nm, this indicated that there is significant exciton dissociation at the polymer/nanocrystals interface. Greenham *et al.* also indicated that long ligands on nanocrystal surfaces may impede the transport of carriers between nanocrystals [48].

In 2002, a breakthrough hybrid solar cell made from a blend of CdSe nanorods and poly-3(hexylthiophene) (P3HT) was reported by Huynh *et al*. P3HT is known as a good hole-transporter and a strong absorber in the visible spectrum [49]. Nanorods provided improved electron transport and large exciton dissociation area in the device. The authors also attached pyridine, a short ligand, onto the CdSe nanorod surfaces to improve film morphology. CdSe nanorods passivated with pyridine are soluble in pyridine and disperse uniformly in the film after spin-coating. Pyridine is a weak binding ligand and can be removed by annealing the devices at 120 °C. By mixing the CdSe nanorods with P3HT and annealing the devices to remove the pyridine, the authors produced 90wt% nanorods/polymer solar cells which showed 1.7% PCE under AM 1.5G one sun conditions. This cell had 5.8 mA/cm^2 I_{sc}, 0.7 V V_{oc}, and 0.44 FF, and achieved 55% EQE

at 485 nm. The architecture and I-V curve of a CdSe nanorods/P3HT device is shown in Figure 1-16.

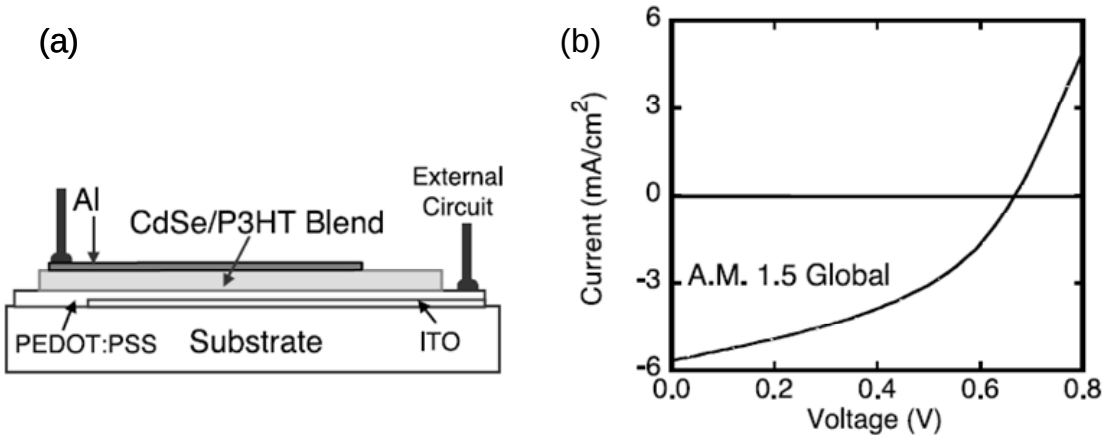

Figure 1-16. (a) The structure of CdSe nanorods/P3HT hybrid solar cell. (b) I-V of 90% CdSe nanorods (7 nm by 60 nm)/P3HT hybrid solar cells under AM 1.5G one sun conditions [49].

Although CdSe/P3HT solar cells have shown promising efficiencies, Cd is a toxic heavy metal and Se is also toxic in large quantities. To solve this problem, various hybrid solar cells have been reported using zinc oxide (ZnO) [50] and TiO_2 [51] nanocrystals. In 2004, Kwong *et al.* studied hybrid films consisting of TiO_2 nanocrystals and P3HT with different concentration of TiO_2 nanocrystals and different solvents. They obtained 0.4% PCE under AM 1 one sun conditions. The best device made with 60 wt% TiO_2 in xylene had 2.76 mA/cm^2 I_{sc}, 0.44 V V_{oc}, 0.36 FF, and 14% IPCE at 475 nm. In 2004, Beek *et al.* reported hybrid solar cells made from poly [2-methoxy-5-(3',7'-dimethyloctyloxy)-1,4-phenylenevinylene] (MDMO-PPV) and ZnO nanocrystals. This hybrid device showed a 1.6% PCE under 0.71 sun white light illumination using a tungsten-halogen lamp. It had 2.4 mA/cm^2 I_{sc}, 0.81 V V_{oc}, and 0.59 FF with 40% IPCE around 500 nm. ZnO and TiO_2 are non-toxic materials and have wide band gaps which only absorb deep violet; therefore, the efficiencies of ZnO/polymer or TiO_2/polymer solar cells are not as good as CdSe/polymer solar cells.

Current conjugated polymers for solar cell applications are good absorbers in the visible light region. To utilize the solar infra-red spectrum, low band gap materials are used in hybrid films. In 2005, Maria *et al.* used lead sulfide (PbS) nanocrystals and poly-

3(octylthiophene) (P3OT) to form a bilayer hybrid solar cell [52]. This cell did not show promising efficiency, but showed a >10% IPCE in the infra-red region. The same year, Watt *et al.* also reported a hybrid solar cell by in situ synthesis of PbS nanocrystals within a MEH-PPV film [53, 54]. This device showed a 0.7% PCE under AM 1.5 illumination at 5 mW/cm^2. However, there is not significant evidence showing the contribution to the photocurrent from the PbS nanocrystals. In 2006, Cui *et al.* reported a hybrid solar cell from the blend of MEH-PPV and PbSe nanocrystals. This device had a 0.14% PCE with 1.08 mA/cm^2 I_{sc}, 0.35V V_{oc}, and 0.37 FF under AM 1.5 one sun illumination. The PbSe nanocrystals contributed to 33% of the short-circuit current. Although low band gap nanocrystals can harvest infra-red light, low band gaps also possibly reduce the V_{oc}.

1.4 Thesis Overview

The primary purpose of this thesis is to apply silicon nanocrystals (Si NCs) in photovoltaic devices to achieve solution-processed solar cells. Compared to the II-VI semiconductor or the other compound materials, Si is an attractive photovoltaic material due to its stability, abundance, and non-toxicity. Silicon technology is also well-studied in industrial applications and has enjoyed years of success in the solar cell industry. The first research approach described in this thesis is a hybrid solar cell which was made by incorporating Si NCs into a conductive polymer matrix. The second approach is a Si NCs-only photovoltaic device made from solution processes. Chapter 2 describes the experimental methods used, including Si NC synthesis from a non-thermal plasma, Si NC characterization, solar cell design, ITO on glass substrate fabrication, solar cell encapsulation, and solar simulator setup.

The fabrication of Si NCs/P3HT hybrid solar cells is described in Chapter 3 and has been published as C. Y. Liu, Z. C. Holman and U. Kortshagen, "Hybrid Solar Cells from P3HT and Silicon Nanocrystals," *Nano Lett*. **9**, 449 (2009). In this work, we reported new hybrid solar cells based on blends of Si NCs and P3HT polymer in which a percolating network of the nanocrystals acts as the electron-conducting phase. The properties of composite Si NCs/P3HT devices made by spin-coating Si NCs and P3HT from a common solvent were studied as a function of Si NC size and Si NC/P3HT ratio. The open-circuit voltage and short-circuit current are observed to depend on the Si NC size due to changes in the band gap and surface-area-to-volume ratio. Under simulated one-sun AM 1.5D illumination (100 mW/cm^2), devices made with 35wt% Si NCs 3-5 nm in size showed 1.15% power conversion efficiency.

Chapter 4 has been prepared for submission as C. Y. Liu and U. Kortshagen, "Optimization of Si NCs/P3HT Hybrid Solar Cells." In this work, we try to optimize the efficiency of Si NCs/P3HT hybrid solar cells by post-production heat treatment. The effect of different metal electrodes on Si NCs/P3HT hybrid solar cells was also studied in this chapter. In order to understand hole transport in P3HT, the hole mobility was measured by using a high work function metal to block electron injection and form hole-

transport-only devices. After heat treatment, Si NCs/P3HT solar cells can reach a power conversion efficiency of 1.47%. The hole mobility of P3HT increases from 2.48×10^{-10} $m^2V^{-1}s^{-1}$ to 1.11×10^{-9} $m^2V^{-1}s^{-1}$ after annealing. The one order of magnitude increase in hole mobility suggests improved crystallinity of the P3HT film, which can enhance the hybrid device efficiency. Quenching of open-circuit voltage and short-circuit current was observed when high work function metals were deposited on the Si NCs/P3HT hybrid devices.

Chapter 5 has been prepared for submission as C. Y. Liu and U. Kortshagen, "Hybrid Solar Cells from MDMO-PPV and Silicon Nanocrystals." In this work, we make a new type of hybrid solar cell by replacing P3HT with MDMO-PPV and we compare the efficiency difference between Si NCs/MDMO-PPV and Si NCs/P3HT devices. Bulk heterojunction solar cells consisting of Si NCs and MDMO-PPV have been fabricated from a solution process. The properties of composite Si NCs/MDMO-PPV devices were studied as a function of Si NCs/MDMO-PPV weight ratio. Hybrid cells of 58wt% Si NCs/MDMO-PPV show a power conversion efficiency of 0.49% under simulated one sun AM 1.5D illumination (100 mW/cm^2). Compared to the composite film of Si NCs and P3HT, the low efficiency of Si NCs/MDMO-PPV may result from lower hole mobility and narrow absorption spectrum of MDMO-PPV. The energy band alignment of Si NCs and MDMO-PPV could be one of the reasons limiting the device efficiency.

Chapter 6 has been prepared for submission as C. Y. Liu and U. Kortshagen, "A New Solution Process for Silicon Nanocrystals Thin-Film Photovoltaic Devices." In this work, we try to fabricate a Si NCs-only thin-film photovoltaic device from a Si suspension without any ligand attachment or exchange and removal reactions. A single layer Schottky photovoltaic device of intrinsic Si NCs was fabricated by spin-coating in a glove box. A photovoltaic device based on a sandwich structure of a 250 nm Si NC layer between ITO and Al electrodes was measured under AM 1.5D one sun illumination. This device showed a significant photovoltaic response with a power conversion efficiency of 0.02%, a fill factor of 0.26, short circuit-current density of 0.148 mA/cm^2, and open-circuit voltage of 0.51 V.

Finally, chapter 7 gives a conclusion of Si NCs application in hybrid and nanocrystals-only photovoltaic devices and justification for future work.

1.5 References

[1] D. M. Chain, C. S. Fuller, and G. L. Pearson, *J. Appl. Phys.* **25**, 676 (1954).

[2] N. S. Lewis, *MRS Bull.* **32**, 808 (2007).

[3] C. Kittel, *Introduction to Solid State Physics*, John Wiley & Sons (2005).

[4] M. A. Loi, S. Toffanin, M. Muccini, M. Forster, U. Scherf, and M. Scharber, *Adv. Funct. Mater.* **17**, 2111 (2007).

[5] N. T. Binh, M. Gailberger and H. Bässler, *Synth. Met.* **47**, 77 (1992).

[6] G. Lanzani, L. Rossi, S. Stagira, S. D. Silvestri, and F. Garnier, *Opt. Mater.* **9**, 445 (1998).

[7] Z. G. Soos, M. H. Hennessy, and G. Wen, *Chem. Phys.* **227**, 19 (1998).

[8] S. H. Lim, T. G. Bjorklund, F. C. Spano, and C. J. Bardeen, *Phys. Rev. Lett.* **92**, 107402 (2004).

[9] H. Sirringhaus, P. J. Brown, R. H. Friend, M. M. Nielsen, K. Bechgaard, B. M. W. Langeveld-Voss, A. J. H. Spiering, R. A. J. Janssen, E. W. Meijer, P. Herwig, and D. M. de Leeuw, *Nature*, **401**, 685 (1999).

[10] M. S. A. Abdou, F. P. Orfino, Y. Son, and S. Holdcroft, *J. Am. Chem. Soc.* **119**, 4518 (1997).

[11] M. L. Chabinyc, R. A. Street, and J. E. Northrup, *Appl. Phys. Lett.* **90**, 123508 (2007).

[12] R. W. Murray, *Acc. Chem. Res.* **1**, 313 (1968).

[13] J. Rostalski and D. Meissner, *Sol. Energy Mater. Sol. Cells*, **61**, 87 (2000).

[14] S. Sun and N. S. Sariciftci, *Organic Photovoltaics: Mechanisms, Materials, and Devices*, Taylor & Francis (2005).

[15] B. R. Saunders and M. L. Turner, *Adv. Colloid Interfac.* **138**, 1 (2008).

[16]http://www.newport.com/Introduction-to-Solar-Radiation/411919/1033/catalog.aspx

[17] J. Tsukamoto, H. Ohigashi, K. Matsumura, and A. Takahashi, *J. Appl. Phys.* **20**, L127–L129 (1981).

[18] J. Kanicki, and P. Fedorko, *J. Phys. D: Appl. Phys.* **17**, 805 (1984).

[19] S. Glenis, G.. Horowitz, G.. Tourillon, and F. Garnier, *Thin Solid Films*, **111**, 93 (1984).

[20] Y. Fang, S. A. Chen, and M. L. Chu, *Synth. Met.* **52**, 261 (1992).

[21] N. S. Sariciftci, L. Smilowitz, A. J. Heeger, and F. Wudl, *Science*, **258**, 1474 (1992).

[22] H. W. Kroto, J. R. Heath, S. C. O'Brien, R. F. Curl, and R. E. Smalley, *Nature,* **318**, 162 (1985).

[23] W. Krätschmer, L. D. Lamb, K. Fostiropoulos, and D. R. Huffman, *Nature*, **347**, 354 (1990).

[24] Y. Ohsawa and T. Saji, *J. Chem. Soc. Chem. Commun.* **10**, 781 (1992).

[25] N. S. Sariciftci, D. Braun, C. Zhang, V. I. Srdanov, A. J. Heeger, G. Stucky, and F. Wudl, *Appl. Phys. Lett.* **62**, 585 (1993).

[26] M. Drees, K. Premaratne, W. Graupner, J. R. Heflin, R. M. Davis, D. Marciu, and M. Miller, *Appl. Phys. Lett.* **81**, 4607 (2002).

[27] L. H. Spherling, *Introduction to Physical Polymer Science*, Wiley-interscicenc (2001).

[28] G.. Yu, J. Gao, J. C. Hummelen, F. Wudl, and A. J. Heeger, *Science*, **270**, 1789 (1995).

[29] S. E. Shaheen, R. Radspinner, N. Peyghambarian, and G. E. Jabbour, *Appl. Phys. Lett.* **79**, 2996 (2001).

[30] W. Ma, C. Yang, X. Gong, K Lee, and A. J. Heeger, *Adv. Funct. Mater.* **15**, 1617 (2005).

[31] http://polymer.matscieng.sunysb.edu/images/js03.gif

[32] R. Rossetti, J. L. Ellison, J. M. Gibson, and L. E. Brus, *J. Chem. Phys.* **80**, 4464 (1984).

[33] M. A. Reed, R.T. Bate, K. Bradshaw, W. M. Duncan, W. R. Frensley, J. W. Lee, and H. D. Shih, *J. Vac. Sci. Technol. B*, **4**, 358(1986).

[34] S. Schmitt-Rink, D. A. B. Miller, and D.S. Chemla, *Phys. Rev. B*, **35** ,8113 (1987).

[35] T. Vossmeyer, L. Katsikas, M. Giersig, I. G. Popovic, K. Diesner, A. Chemseddine, A. Eychmueller, and H. Weller, *J. Phys. Chem.* **98**, 7665 (1994).

[36] A. N. Goldstein, C. M Echer, and A. P. Alivisatos, *Science*, **256**, 1425 (1992).

[37] A. P. Alivisatos, *J. Phys. Chem.* **100**, 13226 (1996).

[38] L. E. Brus, *J. Chem. Phys.* **90**, 2555 (1986).

[39] D. Vanmaekelbergh, and P. Liljeroth, *Chem. Soc. Rev.* **34**, 299 (2005).

[40] M. G. Bawendi, W. L. Wilson, L. Rothberg, P. J. Carroll, T. M. Jedju, M. L. Steigerwald, and L. E. Brus, *Phys. Rev. Lett.* **65**,1623 (1990).

[41] A. R. Kortan, R. Hull, R. L. Opila, M. G. Bawendi, M. L. Steigerwald, P.J. Carroll, and L. E. Brus, *J. Am. Chem. Soc.* **112**,1327 (1990).

[42] M. G. Bawendi, P. J. Carroll, W. L. Wilson, and L. E. Brus, *J. Chem. Phys.* **96**, 946 (1992).

[43] C. B. Murray, D. J. Norris, and M. G. Bawendi, *J. Am. Chem. Soc.* **115**, 8706 (1993).

[44] V. L. Colvin, M. C. Schlamp, and A. P. Alivisatos, *Nature*, **370**, 354 (1994).

[45] A. J. Nozik, *Physica E*, **14**, 115 (2002).

[46] B. O'regan, and M. Grätzel, *Nature*, **353**, 737 (1991).

[47] Y. Bai, Y. Cao, J. Z., M. Wang, R. Li, P. Wang, S. M. Zakeeruddin, and M. Grätzel, *Nat. Mater.* **7**, 626 (2008).

[48] N. C. Greenham, X. Peng, and A. P. Alivisatos, *Phys. Rev. B*, **54**, 17628 (1996).

[49] W. U. Huynh, J. J. Dittmer, and A. P. Alivisatos, *Science*, **295**, 2425 (2002).

[50] W. J. E. Beek, M. M. Wienk, and R. A. J. Janssen, *Adv. Funct. Mater.* **12**, 1009 (2004).

[51] C. Y. Kwong, A. B. Djurisic, P. C. Chui, K. W. Cheng, and W. K. Chan, *Chem. Phys. Lett.* **384**,372 (2004).

[52] A. Maria, P. Cyr, E. Klem, L. Levina, and E. H. Sargent, *Appl. Phys. Lett.* **87**, 213112 (2005).

[53] A. Watt, E. Thomsen, P. Meredith, and H. Rubinsztein-Dunlop, *Chem. Commun.* **20,** 2334 (2004).

[54] A. A. R. Watt, D. Blake, J. Warner, E. A. Thomsen, and E. L. Tavenner, *J. Phys. D: Appl. Phys.* **38**, 2006 (2005).

Chapter 2

Experimental Method

2.1 Overview

This chapter outlines the steps used for the fabrication and characterization of hybrid solar cells and nanocrystal-only photovoltaic devices. In order, this chapter covers the plasma synthesis, characterization and collection of silicon nanocrystals, design of solar cells, ITO substrate fabrication, solar cell encapsulation, solar simulator setup, and optical characterization.

2.2 Plasma Synthesis of Silicon Nanocrystals

Silicon nanocrystals (Si NCs) were synthesized in a nonthermal radio frequency (RF, 13.56 MHz) plasma via dissociation of silane, and collected on mesh filters [1]. Briefly, precursors of 5% silane (SiH_4)/helium (He), argon (Ar), and hydrogen (H_2) were passed through a quartz or Pyrex tube around which a pair of copper ring electrodes was wrapped. 2-20 nm Si NCs can be synthesized by varying the tube size, precursor flow rate, and RF power. Three groups of Si NCs were used in this study: Si NCs that were 3-5 nm in diameter, 5-9 nm in diameter, and 10-20 nm in diameter. Synthesis conditions and the experimental setup for the different sizes of Si NCs used in this study are shown in Table 2-1 and Figure 2-1. To minimize oxidation, Si NC collection and handling were conducted in a nitrogen-purged glove bag (oxygen level < 25 ppm) and a glove box (MBraun, oxygen level< 1 ppm, moisture level< 1 ppm). Prior to device fabrication, Si NCs were characterized by transmission electron microscopy (TEM), Fourier-transform infrared spectroscopy (FTIR), and X-ray diffraction (XRD). TEM, which was used to determine average size, shows spherical particles with narrow size distributions (standard

deviation < 25% of the mean size, see Figure 2-2). Figure 2-3 presents FTIR and XRD spectra of Si NCs. FTIR spectra of Si NCs (Figure 2-3a) show Si-H_x bands at 850, 900, and 2100 cm^{-1} for all Si NC sizes, indicating that the nanocrystal surfaces are terminated by hydrogen. XRD spectra (Figure 2-3b) show the (111), (220), (311), (400), and (331) diffraction peaks of diamond cubic Si for all samples, and peak broadening as the crystallite size decreases.

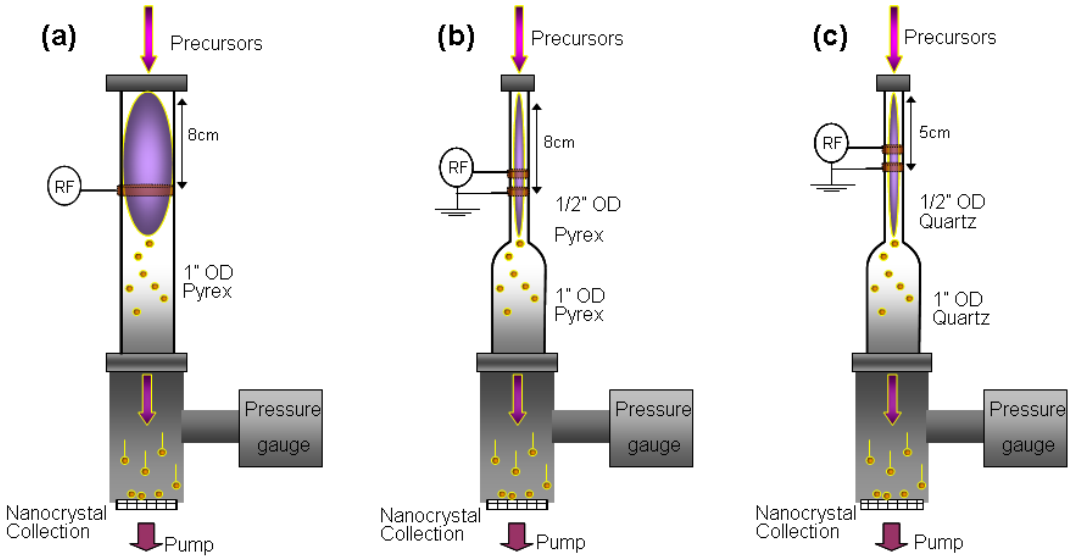

Figure 2-1. Non-thermal RF plasma synthesis systems of (a) 10-20 nm, (b) 5-9 nm, and (c) 3-5 nm Si NCs.

5% SiH_4/He (SCCM)	Ar (SCCM)	H_2 (SCCM)	Pressure (Torr)	RF Power (W)	Si NC size (nm)
35	25	0	3.5	175	10-20 nm
140	100	0	3.5	135	5-9 nm
33	150	6	3.5	135	3-5 nm

Table 2-1. RF plasma synthesis conditions for different sizes of Si NCs.

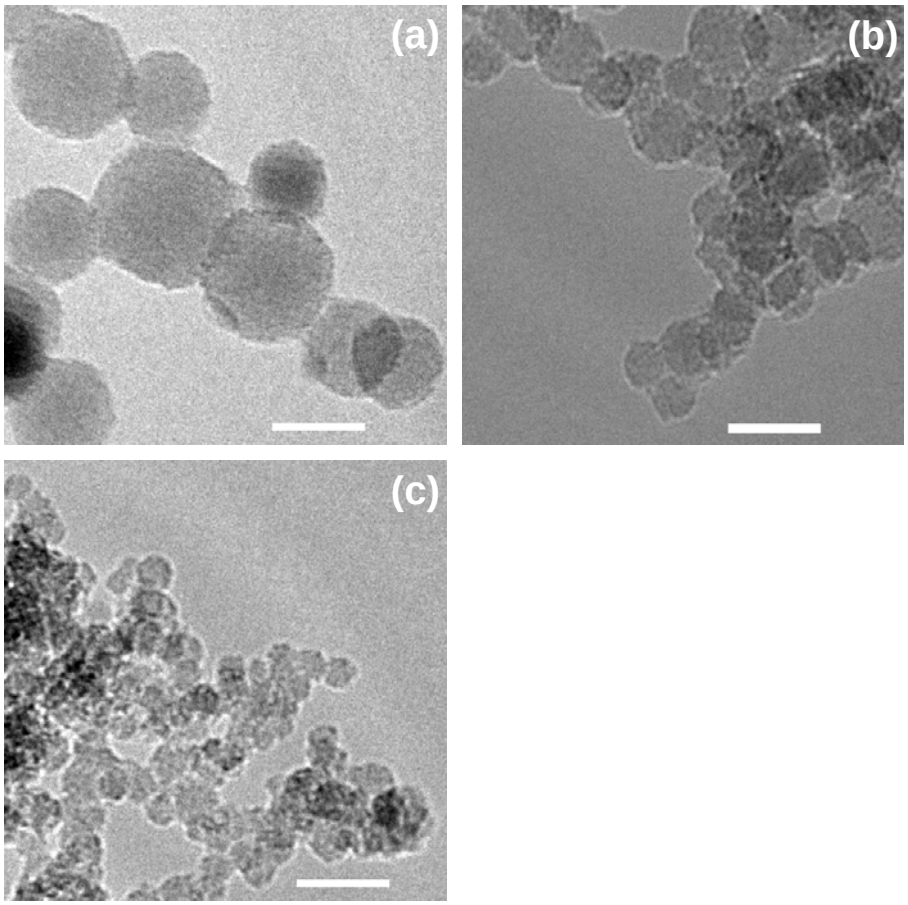

Figure 2-2. TEM images of different sizes of Si NCs. (a) 10-20 nm Si NCs made using 35 SCCM 5% SiH_4/He and 25 SCCM Ar at 175 W; (b) 5-9 nm Si NCs made using 140 SCCM 5% SiH_4/He and 100 SCCM Ar at 135 W; and (c) 3-5 nm Si NCs made using 33 SCCM 5% SiH_4/He, 6 SCCM H_2, and 150 SCCM Ar at 135 W. Scale bar, 10 nm.

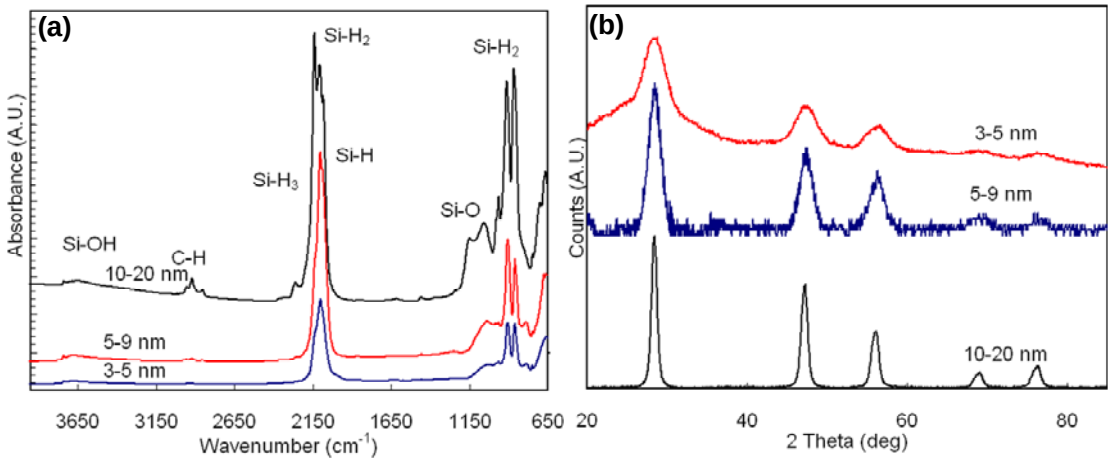

Figure 2-3. (a) FTIR and (b) XRD spectra of different sizes of Si NCs showing Si-H vibrations from the hydrogen-terminated particle surfaces and diffraction peaks from diamond cubic Si.

2.3 Silicon Nanocrystal Collection

Silicon nanocrystals were collected on mesh filters downstream of the plasma. The weight of Si NCs was measured inside a glove bag (oxygen level < 25 ppm) immediately after the chamber was opened. After the weight measurement, the Si NCs and mesh (Figure 2-4a) were sealed in an air-tight bottle (Screw top vial, 27150-U, Sigma-Aldrich). The whole bottle was transferred into the glove box as soon as possible. 1,2-dichlorobenzene (DCB, ACROS) was poured into the bottle with the Si NCs until the whole mesh was immersed in DCB (Figure 2-4b). The vial was taken out the glove box for sonication to release the Si NCs from the mesh into the DCB. To secure the vial cap better, electrical tape was wrapped around the vial and cap. After sonication, the electrical tape was removed before the vial was transferred into the glove box. The cloudy solution of Si NCs in DCB was transferred into a vial containing polymer via a syringe. The mesh absorbs about 10% of the solution so that at least 10% of the Si NCs were lost during the transfer process. For example, 2 ml DCB was mixed with 20 mg Si NCs on mesh and 1.8 ml DCB was taken out from the mixture. We assumed 10% of the Si NCs were lost for each transfer process (one mesh process).

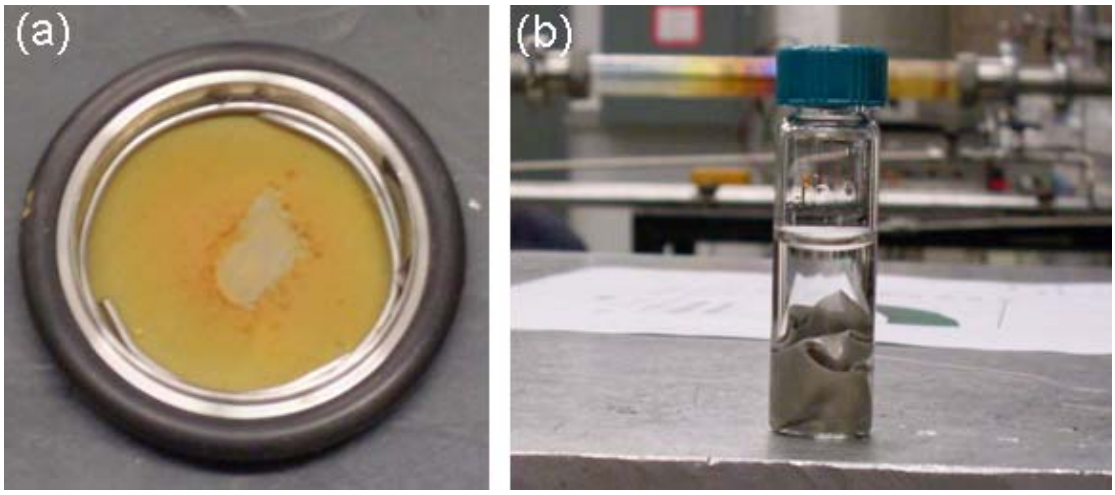

Figure 2-4. Photograph of Si NCs on mesh and Si NCs on mesh in the solvent before sonication.

2.4 Design of Solar Cells

Solar cells were fabricated on indium tin oxide (ITO) coated glass substrates. There are two 2.3 mm wide ITO strips near the middle of the glass substrate. After deposition of the active layer, the metal contacts (2 mm wide) are evaporated by a thermal evaporator under high vacuum (pressure < $2x10^{-6}$ Torr). There are six devices on each substrate. The cross section, which is 0.046 cm^2 between each metal contact and the ITO patterns, is considered as the active area because the exciton diffusion length of the polymer is smaller than 100 nm. Carriers generated outside of the active area cannot reach the metal or ITO electrodes before recombination. The design and photograph of solar cells are shown in Figure 2-5 and Figure 2-6, respectively.

Two polymers, P3HT and MDMO-PPV, have been used with Si NCs. Before Si NCs were added into the polymer solution, P3HT and MDMO-PPV were dissolved in DCB and stirred at 55 °C on the plate for two hours and overnight, respectively. The poly(3,4- ethylenedioxy thiophene)/poly(styrenesulfonate) (PEDOT:PSS) (Baytron P VP Al 4083 grade from H. C. Starck) coated ITO substrate was prepared in the Nanofabrication Center by spin-casting PEDOT:PSS solution at 4000 rpm for 60 seconds twice. To provide good contact between ITO and PEDOT:PSS, ITO substrates were treated with by UV-Ozone cleaner for 10 minutes to clean the substrate surface and make it hydrophilic. After PEDOT:PSS was spin-cast, excess water was then removed from the PEDOT:PSS film by baking at 130 ˚C for 5 minutes. After Si NCs were added into the polymer solution, the concentrations of P3HT or MDMO-PPV were 15 mg/ml or 6 mg/ml, respectively. Due to the agglomeration of Si NCs, the blend solution of Si NCs with polymer needed to be sonicated in the water bath before spin-casting. The blend solution of Si NCs with polymers was spin-cast onto the PEDOT:PSS coated ITO substrates at 700 rpm for 60 seconds in a glove box. Due to the high boiling point of DCB, the film appeared wet after spin-casting. These hybrid films needed to be dried on a test-tube rack for 10 minutes before metal contact deposition.

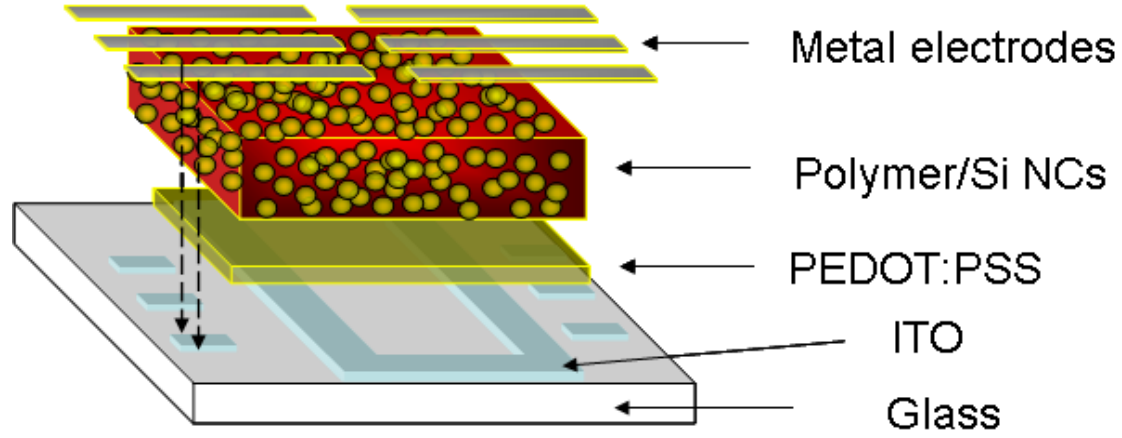

Figure 2-5. Schematic of sequential deposition in fabrication of the hybrid or nanocrystals-only solar cells.

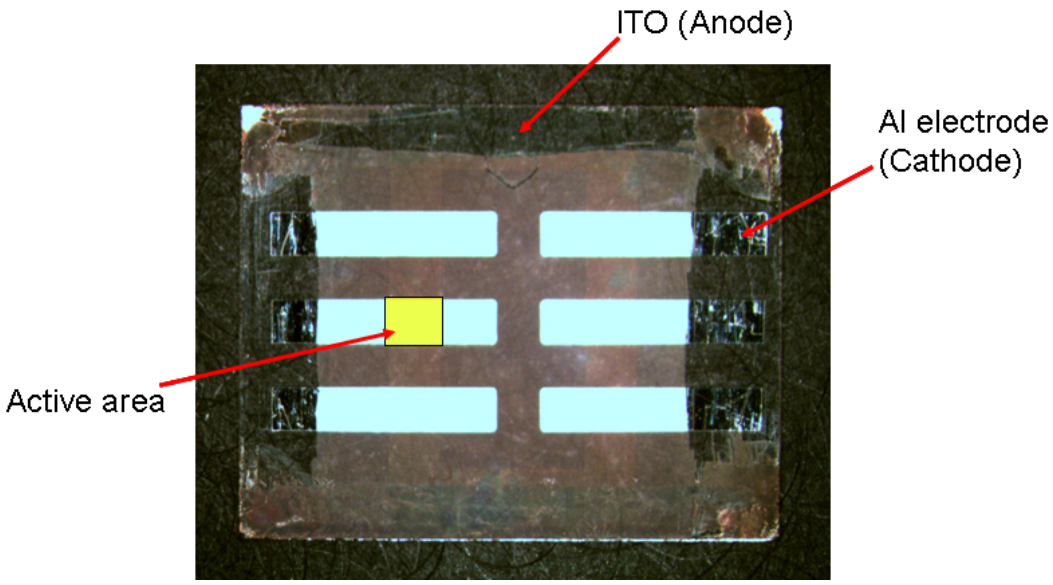

Figure 2-6. Photograph of a hybrid solar cell from P3HT and silicon nanocrystals. The ITO pattern can be seen under the film and the yellow area indicates the active area, which is the cross section of the Al electrode and the ITO pattern.

2.5 ITO Substrate Fabrication

Indium tin oxide coated on polished float glass substrates (25 mm x 20 mm) were patterned using photolithography and etched in a mixture of hydrochloric acid, nitric acid, and water. The design of the ITO substrate is shown in Figure 2-7. The six islands of ITO on the edges of the substrate were designed for better probe contact. The thickness of

metal contacts was usually 100 nm for this study. Without the ITO islands, the probes may penetrate the electrodes and cannot make a good electrical contact. The six ITO islands are located 1 mm away from the substrate edge to prevent device connection which can happen due to mask misalignment during the evaporation process. To reduce the ITO substrate preparation time, we do not fabricate the substrates one by one, but instead patterning a large area ITO on glass plate. One 150 mm x 150 mm ITO coated glass plate of 8 to 12 Ω/square resistance (Delta Technologies, LTD) was used for photolithography. The ITO pattern was printed on a transparent slide (Pageworks), which was then cut and attached to a glass plate (Corning 1737, Delta Technologies, LTD) to complete the shadow mask. The resolution of the printing pattern is 5080 dots per inch (dpi). The design of the shadow mask is shown in Figure 2-8a. The assembly of the shadow mask is shown in Figure 2-8b. Because the feature size of the ITO patterns is in the millimeter range, the alignment of the shadow mask was done with a home-made alignment plate (Figure 2-9a).

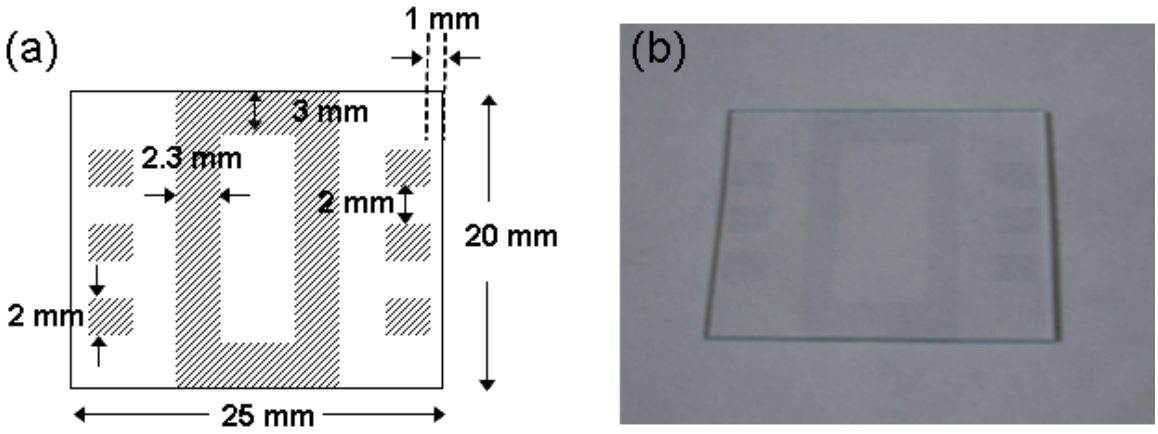

Figure 2-7. (a) Schematic and (b) photograph of the ITO pattern design on the glass for solar cell fabrication.

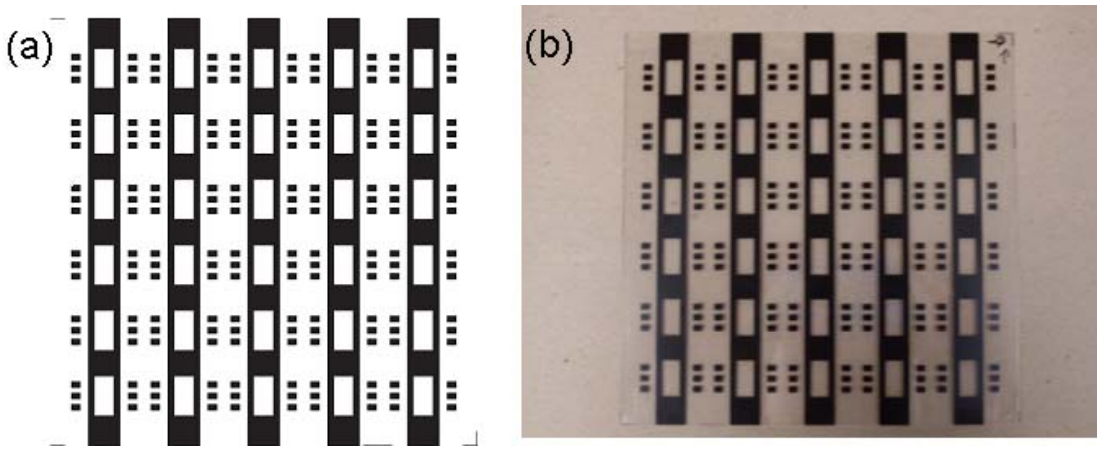

Figure 2-8. (a) Design and (b) photograph of the shadow mask for ITO patterning on the glass plate.

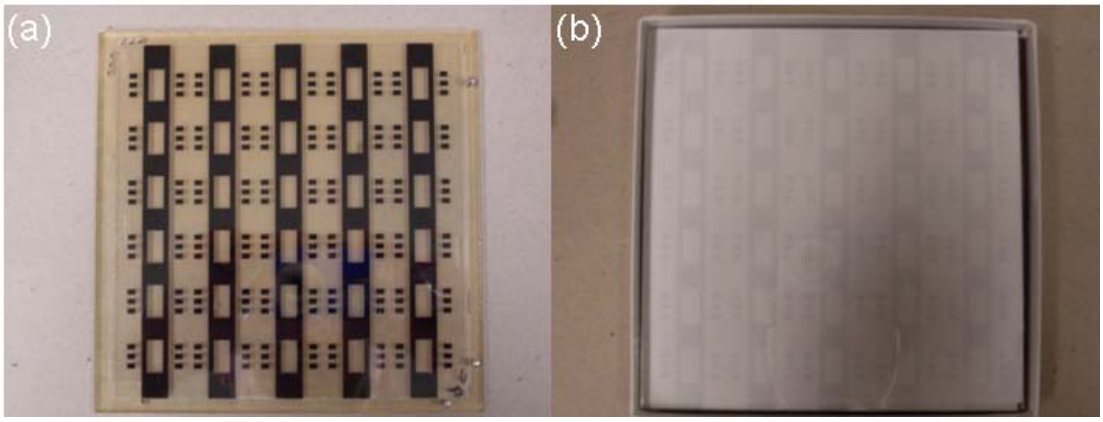

Figure 2-9. (a) Photograph of the shadow mask on the home-made alignment plate. (b) Photograph of ITO pattern on a glass plate.

The photolithography steps and the etching process are described below.

1. Because the substrates are too large for sonication, the 150 mm x 150 mm substrates were cleaned by rinsing with acetone, isopropanol, and deionized water (DI water), and dried under an nitrogen gun.
2. The substrates were prebaked at 115 ºC to dry excess water.
3. HMDS vapor was applied for two to three minutes to provide better adhesion between ITO and photoresist.
4. Shipley 1818 photoresist was spun on the ITO at 3000 rpm for 60 seconds. The thickness of the photoresist was around 1.25 μm.

5. After spin-casting, the substrates were soft baked on a hot plate at 105 ºC for 5 minutes to remove the solvents from the photoresist coating.

6. The mask was aligned with the substrates and exposed for 20 seconds in an Oriel flood exposure system which emits UV light in 350-450 nm region.

7. After exposure, the substrates were immersed in a developer containing 5:1 water/Microposit 351 developer for 75 seconds to remove the exposed photoresist, until rainbows on the surface or brownish clouds were no longer visible.

8. After development, the substrates were rinsed with water and dried with a nitrogen gun.

9. The substrates were hard baked on a hot plate at 120 ºC for 20 minutes to harden the photoresist and enhance the adhesion of the photoresist to the ITO surface.

10. The substrates were put into the etching solution for 3 minutes in a beaker which was heated on a hot plate at 50 ºC. The etching solution contained a mixture of 5% hydrochloric acid and 20% nitric acid by volume in water. After etching, the substrates were rinsed with DI water and dried with a nitrogen gun. To ensure the etching process was successful, the ohmmeter was used to indentify whether the ITO was completely removed.

11. Finally, the unexposed photoresist on the ITO was removed in an acetone bath.

The ITO plate after patterning is shown in Figure 2-9b. The large pattern ITO plates were cut into individual 20 mm x 25 mm substrates. The shadow mask was designed to produce 30 solar cell substrates per large ITO plate, but substrates located in the corner usually did not have enough exposure time due to exposure machine limit and shadowing effects. The substrate yield rate is around 86% (26/30). A flow diagram of ITO etching process is shown in Figure 2-10.

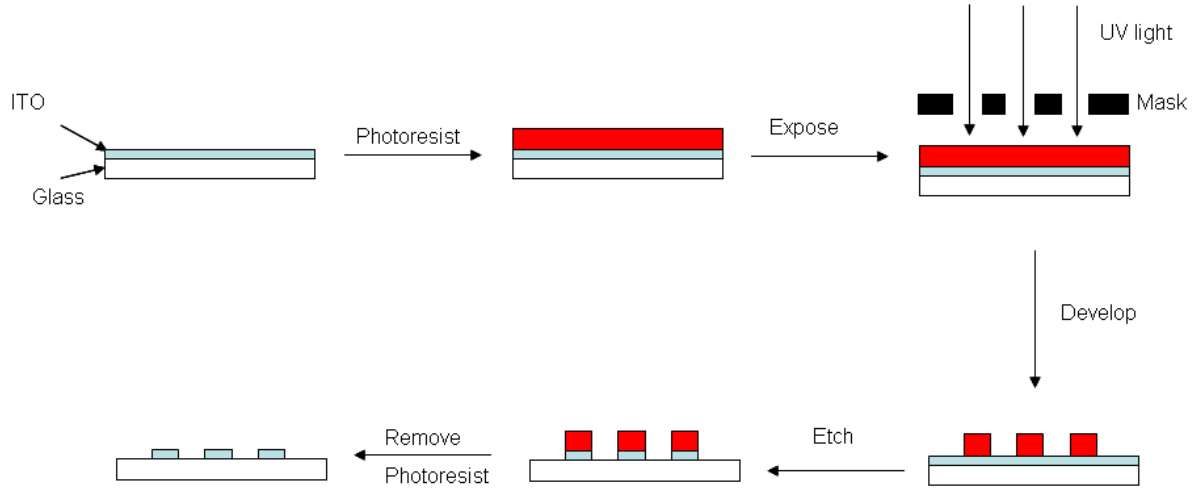

Figure 2-10. A flow diagram of the ITO etching process.

2.6 Encapsulation of Solar Cells

The solar simulator is located outside the glove box. To prevent oxidation of solar cells under atmospheric gases, solar cell test-holders were used for electrical measurements. Test-holders were designed using commercial stainless steel components, which are compatible with a leakage test machine. A schematic and photograph of the test-holder is shown in Figure 2-11. Design of the test-holder is based on the modification of two quick flanges (LDS vacuum, NW40-150-RF). Seven spring probes (Interconnect Devices, Inc., S-100-D-3.5G) were used on the top flange to provide electrical contact to solar cell electrodes. The middle and side probes provide electrical contact to the ITO and metal electrodes, respectively. A quartz glass plate (McMaster-Carr) was sealed on the bottom by Torr Seal vacuum epoxy (Thorlabs, Inc., TS10). The quartz window allows light transmission without blocking the UV light during illumination. There is a black pad on the top flange to prevent light reflection from the stainless steel during illumination. The test-holder with a solar cell after being assembled is shown in Figure 2-12. Leak tests of solar test-holders were conducted with an Alcatel ASM142 leak detector with helium gas. Leak rates less than 10^{-9} mbar·L/s were considered acceptable.

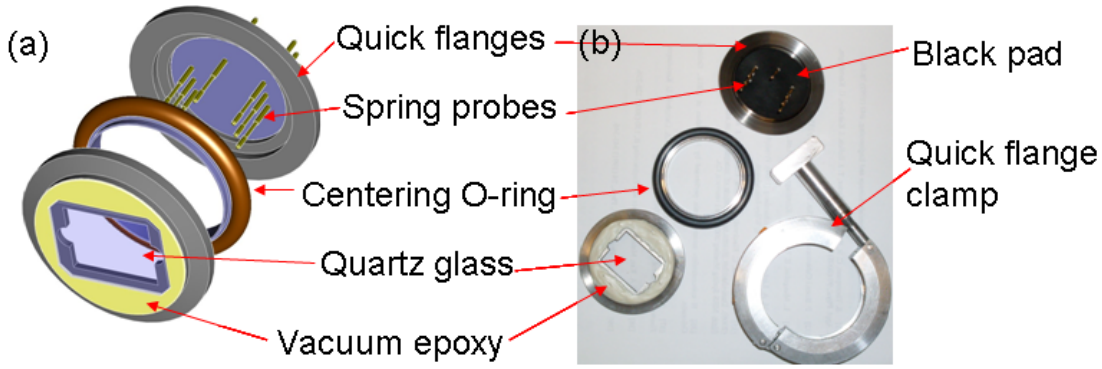

Figure 2-11. (a) Schematic (courtesy of Dave Hultman) and (b) photograph of the components of the solar cell test-holder.

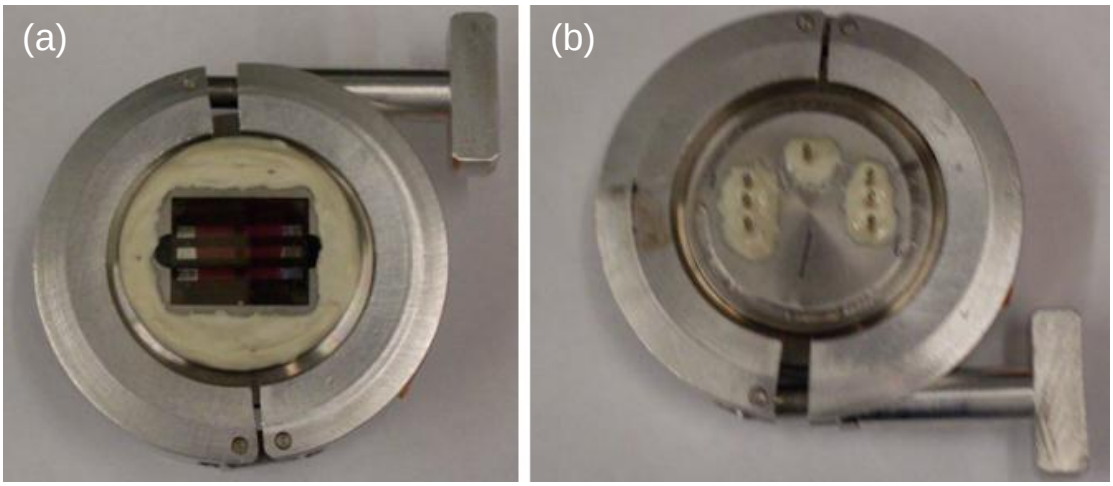

Figure 2-12. Photograph of the assembled test-holder with a solar cell. (a) Bottom view and (b) top view.

2.7 Solar Simulator

Current-voltage (I-V) characteristics of solar cells were measured using a Xenon-arc lamp (Oriel, 100 W) connected to a monochromator (Newport 74036, blaze wavelength = 500 nm) and Keithley 2400 Series or 2611A SourceMeter. This sun light simulator was set up by mounting a grating and a high reflectivity mirror with commercial filters (Newport Corp.) to the monochromator. There are AM 0 and AM 1.5D filters (Newport 81090 and 81092) between the monochromator and lamp to simulate AM 1.5D conditions. AM 1.5D spectrum is obtained by using the mirrors and selected wavelengths from the spectrum (IPCE measurement) are obtained by using the grating. The solar simulator setup is shown in Figure 2-13. The bandwidth of light passing through the

monochromator is controlled by the exit slit. The exit slit is usually set at 1.56 mm to allow around 10 nm of light to pass. The inlet slit of the monochromator is opened all the way to allow maximum light into the monochromator. The solar spectrum was calibrated by a radiometry system that included a Thermopile sensing probe and a radiant power meter from Newport (70268 and 70260). Solar cell measurement under AM 1.5D light illumination is shown in Figure 2-14.

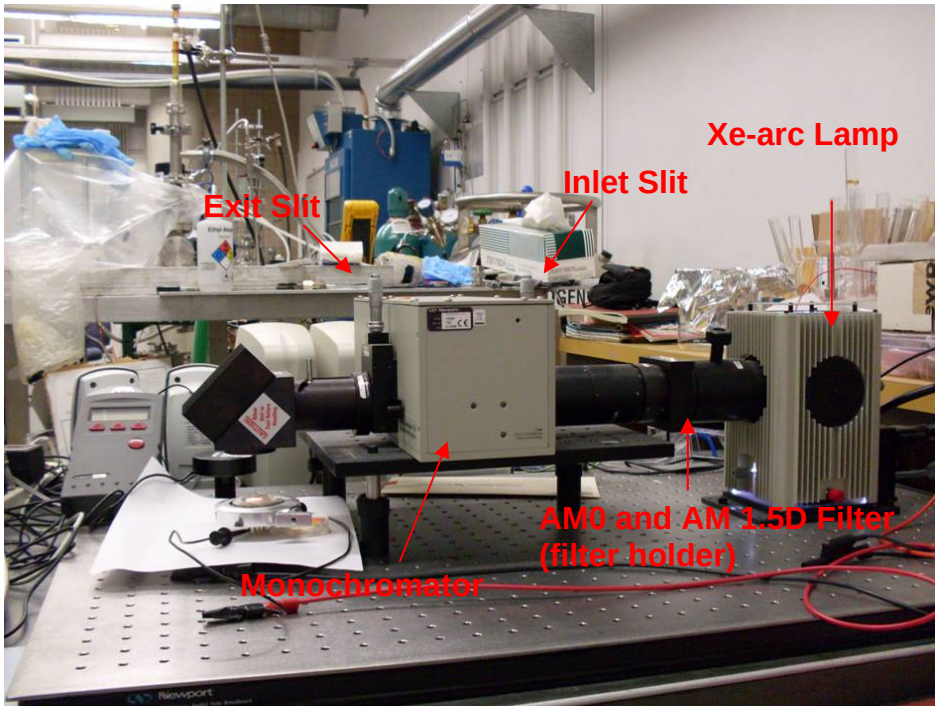

Figure 2-13. Photograph of the solar simulator.

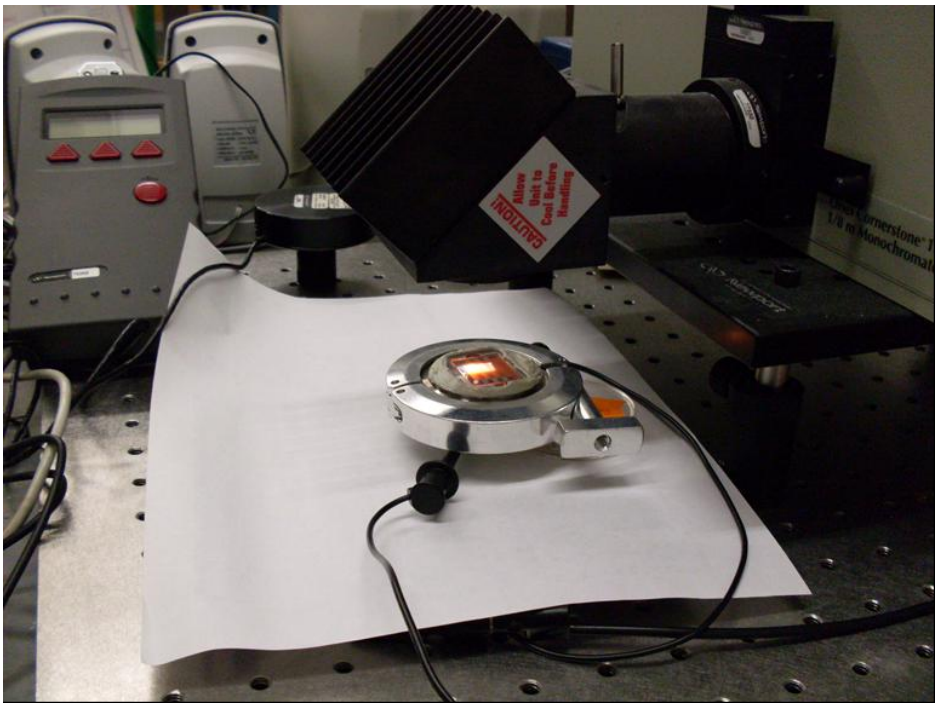

Figure 2-14. Photograph of the solar cell measurement. The solar cell is connected with two lines to measure the current and voltage under AM 1.5D illumination.

2.8 Optical Characterization

Optical absorption spectra of Si NCs and polymers were recorded by an absorption system (Ocean Optics) which includes a combination of deuterium and tungsten halogen lamps (DH-2000-BALL) and a spectrometer (HR2000). The spectrometer is equipped with a silicon detector that is sensitive in the 200–1100 nm range. The absorption measurements of polymers/Si NCs thin films were usually conducted using quartz substrates which are UV transparent. Quantum yield photoluminescence measurements of Si NCs were recorded using an integrating sphere, a 390 nm UV LED, and a USB spectrometer (Ocean Optics). The Si NCs fluorescence (all emitted photons) excited by the LED is picked up by the spectrometer.

2.9 References

[1] L. Mangolini, E. Thimsen, and U. Kortshagen, *Nano Lett.* **5**, 655 (2005).

Chapter 3

Hybrid Solar Cells from P3HT and Silicon Nanocrystals*

3.1 Overview

We are reporting new hybrid solar cells based on blends of silicon nanocrystals (Si NCs) and poly-3(hexylthiophene) (P3HT) polymer in which a percolating network of the nanocrystals acts as the electron-conducting phase. The properties of composite Si NCs/P3HT devices made by spin-coating Si NCs and P3HT from a common solvent were studied as a function of Si NC size and Si NC/P3HT ratio. The open-circuit voltage and short-circuit current are observed to depend on the Si NC size due to changes in the band gap and surface-area-to-volume ratio. Under simulated one-sun AM 1.5 direct illumination (100 mW/cm^2), devices made with 35 weight percent Si NCs 3-5 nm in size showed 1.15% power conversion efficiency.

3.2 Introduction

Hybrid solar cells based on mixtures of conjugated polymers and inorganic semiconductor nanocrystals are attractive because they may combine the desirable properties of both materials. Conjugated polymers are solution-processable and have strong visible absorption so that only thin films are required in solar cells. As a result, they have great potential for inexpensive large-scale solar cell manufacturing. Semiconductor nanocrystals have properties which differ from those in the bulk due to quantum confinement. It is therefore possible to tune the absorption spectra of

nanocrystals by changing their size. Nanocrystals may be blended with polymers without compromising the solution-based fabrication process, and a percolated network of nanocrystals in hybrid devices may provide high-mobility pathways for carriers.

Various promising hybrid solar cells have been reported, including devices which utilize polymer in conjunction with cadmium selenide (CdSe) [1], zinc oxide (ZnO) [2], titanium dioxide (TiO_2) [3], lead sulfide (PbS) [4], lead selenide (PbSe) [5], and copper indium disulphide ($CuInS_2$) [6] spherical nanocrystals; CdSe nanorods [7]; and CdSe hyper-branched nanocrystals [8]. These devices were made by spin-coating nanocrystal/polymer blends onto substrates where they phase segregate at the nanometer length scale to facilitate exciton dissociation and subsequent charge carrier transport. In these hybrid solar cells the organic semiconductor usually acts as the hole-transport medium while the inorganic nanocrystals take the role of electron-transporting medium. CdSe nanocrystals/poly-(3-hexylthiophene) (P3HT) solar cells currently hold the efficiency record for hybrid devices, with power conversion efficiencies (PCEs) greater than 2%. ZnO nanocrystals/ poly [2-methoxy-5-(3',7'-dimethyloctyloxy)-1,4-phenylenevinylene] (MDMO-PPV) and TiO_2 nanocrystals/P3HT solar cells have also shown impressive efficiencies [2, 3], but their performance is likely limited by the poor visible absorption of the wide-band gap nanocrystals. Hybrid solar cells made with PbS, PbSe, and $CuInS_2$ nanocrystals have not yet shown promising efficiencies.

Silicon (Si) has enjoyed years of success in the solar cell and microelectronics industries and is a prime candidate for polymer-nanocrystal solar cells given its abundance, non-toxicity, and strong UV absorption. Gowrishankar *et al.* have fabricated hybrid bilayer cells consisting of either P3HT or MEH-PPV spun onto hydrogenated amorphous silicon (a-Si:H) and achieved efficiencies of 0.16% [9]. Adikaari *et al.* have improved on this result by nanostructuring and crystallizing the a-Si:H to increase interfacial area and carrier mobility [10]. They reported a best efficiency of 0.87%, although the fill factor of 0.23 of the device was low. Here, we employ blends of free-standing silicon nanocrystals (Si NCs) and regioregular P3HT to form nanocrystal-polymer hybrid solar cells. As shown in Figure 3-1a, the band alignment of Si and P3HT is such that exciton dissociation at the interface is energetically favorable even for bulk Si

(dashed lines), and becomes increasingly favorable for quantum confined Si NCs (solid lines). These devices also have the potential for enhanced exciton dissociation compared to the aforementioned Si-containing hybrid devices due to the greater interfacial area afforded by the blend architecture. Additionally, Si NCs may contribute to the light absorption in these devices, offering an advantage over previous hybrids using wide-bandgap semiconductor nanocrystals. In order to optimize solar cell performance, different Si NC sizes and Si NC/P3HT ratios were explored.

3.3 Experimental

Silicon nanocrystals were synthesized in a nonthermal radio frequency (RF) plasma via dissociation of silane, and collected on mesh filters [11]. By varying chamber pressure, precursor flow rate, and RF power, Si NCs can be made with average sizes between 2–20 nm. To minimize oxidation, Si NC collection and handling were conducted in a nitrogen-purged glove bag and Schlenk line. As-produced Si NCs were dispersed in 1,2-dichlorobenzene (DCB, ACROS) and sonicated to form a cloudy solution. Prior to film formation, Si NCs were characterized by transmission electron microscopy (TEM), Fourier-transform infrared spectroscopy (FTIR) and X-ray diffraction (XRD). TEM, which was used to determine average size, shows spherical particles with narrow size distributions (standard deviation < 25% of the mean size, see Figure 2-2 in the chapter 2). Three groups of Si NCs were used in this study: Si NCs that were 3-5 nm in diameter, 5-9 nm in diameter, and 10-20 nm in diameter. FTIR spectra of all Si NCs show Si-H_x bands (Figure 2-3a), indicating that the nanocrystal surfaces are terminated by hydrogen. It should be noted that hydrogen passivation does not provide sufficient steric stabilization to overcome inter-particle Van der Waals attractions and prevent agglomeration of the Si NCs in solution. However, Van der Waals attractions can be significantly reduced by choosing a solvent with a Hamaker constant comparable to the Si NC Hamaker constant. We have observed that Si NCs are more stable in DCB than other common solvents such as toluene or hexane, and flocculate slowly over the course of weeks, not hours. We believe that this occurs because the dielectric constant of Si (11.7) is much closer to that

of DCB (9.8) than toluene (2.4) or hexane (1.9) [12]. XRD patterns for all sizes of particles display the (111), (220), (311), (400), and (331) diffraction peaks of diamond cubic Si (Figure 2-3b).

Solar cells were fabricated by spin-coating Si NCs/P3HT onto indium tin oxide (ITO) coated glass substrates. ITO-coated substrates (25 mm x 20 mm) of 8 to 12 Ω/square resistance (Delta Technologies, LTD) were first patterned using photolithography and etched in a mixture of hydrochloric acid, nitric acid, and water. This left two 2.3 mm wide ITO strips near the middle of the glass substrate. The patterned ITO substrates were cleaned with acetone, isopropanol, and distilled water, and treated with an oxygen plasma for 10 minutes to clean the substrate surface and make it hydrophilic [13]. Roughly 50 nm of poly(3,4- ethylenedioxy thiophene)/poly(styrenesulfonate) (PEDOT:PSS) (H. C. Starck) was spun onto the oxygen-plasma-treated ITO substrates. Excess water was then removed from the PEDOT:PSS film by baking at 130˚ C for 5 minutes. P3HT (Rieke Metals, Inc) was dissolved in a DCB solution which contained a known quantity of Si NCs. The Si NCs/P3HT solution was then sonicated a second time and spun on top of the PEDOT:PSS layer in a glove box to form a film approximately 100 nm thick. Finally, 2 mm wide aluminum (Al) electrodes (100 nm thick) were evaporated on top of the Si NCs/P3HT film to complete the thin film solar cells. A schematic in Figure 3-1b illustrates the device configuration. The active area of each device is 0.046 cm^2.

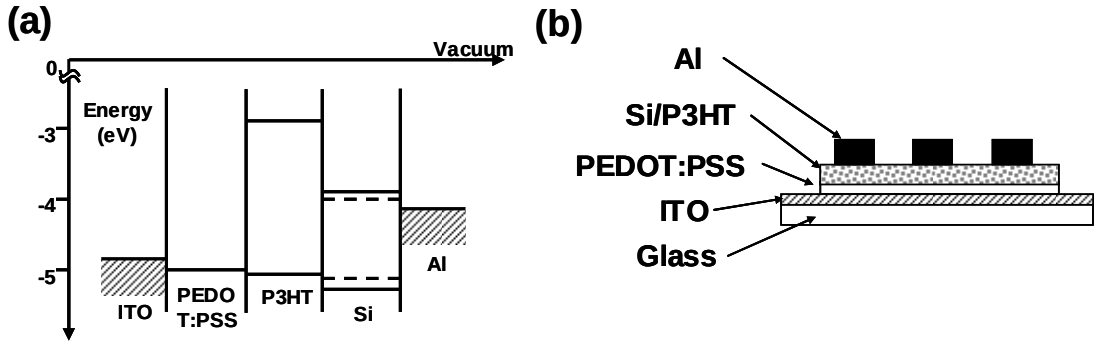

Figure 3-1. (a) Energy band diagram of a Si NCs/P3HT solar cell. The dotted lines represent the valence and conduction bands of bulk Si, while the solid lines are representative of 4 nm Si NCs. (b) Schematic of a Si NCs/P3HT hybrid solar cell. Thin films of PEDOT: PSS and Si NCs/P3HT were spun sequentially on transparent ITO substrates. Aluminum metal electrodes (100 nm thick) were deposited on the top.

3.4 Results and Discussion

Figure 3-2 shows current-voltage (I-V) characteristics of typical Si NCs/P3HT (main figure) and P3HT-only (inset) devices both in the dark and under AM 1.5 direct solar irradiation. For all devices—which were illuminated through the ITO side—diode behavior was seen in the dark and in the light. Predictably, P3HT-only devices exhibit little photoactivity since the lack of an electron-accepting material means any built-in potential must arise from the junctions with the electrodes. By contrast, devices in which Si NCs are included have shown PCEs above 1.1%.

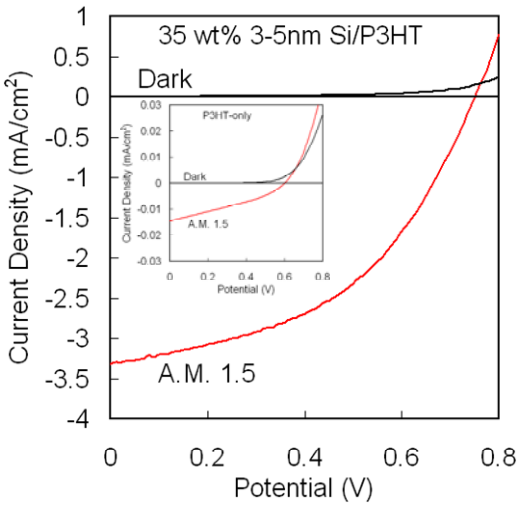

Figure 3-2. Current-voltage characteristic (I-V) of a 35wt% 3-5 nm Si NCs/P3HT solar cell (main window) and P3HT-only solar cell (inset). The I-V characteristic of the hybrid device was recorded under 100 mW/cm^2 AM 1.5 direct conditions and shows 1.15% PCE and a fill factor of 0.46 with 3.3 mA/cm^2 short circuit-current density and 0.75 V open-circuit voltage. The current densities of the P3HT-only device are roughly two orders of magnitude smaller than for the hybrid device.

To understand the role of the Si NCs in these solar cells, device performance was studied as a function of Si NCs/P3HT ratio for each of the three Si NC size groups (Figure 3-3). Figure 3-3a indicates that the open-circuit voltage (V_{oc}) is inversely related to NC size, regardless of the materials ratio. This dependence clearly indicates that the Si NCs play an active role in exciton dissociation. We believe the inverse trend is due to a widening of the Si NC bandgap, which can be observed in the blue-shift of the photoluminescence for sizes below about 10 nm [11]. An opening of the Si NC band gap

results in a smaller conduction band offset between the Si NCs and P3HT (Figure 3-1a), resulting in less voltage lost during exciton dissociation.

Short-circuit current (I_{sc}) also increases with decreasing Si NC size (Figure 3-3b). This result is surprising. Fewer interparticle hopping events should be required to transport an electron to the Al electrode in devices with larger Si NCs, enhancing electron transport. A corresponding increase in I_{sc} is not observed, suggesting that electron transport through the Si NCs is not the limiting factor in the devices. Instead, the current could be limited by a bottleneck in the hole transport material, P3HT, or the efficiency of exciton dissociation could decrease rapidly with increasing Si NC size. Assuming a mobility of 10^{-5} cm^2/Vs and a device thickness of 100 nm, the diffusion time of holes in P3HT is on the order of 100 μs. Transport in P3HT may be limiting I_{sc} if this time is comparable to or longer than the trapping or recombination times. It is also probable that exciton dissociation is enhanced in devices with smaller Si NCs due to their greater surface-area-to-volume ratio and wider bandgap, and this may play a role in the observed trend in I_{sc}.

For all Si NC sizes, I_{sc} peaks when the Si NCs/P3HT weight ratio is between 30-70%. This likely occurs because a balance between electron and hole transport material must be struck, and the interfacial area between them maximized. However, film morphology also plays a role. Scanning electron microscopy (SEM) was performed on Si NCs/P3HT films spun onto gold-coated Si wafer chips which were used to avoid sample charging. SEM image analysis shows films that are 100-200 nm thick on average, but that have non-uniform distributions of Si NCs and therefore non-homogeneous surfaces (Figure 3-4). For high Si NC concentrations, Si NC agglomeration seriously deteriorates film uniformity and is expected to decrease I_{sc} because of increased film resistance. Solar cells with Si NCs/P3HT weight ratios greater than 55% for 3-5 nm Si NCs and 65% for 5-9 nm Si NCs could not be fabricated because the solution viscosity increased until spin-coating a macroscopically uniform film is no longer feasible.

The measured fill factor was nearly independent of Si NC size and the Si NCs/P3HT ratio (Figure 3-3c). As a result, the calculated PCEs follow the trends observed in V_{oc} and I_{sc}, and are shown in Figure 3-3d. It should be noted that these results are reproducible, with greater than 90% yield rate of functional devices. The best solar cell

performance was obtained for 35wt% Si NCs that were 3-5 nm in diameter. This cell had a 1.15% PCE and a fill factor of 0.46, with I_{sc} of 3.3 mA/cm^2 and V_{oc} of 0.75 V.

The incident-photon-to-current-conversion efficiency (IPCE) for the 35wt% 3-5 nm device is shown in Figure 3-5. The device is most efficient near 500 nm, where the IPCE is 26%. In order to understand the spectral dependence observed in the IPCE, the optical absorption spectra of P3HT only, Si NCs only, and Si NCs/P3HT films on quartz substrates were measured and are displayed in Figure 3-6. P3HT has a strong absorption band between 450-650 nm. Silicon nanocrystals have little absorption in the visible compared to P3HT, with the absorption coefficient of bulk Si only one-tenth of that of P3HT at 500 nm [14,15]. However, Si NCs absorb strongly in the UV, complementing the absorption of P3HT. In the P3HT-only film, the maximum absorption is located at 560 nm, but the Si NCs/P3HT film peaks at 520 nm due to the additional absorption by Si NCs. Comparing the absorption spectra with the IPCE spectrum in Figure 3-5, we see that most of the collected current results from P3HT absorption, although Si NC absorption appears to boost the IPCE below 500 nm.

3.5 Conclusion

In summary, we have demonstrated Si NCs/P3HT solar cells fabricated by spin-coating blends of Si NCs and P3HT onto ITO-coated glass substrates. An optimatization of Si NC size and Si NCs/P3HT ratio showed that small Si NC sizes and roughly 35wt% Si NCs produced the best devices, with efficiencies as high as 1.15%. Both open-circuit voltage and short-circuit current improved with decreasing size, suggesting that larger interfacial area and nanocrystal bandgap aid device performance. In these devices, visible light absorption and exciton generation in P3HT is the primary source of photocurrent, and Si NCs only contribute to current generation in the UV. Non-uniform film morphologies were observed in SEM due to Si NC agglomeration, and this is expected to reduce device efficiency. Despite this limitation, our device performance indicates that Si NCs are a good candidate for future organic-inorganic hybrid solar cells, especially given the lack of toxicity and elemental abundance of Si.

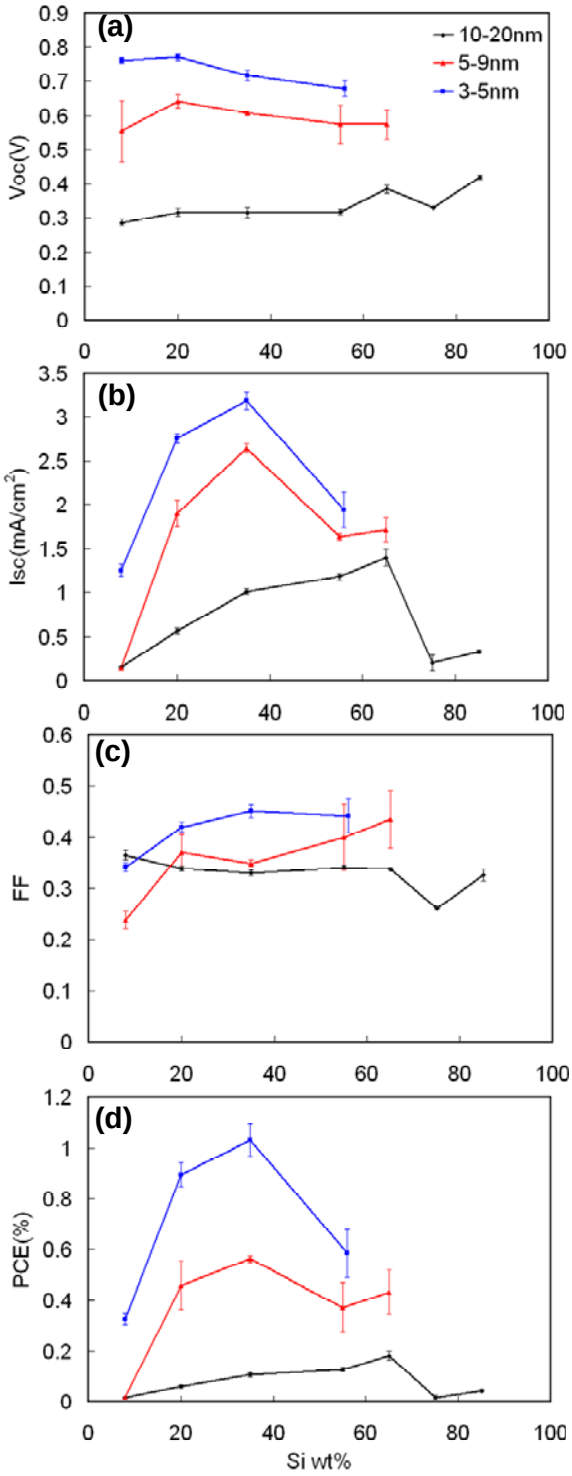

Figure 3-3. Silicon NCs/P3HT solar cell performance for devices with different Si NCs/P3HT ratios and NC sizes. 3-5 nm, 5-9 nm and 10-20 nm Si NCs are represented with blue squares, red triangles, and black diamonds, respectively. Each data point and associated error bar represents an average value and standard deviation from a set of six devices on one substrate. Defective devices, which comprise less than 10% of all devices, are ignored.

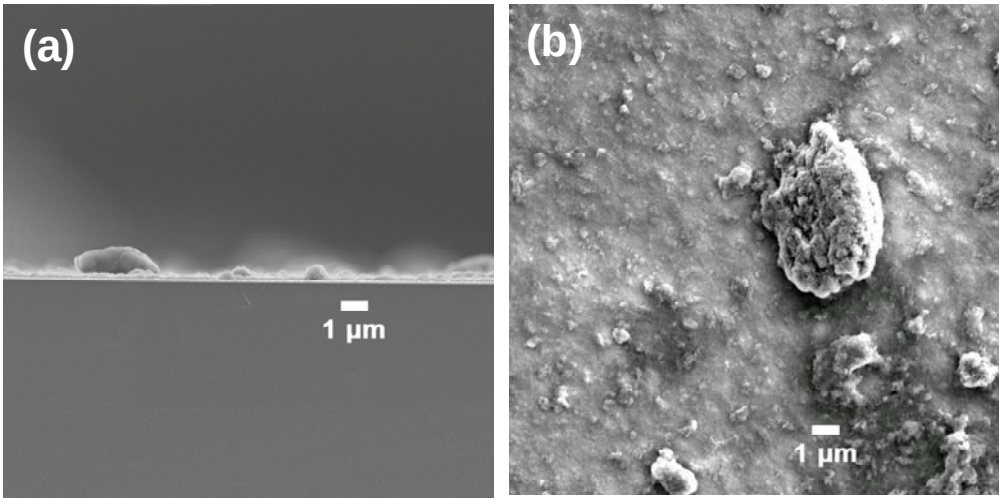

Figure 3-4. SEM images of 35wt% 3-5 nm Si NCs/P3HT films. (a) A cross-section shows film thickness variation which may deteriorate solar cell efficiency. (b) A top-view image shows Si NC agglomerates larger than 1 μm in size.

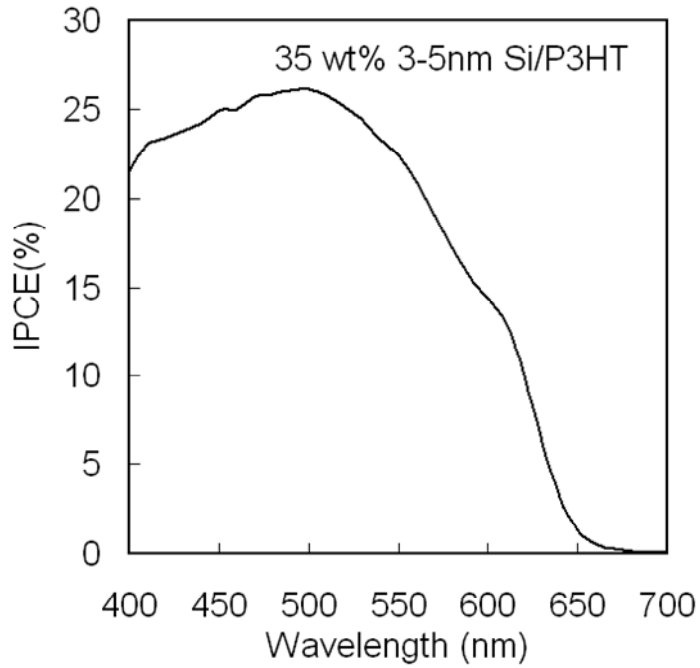

Figure 3-5. Incident photon-to-current-conversion efficiency spectrum of a 35wt% 3-5 nm Si NCs/P3HT solar cell.

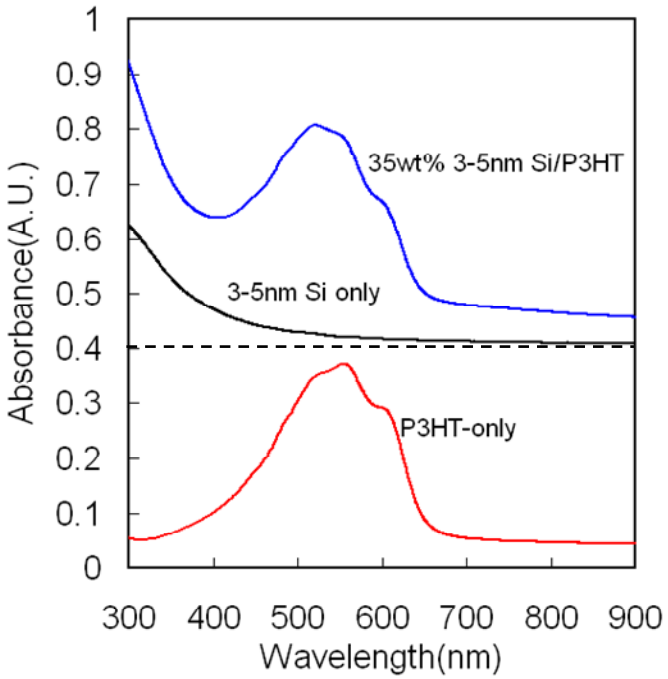

Figure 3-6. Room-temperature optical absorption spectra of P3HT, Si NCs, and 35wt% 3-5 nm Si NCs/P3HT films on quartz. The absorbance of the Si NCs/P3HT film below 400 nm is due to Si NCs. Dashed line represents the reference line for Si NCs and 35wt% 3-5 nm Si NCs/P3HT films.

3.6 References

[1] N. C. Greenham, X. Peng, and A. P. Alivisatos, *Phys. Rev. B*, **54**, 17628 (1996).

[2] W. J. E. Beek, M. M. Wienk, and R. A. J. Janssen, *Adv. Funct. Mater.* **16**, 1112 (2006).

[3] C. Y. Kwong, W. C. H. Choy, A. B. Djurišić, P. C. Chui, K. W. Cheng, and W. K. Chan, *Nanotech.* **15**, 1156 (2004).

[4] S. Günesa, K. P. Fritz, H. Neugebauer, N. S. Sariciftci, S. Kumar, and G. D. Scholes, *sol. Energy Mater. Sol. Cells*, **91**, 420 (2007).

[5] D. Cui, J. Xu, T. Zhu, G. Paradee, S. Ashok, and M. Gerhold, *Appl. Phys. Lett.* **88**, 183111 (2006).

[6] E. Arici, N. S. Sariciftci, and D. Meissner, *Adv. Funct. Mater.* **13**, 165 (2003).

[7] W. U. Huynh, J. J. Dittmer, and A. P. Alivisatos, *Science*, **295**, 2425 (2002).

[8] I. Gur, N. A. Fromer, C. P. Chen, A. G. Kanaras, and A. P. Alivisatos, *Nano Lett.* **7**, 409 (2007).

[9] V. Gowrishankar, S. R. Scully, and M. D. McGehee, *Appl. Phys. Lett.* **89**, 252102 (2006).

[10] A. A. D. T. Adikaari, D. M. N. M. Dissanayake, R. A. Hatton, and S. R. P. Silva, *Appl. Phys. Lett.* **90**, 203514 (2007).

[11] L. Mangolini, E. Thimsen, and U. Kortshagen, *Nano Lett.* **5**, 655 (2005).

[12] W. Martienssen, Ed.,and M.D. Lechner, Ed., *Static Dielectric Constants of Pure and Binary Liquid Mixtures*, Landolt-Börstein series, **17**, Supplement to IV/6, Springer (2008).

[13] J. S. Kim, M. Granstrom, R. H. Friend, N. Johansson, W. R. Salaneck, R. Daik, W. J. Feast, and F. Cacialli, *J. Appl. Phys.* **84**, 6859 (1998).

[14] S. Adachi, *Optical Constants of Crystalline and Amorphous Semiconductors: Numerical Data and Graphical Information*, Springer, 29 (1999).

[15] S. S. Sun, and N. S. Sariciftci, *Organic Photovoltaics: Mechanisms, Materials, and Devices*, Taylor & Francis, 535 (2005).

Chapter 4

Optimization of Si NCs/P3HT Hybrid Solar Cells

4.1 Overview

Silicon nanocrystals (Si NCs) have been proven to be an electron acceptor in hybrid solar cells combining Si NCs with poly-(3-hexylthiophene) (P3HT). The effects of annealing and different metal electrodes on Si NCs/P3HT hybrid solar cells were studied in this chapter. After annealing at 150 °C, Si NCs/P3HT solar cells exhibit power conversion efficiencies as high as 1.47%. The hole mobility of P3HT increase from 2.48×10^{-10} $m^2V^{-1}s^{-1}$ to 1.11×10^{-9} $m^2V^{-1}s^{-1}$ after annealing. The one order of magnitude increase in hole mobility suggests an improved crystallinity of the P3HT film, which can enhance the hybrid device efficiency. A quenching of the open-circuit voltage and short-circuit current was observed when high work function metals were deposited as the cathode on Si NCs/P3HT hybrid devices.

4.2 Introduction

The high cost of inorganic crystalline solar cells is the driving force behind the research of low-cost thin-film solar cells. Polymer-based solar cells have attracted a considerable amount of attention due to solution-phase processing. The solution-phase processing offers great potential for inexpensive large-scale solar cell manufacturing, in which organic semiconductors can be printed, spin-cast or sprayed onto the substrate. Solar cells should consist of materials with absorption spectra which capitalize on the solar spectrum. The band gap of polymers can be varied by changing the polymer structure and synthesis process; therefore, it is possible to tailor the absorption spectra of polymer-based solar cells. The binding energy of excitons in polymers is around 0.4 eV,

which is much larger than the thermal energy available at room temperature, resulting in inefficient exciton dissociation in pristine polymers [1]. However, the exciton dissociation efficiency can be enhanced by incorporating electron acceptors into a polymer matrix. The electron affinity of electron acceptors should be larger than the electron affinity of polymers so that excitons can be separated by transferring the electron into the electron accepting material. In addition, the highest occupied molecular orbital (HOMO) of polymers should be higher than that of electron acceptors to prevent the transfer of holes to the electron acceptor. Various electron acceptors have been reported for solar cell fabrication, including conjugated polymers [2], fullerenes [3], and inorganic nanocrystals [4].

Inorganic nanocrystals with a band structure which aligns favorably with that of polymers can be efficient electron acceptors and may not compromise solution-phase processing. Inorganic nanocrystals can also have properties which differ from bulk materials due to quantum confinement. For example, it is possible to tune the absorption spectra of nanocrystals by changing their size [5]. Hybrid solar cells based on mixtures of conjugated polymers and inorganic semiconductor nanocrystals can provide a new route for solar energy applications by combining advantages of organic and inorganic semiconductors in the same device. Hybrid solar cells consisting of polymer and cadmium selenide (CdSe) [4], titanium dioxide (TiO_2) [6], or zinc oxide (ZnO) [7] nanocrystals have been reported. Recently, silicon nanocrystals (Si NCs) have also been used as an electron acceptor in combination with poly-(3-hexylthiophene) (P3HT) [8]. By reducing the Si NC size from 20 nm to 3 nm, Si NCs/P3HT hybrid solar cells show increasing short-circuit current (I_{sc}) and open-circuit voltage (V_{oc}) due to strong quantum confinement and increasing surface-area-to-volume ratios in the Si NCs. To further improve the power conversion efficiency (PCE) of Si NCs/P3HT hybrid solar cells, the effects of annealing temperature, annealing period, and different metal cathodes were studied in this chapter. After the optimal annealing temperature and period were found, the hole mobility of P3HT was also measured before and after annealing by using a high work function metal to block electron injection. The observed change in mobility is used to explain the changes in solar cell performance after annealing.

4.3 Experimental

Silicon nanocrystals of 3-5 nm diameter were synthesized in a non-thermal RF plasma with a frequency of 13.56 MHz and a power of 135 W [9]. The flow rates of precursors were 33 standard cubic centimeters per minute (SCCM) of 5% silane/helium, 150 SCCM of argon, and 6 SCCM of hydrogen at 3.5 Torr. Regioregular P3HT (electronic grade, 4002-E from Rieke Metals, Inc.) with a molecular weight of 50000-55000 g mol^{-1} was dissolved in 1,2-dichlorobenzene (DCB, ACROS) and stirred on a hot plate at 55 °C for 120 minutes before mixing with Si NCs. After Si NCs were collected downstream of the plasma on a stainless steel mesh, a blend solution of 50:50wt % Si NCs:P3HT was prepared by adding Si NCs into the P3HT solution in DCB. To minimize oxidation, Si NC handling and solution preparation processing were conducted in a glove bag (oxygen level < 25 ppm) and a glove box (oxygen and moisture level < 1 ppm).

Si NCs/P3HT hybrid devices were prepared on indium tin oxide (ITO, 8 to 12 Ω/square resistance, Delta Technologies, LTD) coated glass substrates (25 mm x 20 mm). A hole-conducting layer of PEDOT:PSS (Baytron P VP Al 4083 grade from H. C. Starck) was spin-coated under ambient conditions. Before PEDOT:PSS was spin-coated, the ITO substrates were cleaned with acetone, isopropanol, and distilled water, and were dried at 160 °C for 5 minutes. To provide good contact between the ITO and PEDOT:PSS, the ITO substrates were treated with an UV-Ozone cleaner for 10 minutes to clean the substrate surface and make it hydrophilic. The PEDOT:PSS film was spun onto the ITO at 4000 rpm for 60 seconds twice. After spin-coating, the PEDOT:PSS coated ITO substrates were dried at 130 °C for 5 minutes to remove any residual water inside the PEDOT:PSS film. To make uniform Si NCs/P3HT hybrid devices, the blend solution of 50wt% Si NCs/P3HT was sonicated for 10 minutes before the spin-coating process. After sonication, the blend solution was spin-coated immediately onto the top of the PEDOT:PSS layer in a glove box to reduce the agglomeration of Si NCs. To complete the hybrid solar cells, different work function metals were deposited by thermal evaporation under vacuum (< $2x10^{-6}$ Torr). The active area of the solar cell is 0.046 cm^2.

4.4 Results and Discussion

Low carrier mobility is one factor limiting polymer-based solar cell PCEs [10]. When carrier mobility is low, there is a higher probability of recombination before carriers reach the electrodes. For example, the recombination probability increases with the build-up of space charge in a polymer-based solar cell [11]. In P3HT/ [6,6]-phenly C_{61}-butyric acid methyl ester (PCBM) blend solar cells, the increasing hole mobility in the P3HT phase of the blend leads to a strong enhancement of solar cell efficiency [10]. Similarly, the efficiency of Si NCs/P3HT hybrid solar cells can be improved by increasing the hole mobility in the P3HT phase. The degree of crystallinity in the P3HT phase of the blend structure affects the hole mobility in the film [10]. P3HT tends to form microcrystalline structures due to its self-organizing nature but the microstructure of P3HT is affected by regioregularity [12], molecular weight [13], and solvent choice [14]. Regioregularity and molecular weight are determined by the vendor and would be difficult to alter by common processes. Typically, a high boiling point (bp) solvent and annealing treatment are used to improve the P3HT carrier mobility via crystallization [14, 15]. Chloroform is a commonly used solvent in P3HT devices; however, chloroform has a low bp, which causes rapid evaporation and limits the crystallization time during spin-coating. The field-effect mobility of P3HT films made from chloroform is typically on the order of 0.01 $cm^2\ V^{-1}s^{-1}$. By using high bp solvents, such as 1, 2, 4-trichlorobenzene, the field-effect mobility of P3HT film can be increased to 0.12 $cm^2\ V^{-1}s^{-1}$[14]. The influence of solvent selection in TiO_2/P3HT hybrid solar cells was reported by Kwong *et al.*[15]. Hybrid solar cells of TiO_2/P3HT were made using xylene, chlorobenzene, tetrahydrofuran, and chloroform under the same fabrication conditions. TiO_2/P3HT solar cells made from xylene, a relatively high bp solvent, displayed the best efficiency.

For Si NCs/P3HT solar cell fabrication, we found that low bp solvents cannot be a proper mediator for Si NCs/P3HT thin film fabrication. The surfaces of Si NCs from our plasma reactor are terminated with hydrogen. This hydrogen-terminated surface does not provide solubility in common non-polar solvents. Low bp solvents have fast evaporation rates and thin films made from the low bp solvents must be fabricated at high spin-

casting speeds. The high speed fabrication process is unable to provide a continuous Si NCs/P3HT film because of the poor solubility of the Si NCs. In this study, 1, 2-dichlorobenzene (DCB) was used because we observed that bare Si NCs in DCB have less flocculation. Another advantage of using DCB is that it allows us to use a low spin-casting speed, which provides continuous film morphology because of its relatively high bp [8]. Third, using DCB allows the P3HT to crystallize during the slow drying of the DCB [14, 16].

The literature reports that the crystallization of P3HT can be enhanced by annealing films at a temperature higher than the P3HT glass-transition temperature [17]. For P3HT hybrid solar cells, annealing temperatures of 80 °C [7], 110 °C [15], 120 °C [18], and 135 °C [19] have been reported. Reported annealing periods vary from 5 minutes to 24 hours for ZnO/P3HT [7], TiO2/P3HT [15], CdSe/P3HT [18], and amorphous-silicon/P3HT hybrid solar cells [19]. To optimize the performance of Si NCs/P3HT devices, it is necessary to examine various annealing temperatures and periods. The SEM image of a 50wt% Si NCs/P3HT film shown in Figure 4-1 indicates that agglomeration of Si NCs results in non-uniform film morphology which could also affect solar cell performance.

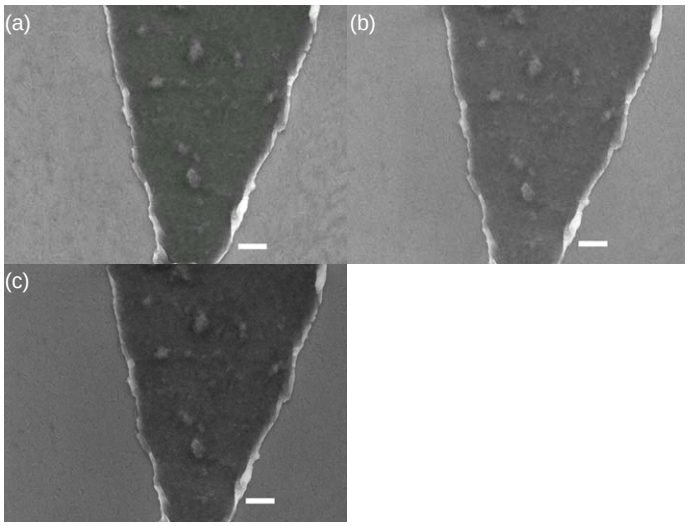

Figure 4-1. SEM images of 50wt% 3-5 nm Si NCs/P3HT films show Si NC agglomerates larger than 1 μm in size before and after annealing. Annealing does not change the macroscopic morphology. (a) As-cast film (b) 150 °C anneal for 120 minutes (c) 200 °C anneal for 120 minutes. Scale bar, 1 um.

4.4.1 Annealing Effect

The hybrid solar cells of 50wt% Si NCs/P3HT with aluminum (Al) electrodes were annealed at 100 °C to 200 °C for different annealing periods (5 minutes, 30 minutes, and 120 minutes) in a glove box. Sixteen substrates were fabricated from the same blend of solution under the same conditions, and each substrate had six devices. Figure 4-2 shows device performance as a function of annealing temperatures and periods under air mass 1.5 direct (AM 1.5D) solar irradiation (100 mW/cm^2). Figure 4-2a indicates that the V_{oc} is nearly independent of annealing temperature and period. The slight variation may come from sample inhomogeneities arising from the non-uniform film morphology. The maximum I_{sc} was obtained at an annealing temperature of 150 °C for 120 minutes. For temperatures lower than 150 °C, I_{sc} increases with increasing annealing time. For temperatures higher than 150 °C, I_{sc} decreases with increasing annealing time. Fill factor (FF) also increases slightly with increasing annealing time at different temperatures (Figure 4-2c). As a result, the calculated PCEs follow the trends observed in I_{sc} and FF, and are shown in Figure 4-2d. The peak PCE happens when the devices are annealed at 150 °C for 120 minutes.

The phenomena that the performance of Si NCs/P3HT devices decreases at annealing temperatures higher than 150 °C may be explained by a change in microscopic film morphology. We know of no literature about morphology changes in hybrid solar cells after annealing. For P3HT/PCBM solar cells, there are reports in the literature that high temperature annealing or long annealing periods can change the microscopic film morphology. Huang *et al.* reported that a long annealing period (140 °C, 60 minutes) could cause aggregation of PCBM and reduce the solar cell efficiency [20]. Li *et al.* reported that high temperature annealing (180 °C) could decrease film roughness and reduce the solar cell efficiency [21]. This may explain why higher temperature annealing and longer annealing periods for Si NCs/P3HT devices reduce solar cell efficiency. Roughness probing is a challenge for our Si NCs/P3HT devices because the film morphology has variations in the micrometer range. A significant roughness change on the micrometer scale of Si NCs/P3HT film was not observed in SEM even after annealing

at 200 °C for 120 minutes (Figure 4-1). However, microscopic restructuring of the P3HT phase is likely at these temperatures.

The most common annealing temperature for hybrid solar cells or P3HT/PCBM devices is between 100 and 150 °C. From this perspective, an optimal annealing temperature of 150 °C for Si NCs/P3HT devices is reasonable. The optimal annealing time of 120 minutes is longer than is commonly used for P3HT/PCBM blend devices (4 - 30 minutes) [10, 20, 21] and shorter than some researchers have used for CdSe/P3HT or TiO_2/P3HT devices (2 hours - 24 hours) [15, 18]. We believe we are the first to report the effects of annealing time in P3HT hybrid solar cells, and it is clear that the annealing time plays an important role in determining I_{sc}. The optimal annealing time likely depends on the film morphology, as we attribute the improved device performance to P3HT crystallization and crystal growth may be slowed or impeded by NC agglomerates into which the P3HT penetrates.

Figure 4-3 shows current-voltage (I-V) characteristics of the 50wt% Si NCs/P3HT device under AM1.5D solar irradiation (100 mW/cm^2) before and after 150 °C annealing for 120 minutes. This cell had a 1.47% PCE and a FF of 0.47, with I_{sc} of 3.8 mA/cm^2 and V_{oc} of 0.8 V. The incident-photon-to-current-conversion efficiency (IPCE) for this device before and after annealing is shown in Figure 4-4 and has a maximum of 30% after annealing near the P3HT peak absorption at 500 nm. The optical absorption spectrum of a 50wt% Si NCs/P3HT film before and after 150 °C annealing for 120 minutes is shown in Figure 4-5. The optical absorption spectrum does not show significant change before and after annealing. There is a slight increase for wavelengths below 510 nm after annealing. The small increase may result from annealing, but may just be from scattering. It should be noted that the rough morphology of Si NCs/P3HT films may cause scattering and affect the accuracy of absorption spectra before and after annealing. For P3HT/PCBM solar cells, there is usually a significant red-shift in absorption after annealing due to increasing interchain interaction among the P3HT chains [21]. Although a red-shift in the absorption spectrum of the Si NCs/P3HT film was not observed after annealing, IPCE still indicated a slight red-shift.

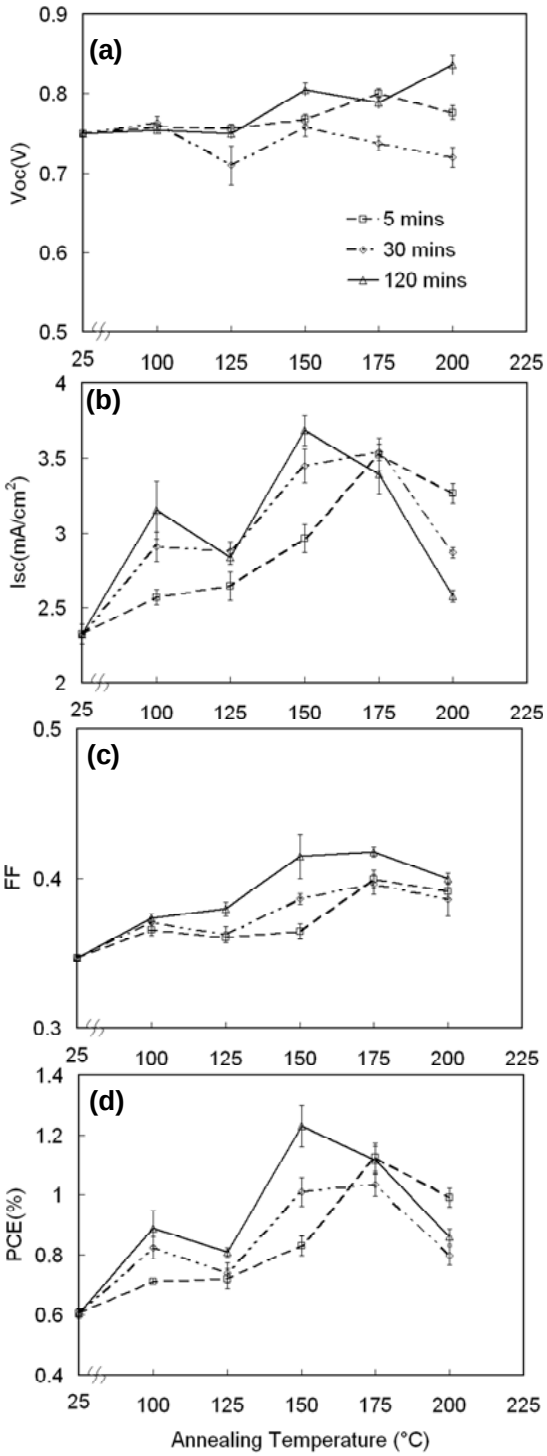

Figure 4-2. Hybrid solar cell performance of 50wt% 3-5 nm Si NCs/P3HT devices with different annealing temperatures (100, 125, 150, 175, 200 °C) and periods (5, 30, 120 minutes). 5minutes, 30 minutes ,and 120 minutes annealing periods are represented with squares, diamonds, and triangles, respectively. Each data point and associated error bar represents an average value and standard deviation from a set of six devices on one substrate.

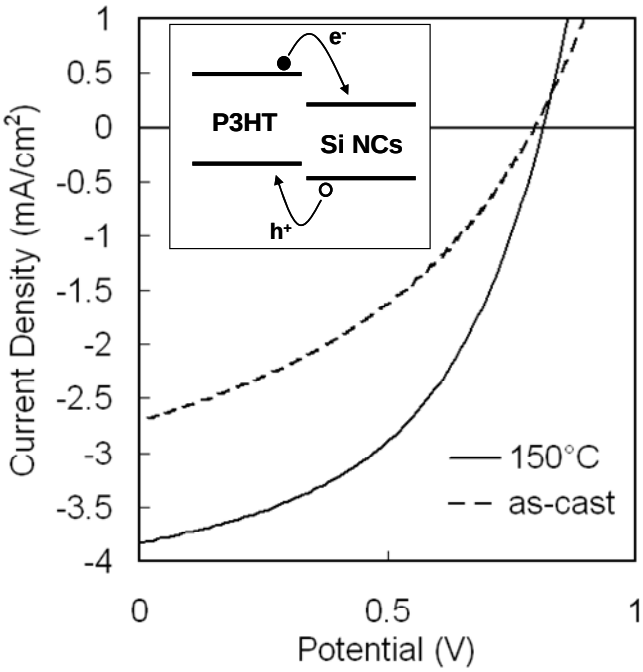

Figure 4-3. Current-voltage characteristic (I-V) of a 50wt% 3-5 nm Si NCs/P3HT solar cell (main plot) before and after 150 °C annealing for 120 minutes. The dashed and solid lines represent before and after annealing. The I-V characteristic of the hybrid device was recorded under 100 mW/cm^2 AM 1.5D conditions and shows 1.47% PCE and a FF of 0.47 with 3.8 mA/cm^2 I_{sc} and 0.8 V V_{oc}. The inset shows the energy band levels of the Si NCs and P3HT.

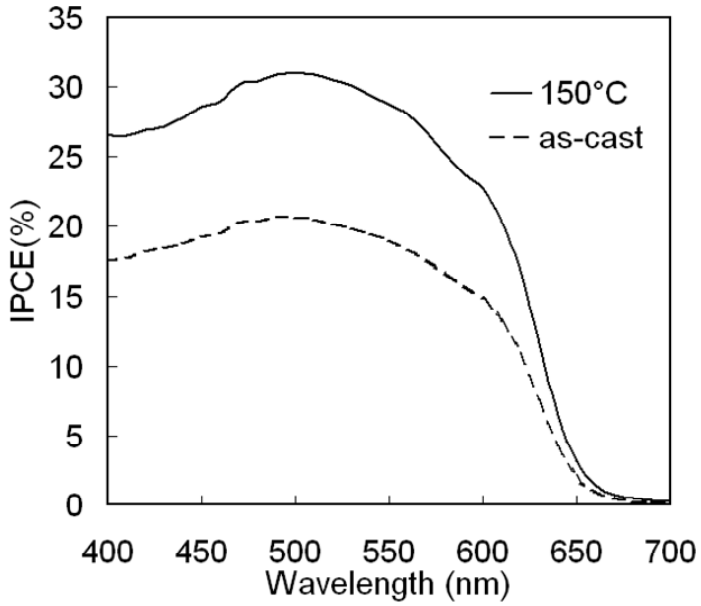

Figure 4-4. Incident-photon-to-current-conversion efficiency spectrum of a 50wt% 3-5 nm Si NCs/P3HT solar cell before and after annealing at 150 °C for 120 minutes. The dashed and solid lines represent the IPCE before and after annealing. There is a slight red-shift in the IPCE curve after annealing.

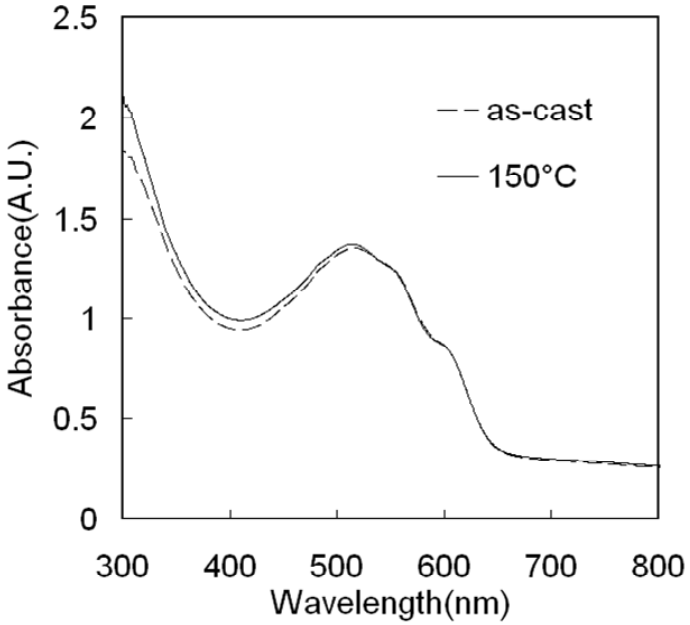

Figure 4-5. Room-temperature optical absorption spectra of 50wt% 3-5 nm Si NCs/P3HT films on quartz before and after annealing at 150 °C for 120 minutes. The absorbance of the Si NCs/P3HT film below 400 nm is due to the Si NCs. The dashed and solid lines represent the absorption spectra before and after annealing. There is not a significant change in absorption after annealing.

4.4.2 Hole Mobility Measurement

In order to understand carrier transport within polymer-based solar cells, Melzer *et al.* changed the cathode or anode metals to achieve hole-transport-only or electron-transport-only devices with the same solar cell architecture [22]. The dark current of P3HT is space-charge-limited, which provides a direct measurement of hole mobility from the I-V measurement [10]. However, Si NCs/P3HT blend devices with PEDOT:PSS and Al contacts would result in a combined current from electrons and holes. In order to measure the hole-only space-charge-limited-current (SCLC), the Al electrode should be replaced by the high work function metal to block electron injection into the Si NCs. Gold (Au) was used for this study. The Frenkel effect, in which the effective depth of shallow traps can be reduced by high electric fields, was considered. The SCLC equation with the Frenkel effect results in a much greater current than the Mott-Gurney Law at high electric fields. The Frekel effect SCLC equation can be written as [10]:

$$J_h = \frac{9}{8}\varepsilon_0\varepsilon_r\mu_h \exp(0.891\gamma_h\sqrt{\frac{V_{\text{int}}}{L}})\frac{V_{\text{int}}^{\ 2}}{L^3} \tag{4.1}$$

where J_h is the hole current-density, ε_0 is the vacuum permittivity (8.85×10^{-12} A s V^{-1} m^{-1}), ε_r is the relative dielectric constant, μ_h is the zero-field hole mobility, γ_h is the field activation parameter, and L is the thickness of the active layer. The internal voltage drop between the two electrodes is denoted as V_{int} and can be expressed as

$$V_{int}=V-V_{bi}-V_{Rs} \tag{4.2}$$

where V_{bi} is the built-in voltage drop caused by the work function difference between electrodes, and V_{Rs} is the voltage drop from the series resistances of the substrates. The V_{bi} between PEDOT:PSS (5 eV) and Au (5.1 eV) is 0.1 V and the series resistance of PEDOT:PSS on ITO is 75 Ω in our study. The relative dielectric constant ε_r of P3HT is taken as 2.6 [23].

For our experiments, there were six hole-transport-only devices on each substrate. Figure 4-6 shows experimental hole-only I-V data of a 50wt% Si/P3HT film 150 nm thick. The solid lines represent the fitting results from Equation 4.1. Before annealing, the zero-field hole mobility found from the fit was $2.2\text{x}10^{-10}$ $m^2V^{-1}s^{-1}$ with $\gamma_h=8.04\text{x}10^{-4}$ $(mV^{-1})^{0.5}$. After annealing at 150 °C for 120 minutes, the hole mobility increased to $1.4\text{x}10^{-9}$ $m^2V^{-1}s^{-1}$ with $\gamma_h=3.81\text{x}10^{-4}$ $(mV^{-1})^{0.5}$. The non-uniform film morphology caused by NC incorporation is expected to vary the experimental values of the hole mobility measurement on different devices. The average hole mobilities out of six devices before and after annealing at 150 °C for 120 minutes were $2.48\ \text{x}10^{-10}$ and $1.11\text{x}10^{-9}$ $m^2V^{-1}s^{-1}$. The mobility change in P3HT/PCBM films cast from chloroform was studied by Mihailetchi *et al.* as a function of annealing temperature [10]. P3HT/PCBM films had a hole mobility of $2\text{x}10^{-12}$ $m^2V^{-1}s^{-1}$ without annealing and increased to $9\text{x}10^{-9}$ $m^2V^{-1}s^{-1}$ after annealing at 130°C. As-cast Si NCs/P3HT films have a higher mobility than as-cast P3HT/PCBM films because the slow-drying DCB enhances the crystallinity of the P3HT film. It is understandable that Si NCs/P3HT films have a lower hole mobility than P3HT/PCBMs films after annealing because Si NCs agglomerates are larger than PCBM and can interrupt the propagation of P3HT crystals more than PCBM [24]. Control devices with P3HT only were made under the same fabrication conditions. The P3HT-

only as-cast film had an average mobility of 2.65×10^{-8} $m^2V^{-1}s^{-1}$ (γ_h=0), which show that the hole mobility decreases in the presence of Si NCs.

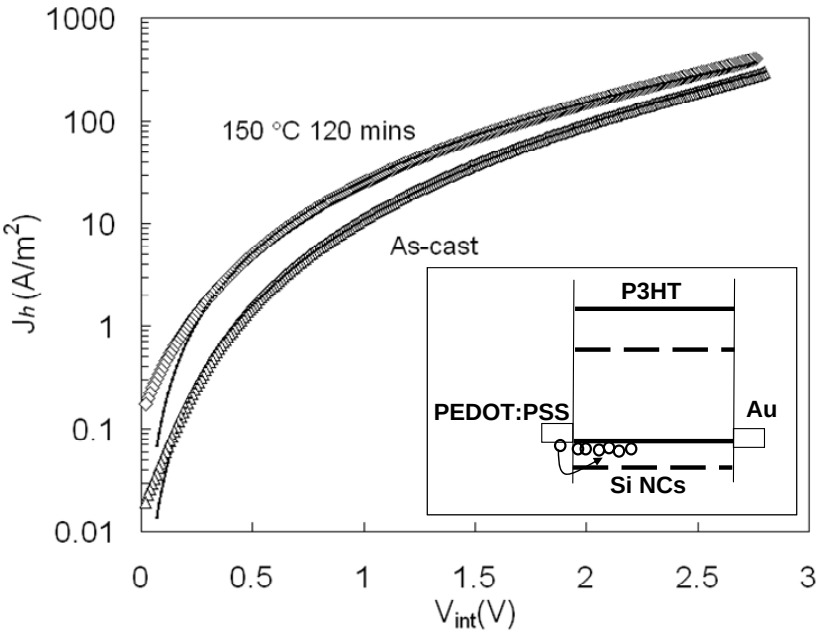

Figure 4-6. Current density-voltage characteristic of a hole-transport-only device of 50wt% 3-5 nm Si NCs/P3HT (active layer thickness around 150 nm) before and after 150 °C annealing for 120 minutes. The as-cast and 150 °C annealed data are represented with triangles and diamonds, respectively. The solid lines present the fits to the measurement data from Equation 4.1. The inset shows the device configuration.

We also tried to use low work function metals, such as magnesium (Mg), calcium (Ca), and samarium (Sm), as the cathode and anode to measure the electron mobility between Si NCs. Two sets of devices of 50wt% Si NCs/P3HT and P3HT-only (control sample) were made with the same fabrication conditions. For both device types, it was observed that the top electrode had better electron injection than the bottom electrode because there was no adhesion layer, such as PEDOT:PSS, between the active layer and the bottom electrode. At the same voltage, the current in the Si NCs/P3HT devices was higher than in the P3HT-only devices. This implies that we successfully made electron-transport-only devices by blocking hole transport in the P3HT phase. However, these devices broke down around 1 V and we were not able to determine the electron mobility from the low voltage data. We attribute the breakdown to the poor contact between the film and the bottom electrode.

4.4.3 Cathode Metal Effect

It has been shown that polymer-based solar cell characteristics can be affected by cathode metal selection [25, 26, 27, 28]. There is not a consistent explanation for how the V_{oc} changes with different cathode metals across different architectures of polymer-based solar cells. For a single layer polymer-based photodiode made by poly(2-methoxy-5-(2'-ethylhexyloxy)-1,4-phenylenevinylene), the V_{oc} scales with the work function difference between the two electrodes [25]. In the bilayer structures of electron- and hole-accepting polymers, the V_{oc} also scales with the electrode work function difference [26]. The device V_{oc} for a bilayer of poly(9,9'-dioctylfluorene -co-benzothiadiazole) (electron accepting polymer) and poly(9,9',dioctylfluorene-co-bis-N,N'-(4-butylphenyl)-bis-N,N'-phenyl-1,4-phenylenediamine) (hole accepting polymer) decreased from 1.5 V to 0.7 V by replacing an Al electrode with a Au electrode. However, in the blend system of electron- and hole-accepting polymers, the significant change in V_{oc} with different work function metals was not observed [27]. The V_{oc} of the blend system from poly[2-methoxy-5-(3′,7′-dimethyloctyloxy)-1,4 -phenylene vinylene] and PCBM only varied by 0.16 V when the electrodes were changed from Au to Ca. Brabec *et al.* explain that this slight decrease in V_{oc} comes from pinning of the electrode work function to the reduction potentials of PCBM. There is no literature reported about the cathode metal effect on hybrid solar cells. To examine the effect of different metal cathodes, 50 nm of Ca, Mg, silver (Ag), or Au were evaporated on top of 50wt% Si NCs/P3HT hybrid solar cells which were pre-annealed at 150 °C for 120 minutes in a glove box. Finally, 100 nm of Al was evaporated on top of the different metal cathode devices to protect the reactive electrodes. Figure 4-7 shows device performance as a function of metal work function under AM 1.5D one sun condition. Figure 4-7a shows that the V_{oc} is quenched by the high work function metals. Si NCs/ P3HT devices with low work function metals (Ca and Mg) had a V_{oc} close to 0.8 V which was similar to devices with Al contacts. This implies that the V_{oc} is determined by the energy difference between the conduction band (CB) of Si NCs and the HOMO of P3HT when the metal work function is smaller than the electron affinity of Si NCs. If the work function is larger than the electron affinity of Si NCs, the V_{oc} of hybrid devices is strongly affected

by the metal work function and was determined by the energy difference between the HOMO of P3HT and metal Fermi level.

Figure 4-7b indicates that the devices with Al cathodes have the highest I_{sc}. Although Si exhibits strong quantum confinement at the nanoscale, the CB and valence band (VB) shift are not equal and the ratio of the CB to VB shifts is 1/2 from experimental results [29]. Therefore, 3-5 nm Si NCs should have a higher CB than bulk Si, but we do not expect the shift to more than 0.2 eV (the band gap is ~ 1.5 eV from photoluminescence measurements) in CB. Compared to devices with Al cathodes, devices with Mg or Ca cathodes have a lower I_{sc} because electrons in Si NCs need to overcome higher barriers to be injected into the cathodes. The reason high work function metals (Ag and Au) result in low currents is not clear. However, the quenching of the V_{oc} provides strong proof that electric fields inside the Si NCs/P3HT hybrid devices may be strongly affected by the metal work function, and this may reduce the efficiency of exciton dissociation and carrier transport. There is slightly a decrease in FF (shown in Figure 4-7c) when low and high work function metals were applied. From these results, Al is the optimal cathode metal for Si NCs/P3HT hybrid devices.

4.5 Conclusion

We have optimized Si NCs/P3HT hybrid devices with annealing post treatments and various cathode metals, and analyzed hole transport in Si NCs/P3HT hybrid devices. Annealing 50wt% Si NCs/P3HT hybrid solar cells at 150 °C for 120 minutes led to the best PCE. Under AM 1.5D one sun conditions, the best device had 1.47 % PCE with an IPCE of 31% at 500 nm. Hole mobility in the P3HT phase of Si NCs/P3HT devices was enhanced by one order of magnitude upon annealing. The increase in hole mobility suggests an improved crystallinity of the P3HT phase, which accounts for the enhanced solar cell efficiency [10]. Silicon NCs/P3HT hybrid devices performed very differently in different work function metals. By using cathodes with smaller work function than Al, the V_{oc} was determined by the energy difference between the HOMO of P3HT and CB of Si NCs. When the cathodes had larger a work function than Al, the V_{oc} and I_{sc} decreased

rapidly with increasing metal work function. These results are valuable for the optimization of Si NCs/P3HT hybrid solar cells.

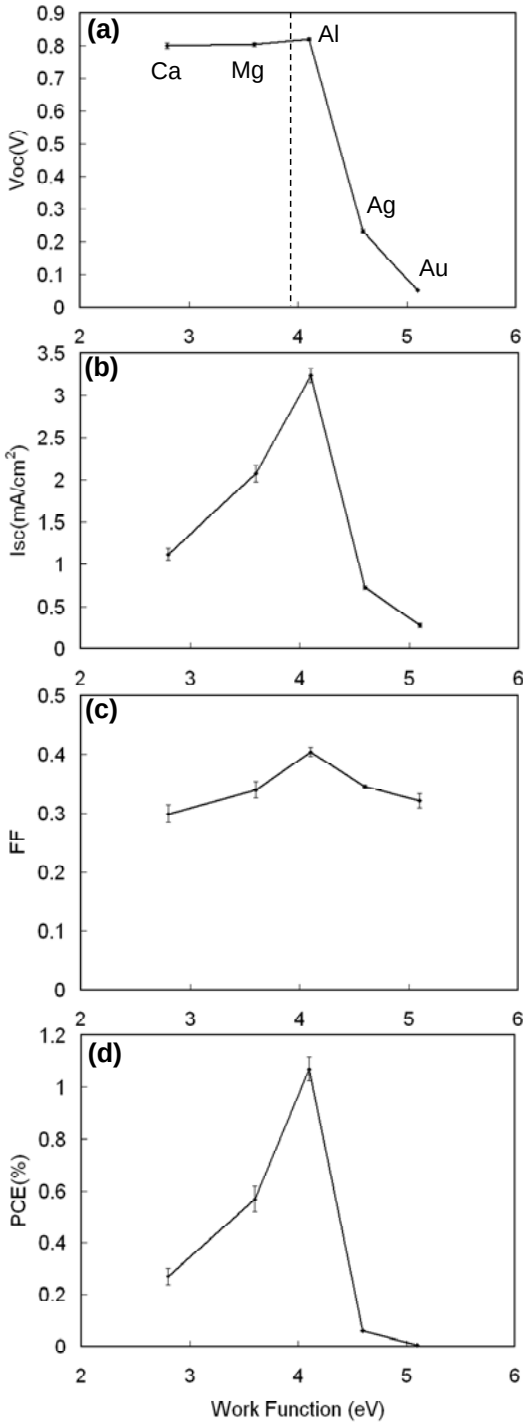

Figure 4-7. Hybrid solar cell performance of 50wt% Si NCs/P3HT with work function metals (Ca, Mg, Al, Ag, Au). The V_{oc} and I_{sc} were strongly affected by the metal work functions. The dashed line represents the CB level of 4 nm Si NCs. Each data point and associated error bar represents an average value and standard deviation from a set of six devices on one substrate.

4.6 References

[1] S. Barth, and H. Bässler, *Phys. Rev. Lett.* **79**, 4445 (1997).

[2] J. J. M. Halls, C. A. Walsh, N. C. Greenham, E. A. Marseglia, R. H. Friend, S. C. Moratti, and A. B. Holmes, *Nature*, **376**, 498 (1995).

[3] G. Yu, J. Gao, J. C. Hummelen, F. Wudi, and A. J. Heeger, *Science*, **270**, 1789 (1995).

[4] W. U. Huynh, J. J.Dittmer, and A. P. Alivisatos, *Science*, **295**, 2425 (2002).

[5] C. B. Murray, D. J. Norris, and M. G. Bawendi, *J. Am. Chem. Soc.* **115**, 8706 (1993).

[6] C. Y. Kwong, W. C. H. Choy, A. B. Djurišić, P. C. Chui, K. W. Cheng, and W. K. Chan, *Nanotech.* **15**, 1156 (2004).

[7] W. J. E. Beek, M. M. Wienk, and R. A. J. Janssen, *Adv. Funct. Mater.* **16**, 1112 (2006).

[8] C. Y. Liu, Z. C. Holman, and U. Kortshagen, *Nano Lett.* **9**, 449 (2009).

[9] L. Mangolini, E. Thimsen, and U. Kortshagen, *Nano Lett.* **5**, 655 (2005).

[10] V. D. Mihailetchi, H. Xie, B. D. Boer, L. J. A. Koster, and P. W. M. Blom, *Adv. Funct. Mater.* **16**, 699 (2006).

[11] V. D. Mihailetchi, J. Wildeman, and P. W. M. Blom, *Phys. Rev. Lett.* **94**, 126602 (2005).

[12] H. Sirringhaus, P. J. Brown, R. H. Friend, M. M. Nielsen, K. Bechgaard, B. M. W. Langeveld-Voss, A. J. H. Spiering, R. A. J. Janssen, E. W. Meijer, P. Herwig, and D. M. de Leeuw, *Nature*, **401**, 685 (1999).

[13] R. J. Kline, *Adv. Mater.* **15**, 1519 (2003).

[14] J. Chang, B. Sun, D. W. Breiby, M. M. Nielsen,T. I. Sölling, M. Giles, I. McCulloch, and H. Sirringhaus, *Chem. Mater.* **16**, 4772 (2004).

[15] C. Y. Kwong, A. B. Djurisic, P. C. Chui, K. W. Cheng, and W. K. Chan, *Chem. Phys. Lett.* **384**, 372 (2004).

[16] Y. Kim, S. A. Choulis, J. Nelson, D. D. C. Bradley, S. Cook, J. R. Durrant , *Appl. Phys. Lett.* **86**, 063502 (2005).

[17] Y. Zhao, G. Yuan, P. Roche, M. Leclerc, *Polymer*, **11**, 2211(1995).

[18] W. U. Huynh, J. J. Dittmer, W. C. Libby, G. L. Whiting, and A. P. Alivisatos, *Adv. Funct. Mater.* **13**, 73 (2003).

[19] V. Gowrishankar, S. R. Scully, A. T. Chan, M. D. McGehee, Q. Wang, and H. M. Branz, *J. Appl. Phys.* **103**,064511 (2008).

[20] Y. C. Huang, Y.C. Liao, S. S. Li, M. C. Wu, C. W. Chen, and W. F. Su, *Sol. Energ. Mat. Sol. C.* **93**, 888 (2009).

[21] G. Li, V. Shrotriya, Y. Yao, and Y. Yang, *J. appl. Phys.* **98**, 043704 (2005).

[22] C. Melzer, E. J. Koop, V. D. Mihailetchi, and P. W. M. Blom, *Adv. Funct. Mater.* **14**, 865 (2004).

[23] S. Lee, G. D. Moon ,and U. Jeong, *J. Mater. Chem.* **6**, 669 (2009).

[24] B. R. Saunders, and M. L. Turner, *Adv. Colloid Interfac.* **138**, 1 (2008).

[25] J. Liu, Y. Shi, and Y. Yang, *Adv. Funct. Maters.* **11**, 420 (2001).

[26] C. M. Ramsdale, J. A. Barker, A. C. Arias, J. D. MacKenzie, R. H. Friend, and N. C. Greenham, *J. Appl. Phys.* **8**, 4266 (2002).

[27] C. J. Brabec, A. Cravino, D. Meissner, N. S. Sariciftci, T. Fromherz, M. T. Rispens, L. Sanchez, and J. C. Hummelen, *Adv. Funct. Maters.* **11**, 374 (2001).

[28] V. D. Mihailetchi, P. W. M. Blom, J. C. Hummelen, and M. T. Rispens, *J. Appl. Phys.* **94**, 6849 (2003).

[29] T. van Buuren, L. N. Dinh, L. L. Chase, W. J. Siekhaus, and L. J. Terminello, *Phys. Rev. Lett.* **80**, 3803 (1998).

Chapter 5

Hybrid Solar Cells from MDMO-PPV and Silicon Nanocrystals

5.1 Overview

Bulk heterojunction solar cells consisting of 3-5 nm silicon nanocrystals (Si NCs) and poly [2-methoxy-5-(3',7'-dimethyloctyloxy)-1,4-phenylenevinylene] (MDMO -PPV) have been fabricated from solution processes. The properties of composite Si NCs/MDMO-PPV devices were studied as a function of the Si NCs/MDMO-PPV weight ratio. The hybrid cells of 58wt% 3-5 nm Si NCs/MDMO-PPV showed a power conversion efficiency of 0.49% under simulated one sun AM 1.5 direct illumination (100 mW/cm^2). Compared to the composite film of Si NCs and poly-3(hexylthiophene), the low efficiency of Si NCs/MDMO-PPV may result from the lower hole mobility and narrow absorption spectrum of MDMO-PPV. The energy band alignment of Si NCs and MDMO-PPV may also be one of the factors limiting device efficiency.

5.2 Introduction

To achieve high hybrid solar cell performance, the electron and hole mobilities should be balanced and optimized. In 1996, Greenham *et al.* reported the first polymer/nanocrystals solar cell made by dispersing cadmium selenide (CdSe) or cadmium sulfide (CdS) nanocrystals into the conjugated polymer poly (2-methoxy, 5-(2′-ethyl) - hexyloxy-*p*-phenylenevinylene) (MEH-PPV) [1]. The best efficiency cells were obtained by using 90wt % (weight ratio) nanocrystals, which corresponds to a volume ratio around 50%. Although the best cell had an efficiency lower than 0.1% under AM 1.5 one sun condition and 10% external quantum efficiency at 514 nm, this indicates that

there is significant exciton dissociation at the polymer/nanocrystals interface. Greenham *et al.* also indicated that long ligands on nanocrystal surfaces impeded the transport of carriers between nanocrystals. They attributed low external quantum efficiency to the poor electron transport due to the hopping mechanism and trapping problem at the dead-end of nanocrystals. The poor electron transport was improved by introducing CdSe nanorods into the polymer matrix [2]. The number of electron hopping events can be reduced by using nanorods, which also have the advantage of high surface-area-to-volume ratio for exciton dissociation.

However, the improvement of solar cell performance in hybrid zinc oxide (ZnO) / poly [2-methoxy-5-(3',7'-dimethyloctyloxy)-1,4-phenylenevinylene] (MDMO-PPV) devices was not observed by replacing ZnO nanocrystals with ZnO nanorods [3]. Beek *et al.* indicated that solar cell preparation of ZnO nanorods/MDMO-PVV was not as easy as that for ZnO NCs/MDMO-PPV. Koster *et al.* found that the performance of ZnO NCs/MDMO-PPV solar cells was not limited by electron mobility, but rather hole transport in the polymer [4]. Beek *et al.* replaced the MDMO-PPV with poly-3(hexylthiophene) (P3HT) which had a hole mobility higher than MDMO-PPV [5]. The hybrid device made by P3HT and ZnO NCs was not as efficient as MDMO-PPV because of coarse mixing and film roughness. Those results imply that the hybrid solar cell performance is not only limited by the carrier transport but also the compatibility of nanocrystals and polymer, which may cause the morphology difference.

Here, we investigate the application of MDMO-PPV polymer in Si NCs-based hybrid solar cells. Compared to the Si NCs/P3HT solar cells, an increase of open-circuit voltage (V_{oc}) is expected due to the fact that MDMO-PPV has a lower highest occupied molecular orbital (HOMO) level than P3HT. The hybrid solar cells of Si NCs/MDMO-PPV are made by a solution process and the hole mobility of MDMO-PPV is measured by replacing the cathodes with the high work function metal.

5.3 Experimental

3-5 nm silicon nanocrystals were used as an electron acceptor in the MDMO-PPV polymer matrix. Silicon nanocrystals of 3-5 nm were synthesized by flowing and dissociating the precursor, silane (SiH_4), through a non-thermal plasma reactor under vacuum conditions [6]. 5% SiH_4/Helium (He) was mixed with argon (Ar) and hydrogen (H_2) and passed through a one-half inch outer diameter quartz tube around which a pair of copper electrodes was wrapped. The flow rates of 5% SiH_4/He, Ar and H_2 are 33, 150, and 6 standard cubic centimeters per minute (SCCM), respectively. 135 Watts of radio frequency power at 13.56 MHz was applied to the electrodes. The Si NCs were collected downstream of the plasma on a stainless steel mesh. After Si NC deposition finished, the Si NCs were weighed and transferred to an air-tight vial (Sigma-Aldrich, 27150-U) inside a nitrogen-purged glove bag (oxygen level < 25 ppm). The vial was transferred into a glove box (oxygen and moisture level < 1 ppm) immediately after the sealing process. 18mg/0.5ml MDMO-PPV (M_w>500 $kgmol^{-1}$, American Dye Source, INC., ADS104RE) in 1,2-dichlorobenzene (DCB, ACROS) was stirred overnight at 55 °C on a hot plate. 2.5 ml DCB was added to the vial with Si NCs on mesh in a glove box and taken out for sonication for 10 minutes. A syringe was used to transfer the cloudy Si NCs solution into the vial containing MDMO-PPV solution. The final concentration of MDMO-PPV was around 6 mg/ml. After mixing Si NCs and MDMO-PPV, the blend solution was taken out again for sonication before device fabrication.

Hybrid solar cells of Si NCs and MDMO-PPV were prepared by spin-coating the blend solution of Si NCs and MDMO-PPV onto poly(3,4- ethylenedioxy thiophene)/poly(styrenesulfonate) (PEDOT:PSS, Baytron P VP Al 4083 grade from H. C. Starck) coated indium tin oxide (ITO, Delta Technologies, LTD**,** CG-51IN-1507) on glass substrates at 700 rpm for 60 seconds in a glove box. ITO coated glass substrates were cleaned and coated with 50 nm PEDOT:PSS in ambient conditions before device fabrication. The PEDOT:PSS coated substrates were subsequently dried in the fume hood on a hot plate at 130 °C for 5 minutes to remove any residual water inside the film. A 100 nm of aluminum (Al) electrode was evaporated under vacuum conditions (< $2x10^{-6}$ Torr). The composite film thickness of Si NCs/MDMO-PPV was around 50 nm and the active

area of hybrid device was 0.046 cm^2. For hole-transport-only devices, the Al electrodes were replaced with gold (Au) electrodes.

Hydrosilylation of Si NCs was conducted by attaching the organic molecule, 1-dodecene, onto the Si NC surface. A solution of 5:1 mesitylene/1-dodecene was dried with molecular sieves and degassed by bubbling nitrogen for 30 minutes in Schlenk line. The Si NCs were collected on the mesh downstream of the plasma. The mesh was transferred into the test tube and sealed with a cap inside a glove bag. The solution 5:1 mesitylene/1-dodecene after degassing was transferred to the tube until the mesh was immersed by the solution on the Schlenk line. The tube including the solution and mesh was sonicated for 10 minutes to release Si NCs into the solution from the mesh. The cloudy solution after sonication was heated at 220 °C for two hours in the Schlenk line. After the reaction, the cloudy solution became clear, because the Si NCs are soluble in the mesitylene.

5.4 Results and Discussion

5.4.1 Si NCs/MDMO-PPV Solar Cells

The photovoltaic performance of the hybrid devices was studied as a function of Si NCs/MDMO-PPV weight ratio under AM 1.5 direct (AM 1.5D) one sun condition (100 mW/cm^2) and shown in Figure 5-1. The surface of Si NCs is terminated by hydrogen which cannot provide the solubility in DCB. Therefore, the Si NC concentration higher than 58wt% cannot be manufactured due to the non-continuous film formed by the agglomeration of Si NCs. Figure 5-1a indicates that the V_{oc} increases up to 0.94 V after integrating Si NCs within the polymer matrix. When 3-5 nm Si NCs were mixed with P3HT, the V_{oc} of Si NCs/P3HT devices was around 0.8 V [7]. The HOMO level of MDMO-PPV is around 0.2 eV lower than that of P3HT. The 0.15 V increase in V_{oc} is expected due to the lower HOMO level of MDMO-PPV. Short-circuit current (I_{sc}) also increases with increasing Si NC concentration (Figure 5-1b) due to increase of exciton dissociation area. The excitons generated inside the polymer have a higher probability to diffuse to the Si NC interface at high concentration of Si NCs than at low concentration.

The fill factor (FF) increases slightly with the Si NCs/MDMO-PPV ratio. As a result, the calculated power conversion efficiencies (PCEs) follow the trends observed in I_{sc} and FF, and are shown in Figure 5-1d. The best solar cell performance (Figure 5-2) was obtained for 58wt% Si NCs /MDMO-PPV. This cell had a 0.49% PCE and a FF of 0.4, with I_{sc} of 1.29 mA/cm^2 and V_{oc} of 0.95 V.

The incident-photon-to-current-conversion efficiencies (IPCEs) for the different Si NC weight ratio devices are shown in Figure 5-3. Such devices are most efficient near 500 nm, where the highest IPCE is 17% for 58wt% Si NCs/MDMO-PPV. The surface morphology of 58wt% Si NCs/MDMO-PPV film is shown in Figure 5-4. Due to the agglomeration of Si NCs, the film roughness varies in the micrometer range and the rough morphology may be one of main factors limiting the hybrid solar cell efficiency. To measure the absorption spectrum of Si NCs/MDMO-PPV film (Figure 5-5), the composite film was spin-coated on PEDOT:PSS coated quartz substrates, which are UV transparent and do not affect the Si absorption spectrum. MDMO-PPV has a strong absorption band between 400-600 nm. By increasing the Si NC concentration in the composite film, the UV absorption starts to increase due to the incorporation of Si NCs. There is a significant increase in absorption between 600 nm- 800 nm, but it is likely not due to the real absorption of Si NCs. As mentioned above, a non-uniform morphology was observed by the SEM and agglomeration was caused by the non-passivated Si NCs. Due to this agglomeration, the absorption between 600-800 nm is caused by scattering effects. This can be validated by the fact that the IPCE spectrum does not show significant increase in the region between 600-800 nm after Si NCs are incorporated into the MDMO-PPV film. This is a reminder that the non-uniform morphology also affects the accuracy of absorption measurement between 300-600 nm.

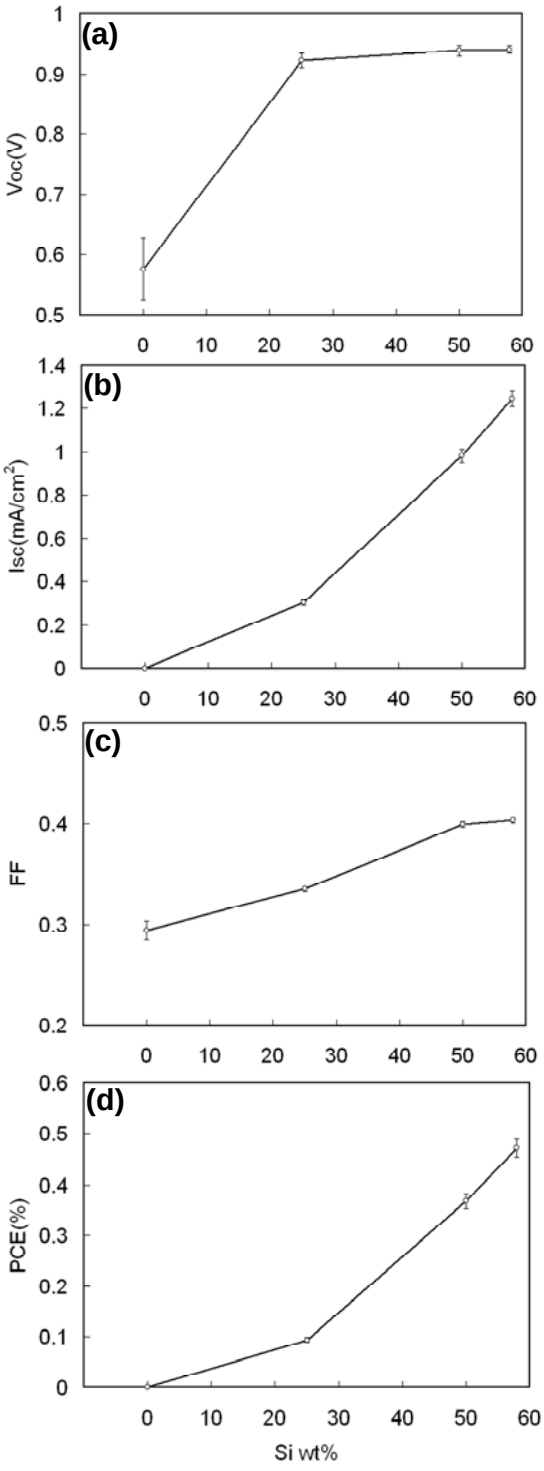

Figure 5-1. Hybrid solar cell performance based on 3-5 nm Si NCs/MDMO-PPV with different Si NCs/MDMO-PPV weight ratios under AM 1.5D one sun illumination. When silicon concentration is higher than 58wt%, a continuous film cannot be formed and devices cannot be measured. Each data point and associated error bar represents an average value and standard deviation from a set of six devices on one substrate. Defective devices, which comprise less than 6% of all devices, are ignored.

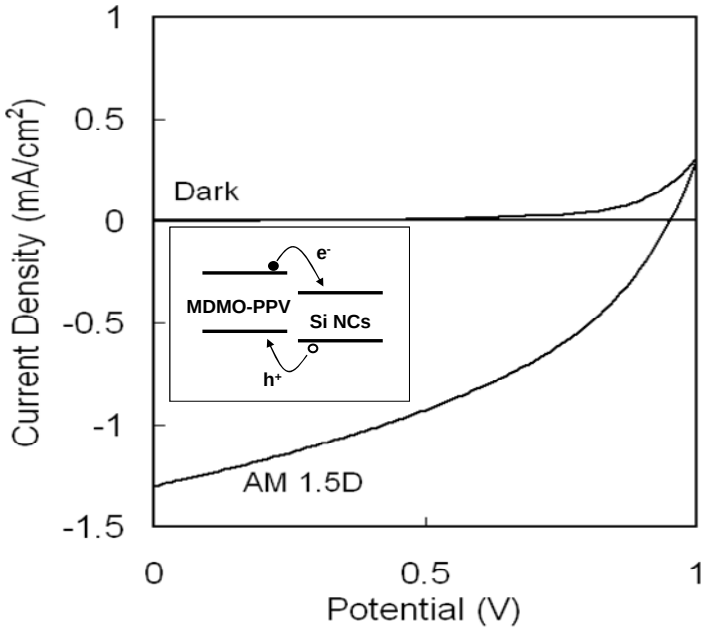

Figure 5-2. Current-voltage characteristic (I-V) of a 58wt% 3-5 nm Si NCs/MDMO-PPV solar cell (main plot). The I-V characteristic of the hybrid device was recorded under 100 mW/cm^2 AM 1.5D conditions and shows 0.49% PCE and a fill factor of 0.4 with 1.29 mA/cm^2 short circuit-current density and 0.95 V open-circuit voltage. The inset shows the energy band alignment of the Si NCs and MDMO-PPV.

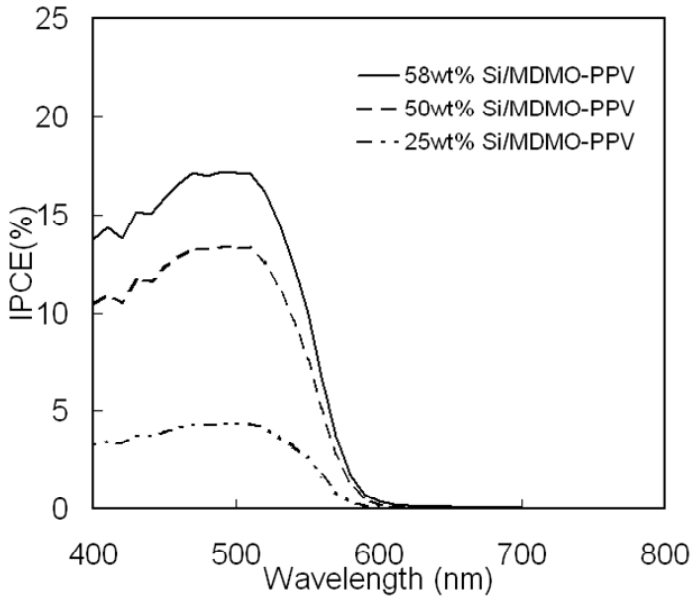

Figure 5-3. Incident photon-to-current-conversion efficiency spectrum of 3-5 nm Si NCs/MDMO-PPV solar cell at different Si weight concentrations. 58wt%, 50wt% and 25wt% Si NCs are represented with solid, dash, and dash-dot lines, respectively.

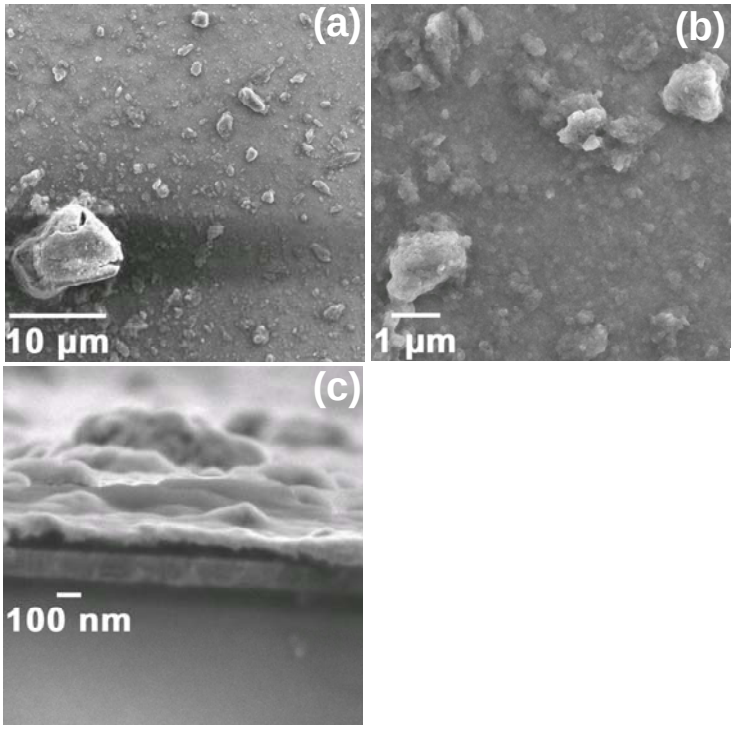

Figure 5-4. SEM images of 58wt% 3-5 nm Si NCs/MDMO-PPV films. (a) and (b) Top-view images at different magnification show Si NC agglomerates larger than 10 μm in size. (c) A cross-section shows film thickness variation which may deteriorate solar cell efficiency.

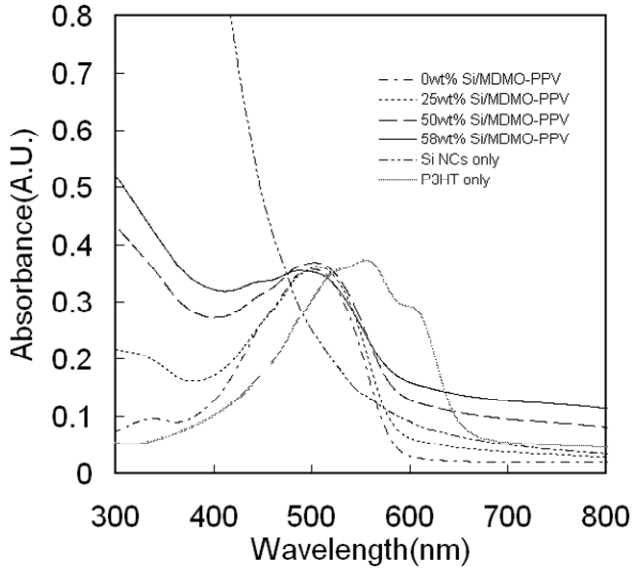

Figure 5-5. Room-temperature optical absorption spectra of Si NCs-only, 0wt%, 25wt%, 50wt% and 58wt% 3-5 nm Si NCs/MDMO-PPV, and P3HT-only films on quartz. The absorbance of the Si NCs/MDMO-PPV film below 400 nm is due to Si NCs.

5.4.2 Hole Transport in Si NCs/MDMO-PPV Solar Cells

The hole mobility of MDMO-PPV in the Si NCs/MDMO-PPV blend structure can be obtained from the dark current-voltage curve by using high work function metals to block the electron transport, resulting in hole-transport-only devices [8]. The characteristic of the dark current is space-charge-limited-current (SCLC) and the hole mobility of MDMO-PPV can be obtained by fitting the experimental data with SCLC equation [9, 10]. In this section, the hole-transport-only device was fabricated by evaporating Au as the top electrodes on the 58wt% Si NCs/MDMO-PPV composite film. The Fermi level of Au is very close to the HOMO level of MDMO-PPV (5.1-5.3 eV), such that Au strongly suppresses electron injection into Si NCs.

Figure 5-6 shows the experimental dark current-voltage curve of Si NCs/MDMO-PPV hole-transport-only device. The SCLC of a hole-transport-only device is approximated by the following

$$J_h = \frac{9}{8}\varepsilon_0\varepsilon_r\mu_h \exp(0.891\gamma_h\sqrt{\frac{V_{\text{int}}}{L}})\frac{V_{\text{int}}^{\ 2}}{L^3} \tag{5.1}$$

where J_h is the hole current-density (J), ε_0 is the vacuum permittivity (8.85×10^{-12} A s V^{-1} m^{-1}), ε_r is the relative dielectric constant, μ_h is the zero-field hole mobility, γ_h is the field activation factor, and L is the thickness of the active layer. The internal voltage drop, denoted as V_{int}, was corrected for the built-in voltage (V_{bi}) and the voltage drop (V_{Rs}). The V_{int} can be expressed as

$$V_{\text{int}}=V-V_{\text{bi}}-V_{\text{Rs}} \tag{5.2}$$

where V_{bi} is the built-in voltage drop caused by the work function difference between electrodes, and V_{Rs} is voltage drop from series resistance of the substrates. The experimental data in Figure 5-6 was fitted using Equation 5.1, and the result is shown in solid line in Figure 5-6. The V_{bi} between PEDOT:PSS and Au is 0.1 V and the series resistance of PEDOT:PSS on ITO is 75 Ω in our study. To measure the series resistance of the substrates, Al contacts were deposited on the PEDOT:PSS coated ITO substrates. The resistance was obtained from the I-V curve. The relative dielectric constant ε_r of MDMO-PPV is taken as 2.1[4].

At room temperature, a zero-field hole mobility of 7.9×10^{-11} $m^2V^{-1}s^{-1}$ with $\gamma_h = 5.52 \times 10^{-4}$ $(mV^{-1})^{0.5}$ was obtained in the 58wt% Si NCs/MDMO-PPV film. This hole mobility is close to the hole mobility measured in the ZnO NCs/MDMO-PPV film [4]. The non-uniform distribution of Si NCs was observed in SEM, so the variation in hole mobility between devices is expected. The average hole mobility out of five devices is 8.63×10^{-11} $m^2V^{-1}s^{-1}$. The control device of MDMO-PPV only had a hole mobility of (1.5×10^{-9} – 2.6×10^{-10}) $m^2V^{-1}s^{-1}$ ($\gamma_h = 0$). The presence of Si NCs in the MDMO-PPV matrix affects the hole transport.

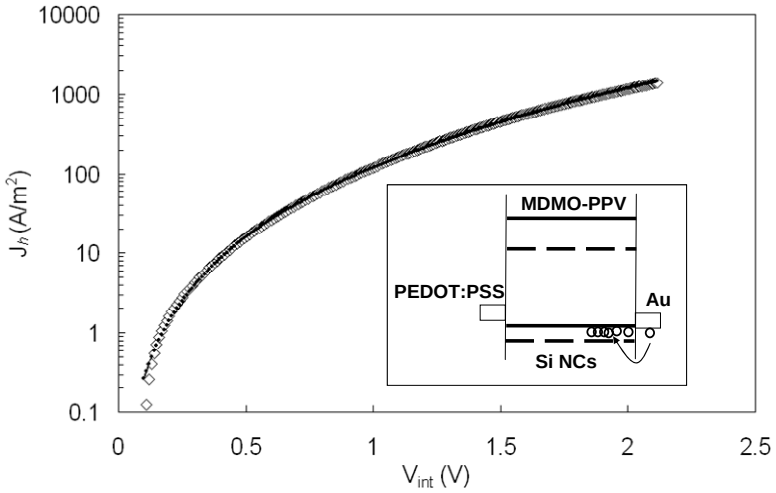

Figure 5-6. Current density-voltage characteristic of a hole-transport-only device of 58wt% 3-5 nm Si NCs/MDMO-PPV (active layer thickness around 50 nm). Measurement data are represented with diamonds. The solid line represents the fit to the measurement data from Equation 5.1. The inset shows the hole-transport-only device configuration of the Si NCs and MDMO-PPV.

5.4.3 Comparing Si NCs/MDMO-PPV with Si NCs/P3HT Solar Cells

Photoluminescence (PL) from Si NCs could provide us with more information about the band-shift of Si NCs. To measure the PL signal from Si NCs, the surface states of Si NCs need to be passivated with certain organic molecules. The surface of Si NCs is terminated by hydrogen and hydrosilylation of Si-H_x surface with 1-dodecene as the organic ligand was used to passivate Si NCs surface in this study. The PL spectrum (Figure 5-7) was measured in the integrating sphere using a USB spectrometer. The valance band (VB) and conduction band (CB) shift are not equal in quantum-confined Si NCs. The estimate of Si NC band gap can be expressed as [11]

$$E_{gap} = 3\Delta CB + 1.1 \ (eV) \tag{5.3}$$

where the VB shift is equal to twice CB band shift. The luminescence peak of 3-5 nm Si NCs is around 850 nm (1.46 eV). The VB level of 850 nm-luminescent Si NCs is around 0.24 eV lower than that of bulk Si (5.1 eV) and the HOMO level of MDMO-PPV is around 5.3 eV. From the calculation results, the Si NCs which have a luminescence peak above 850 nm may not have efficient hole injection from Si NCs to MDMO-PPV, which can cause exciton recombination. Compared to the Si NCs/P3HT solar cells, the HOMO of P3HT is about 0.2 eV higher than MDMO-PPV. Most of 3-5 nm Si NCs can have a preferable hole injection from Si NCs to P3HT. This may be one of reasons why the I_{sc} of Si NCs/MDMO-PPV cells is lower than Si NCs/P3HT cells. From an absorption perspective, the P3HT has a broader absorption (400-650 nm) than MDMO-PPV (400-600 nm). The exciton generation in P3HT may be more efficient than in MDMO-PPV under AM 1.5 conditions. As described above, the hole mobility in the SiNCs/P3HT film ($1.1x10^{-9}$ $m^2V^{-1}s^{-1}$) is around one order of magnitude higher than the Si NCs/MDMO-PPV film ($8.63x10^{-11}$ $m^2V^{-1}s^{-1}$). The low mobility can cause hole-electron recombination before the hole reaches the anode. Those reasons may explain why the Si NCs/MDMO-PPV cells are not as efficient as the Si NCs/P3HT cells.

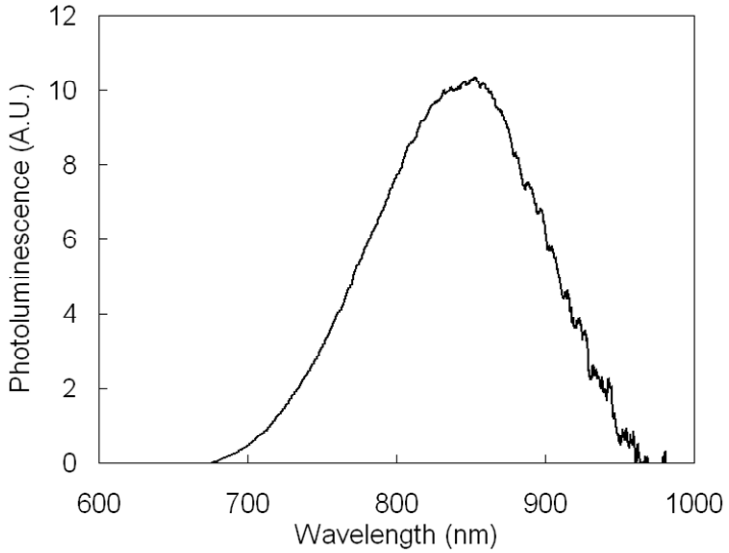

Figure 5-7. Photoluminescence spectrum of 3-5 nm Si NCs after hydrosilylation of Si-H_x by 1-dodecene. Si NCs exhibit photoluminescence between 670 to 950 nm.

5.5. Conclusion

We have studied Si NCs/MDMO-PPV solar cells fabricated by spin-coating blends of Si NCs and MDMO-PPV onto PEDOT:PSS coated ITO glass substrates. The hybrid solar cell based on 58wt% Si NCs/MDMO-PPV provides an estimated efficiency of 0.49% PCE under AM 1.5D one sun conditions with a IPCE of 17% near 500 nm. Due to the surface properties of SiH_x groups on the Si NCs causing insolubility in DCB, the device with concentrations higher than 58wt% cannot be fabricated. The non-uniform morphology of Si NCs/MDMO-PPV, shown in SEM, can also limit the device efficiency. Although Si NCs/MDMO-PPV devices have a V_{oc} of 0.95 V which is larger than the V_{oc} of similar Si NCs/P3HT devices (0.8V), the Si NCs/MDMO-PPV devices do not perform as well as Si NCs/P3HT devices. This can be explained by several reasons: The absorption spectrum of P3HT (400-650 nm) is broader than MDMO-PPV (400-600 nm) so that there will be more photons absorbed in P3HT than MDMO-PPV under AM 1.5 conditions. Half of all 3-5 nm Si NCs may not be able to provide sufficient energy band alignment for exciton dissociation because the HOMO level of MDMO-PPV is around 0.2 eV lower than that of P3HT. The exciton recombination probability in Si NCs/MDMO-PPV devices may be higher than in Si NCs/P3HT devices. Also, the hole mobility measurements on Si NCs/MDMO-PPV devices show that MDMO-PPV has a hole mobility lower than P3HT. If we assume the electron mobility between Si NCs in Si NCs/P3HT and Si NCs/MDMO-PPV devices is same, the hole mobility of polymers can be a limiting factor for solar cell efficiency.

5.6 References

[1] N. C. Greenham, X. Peng, and A. P. Alivisatos, *Phys. Rev. B*, **54**, 17628 (1996).

[2] W. U. Huynh, J. J. Dittmer, and A. P. Alivisatos, *Science*, **295**, 2425 (2002).

[3] W. J. E. Beek , M. M. Wienk , M. Kemerink , X. N. Yang , R. A. J. Janssen , *J. Phys. Chem. B*, **109**, 9505 (2005).

[4] L. J. A. Koster, W. J. van Strien, W. J. E. Beek, P. W. M. Blom, *Adv. Funct. Mater.* **17**, 1297 (2007).

[5] W. J. E. Beek , M. M. Wienk, and R. A. J. Janssen, *Adv. Funct. Mater.* **16**, 1112 (2006).

[6] L. Mangolini, E. Thimsen, and U. Kortshagen, *Nano Lett.* **5**, 655 (2005).

[7] C. Y. Liu, Z. C. Holman, and U. Kortshagen, *Nano Lett.* **9**, 449 (2009).

[8] V. D. Mihailetchi, H. Xie, B. D. Boer, L. J. A. Koster, and P. W. M. Blom, *Adv. Funct. Mater.* **16**, 699 (2006).

[9] V. D. Mihailetchi, J. K. J. van Duren, P. W. M. Blom, J. C. Hummelen, R. A. J. Janssen, J. M. Kroon, M. T. Rispens, W. J. H. Verhees, and M. M. Wienk, *Adv. Funct. Mater.* **13**, 43 (2003).

[10] P. W. M. Blom, M. J. M. de Jong, and M. G. van Munster, *Phys. Rev. B*, **55**, R656 (1997).

[11] T. van Buuren, L. N. Dinh, L. L. Chase, W. J. Siekhaus, and L. J. Terminello, *Phys. Rev. Lett.* **80**, 3803 (1998).

Chapter 6

A New Solution Process for Silicon Nanocrystals Thin-Film Photovoltaic Devices

6.1 Overview

To reduce the manufacturing cost of silicon thin-film solar cells, we report a new thin-film formation process using silicon nanocrystal (Si NC) suspensions without any attachment, exchange or removal of ligands. A single layer Schottky photovoltaic device consisting of intrinsic Si NCs was fabricated by spin-coating in a glove box. A photovoltaic device based on a sandwich structure of a 250 nm Si NC layer between indium tin oxide and aluminum electrodes was measured under AM 1.5 direct one sun illumination. This device showed a significant photovoltaic response with a power conversion efficiency of 0.02%, a fill factor of 0.26, short circuit-current density of 0.148 mA/cm^2 and open-circuit voltage of 0.51 V.

6.2 Introduction

Long-term emission of CO_2 and other green-house gases into the atmosphere can cause undesirable climate change and many would like to reduce the quantity of carbon released from electricity or power generation. The sun delivers approximately 1 gigawatt per square kilometer of energy to the earth's surface — the total solar power hitting the earth is thus almost 10,000 times more power than humans presently consume. From a practical perspective, solar energy can supply the world population with terawatts of power.

Although current commercial silicon solar cells can reach 10-20% power conversion efficiency (PCE), current solar cell manufacturing processes require high temperatures,

vacuum technologies, and high-grade materials, all of which increase cost. As a result, current commercial solar cells remain expensive compared to fossil fuels, around 25-50 cents per kilowatt-hour in the USA [1]. Organic solar cells, which are made from carbon-containing compounds, are usually made in solution so that they can be printed in a process similar to newspaper printing, or sprayed onto surfaces, like paint. Print or spray processing can bring down manufacturing costs by avoiding high temperature and high vacuum methods. However, stability and carrier transport are challenges for organic solar cells. Current solar cells are expected to last at temperatures between -20 and 90 °C for 20-30 years, which organic solar cells may not be able to achieve [2]. The highest carrier mobility in polymer-based organic solar cells is typically on the order of 0.1 cm^2/Vs [3, 4]. Compared to inorganic semiconductors, carrier mobility of organic solar cells is still low.

Nanocrystals not only have the primary advantages of organic materials including solution-processability and tunable absorption, but also retain the broadband absorption and transport properties of traditional photovoltaic materials. Various promising nanocrystals-only solar cells have been reported, including devices which utilize cadmium selenide (CdSe) and cadmium telluride (CdTe) nanorods for heterojunction solar cells [5], as well as lead selenide (PbSe) [6] and lead sulfide (PbS) [7] for Schottky solar cells. These devices were made by spin-coating or dip-coating nanocrystals onto substrates. CdSe/CdTe heterojunction solar cells are air stable devices, and PbSe or PbS Schottky solar cells are infrared harvesting devices which can utilize the broad solar spectrum. Although nanocrystals-only solar cells have shown encouraging efficiencies, cadmium, selenium, and lead are toxic materials which may limit their commercialization for low-cost solar cells. Silicon has dominated the solar cell market since the first crystalline silicon solar cell was reported to have a 6% power conversion efficiency by Chapin in 1954 [8].

Silicon is an abundant and non-toxic material, and is also well-studied in industrial applications. If this conventional material can be used in a novel way (*e.g.* nanocrystal solution processes), the manufacturing cost of silicon-based solar cells may be reduced.

Here, we report a new thin-film formation process which may be applied in silicon-based photovoltaic devices by using solution-processable silicon nanocrystals (Si NCs).

6.3 Experimental

Silicon nanocrystals of 10-20 nm were synthesized by flowing and dissociating the precursor, silane (SiH_4), through a non-thermal plasma reactor under vacuum condition [9]. 5% SiH_4/Helium (He) was mixed with argon (Ar) and passed through a one inch outer diameter Pyrex tube with a copper electrode around it. The flow rate of 5% SiH_4/He and Ar were 35 and 25 standard cubic centimeters per minute (SCCM), respectively. Radio frequency power of 175 Watts was applied to the electrode at 13.56 MHz. The Si NCs were collected downstream of the plasma on stainless steel meshes. After Si NC deposition finished, the Si NCs were weighed and transferred to an air-tight vial (Sigma-Aldrich, 27150-U) inside a nitrogen-purged glove bag (oxygen level < 25 ppm). To test that functional films can be cast from Si NC suspensions, a simple Schottky photovoltaic device was made. Silicon nanocrystal thin-films were fabricated by spin-coating Si NC suspensions onto indium tin oxide (ITO) coated glass substrates in the glove box at 700 rpm for 60 seconds. The device architecture is shown in Figure 6-1. Si NCs were dispersed in 1,2-dichlorobenzene (DCB, ACROS) to form a cloudy solution. The solution concentration was 8mg Si NCs/ml DCB. To obtain the 250 nm Si NC thin film, multi-spin-coating processes were required. To complete the device, 100 nm of aluminum (Al) was deposited on the top of the film as the electrode. The active area of each device was 0.046 cm^2.

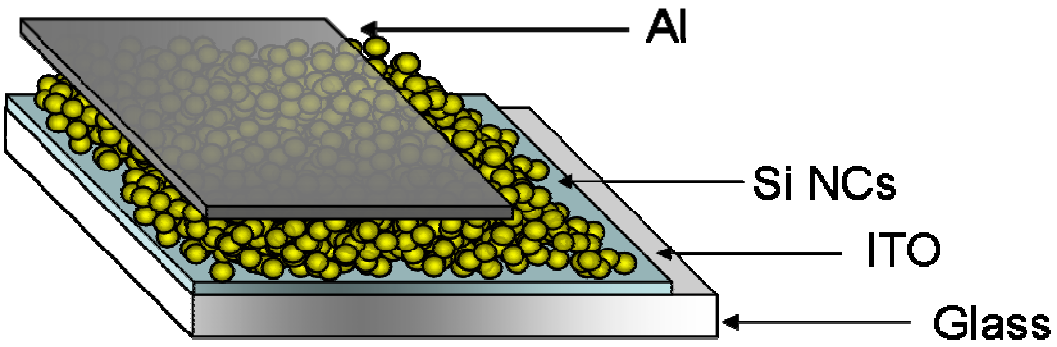

Figure 6-1. The schematic of Si NCs-only photovoltaic device.

6.4 Results and Discussion

Spin-coating of Si NCs suspension from DCB led to a rough and densely packed film, as shown by the scanning electron micrograph (SEM) in Figure 6-2. The rough morphology is expected due to the agglomeration of Si NCs. There were six devices on one substrate; we found that one device short-circuited while the other five devices had similar performance. The current-voltage (I-V) of one device is shown in Figure 6-3a. This device had a 0.02% PCE and a fill factor of 0.26, with short circuit-current density of 0.148 mA/cm^2 and open-circuit voltage of 0.51 V. The incident-photon-to-current-conversion efficiency (IPCE) for the Si NCs-only device is shown in Figure 6-3b. The optical absorption spectrum of Si NCs-only films on the ITO substrate was measured and is displayed in Figure 6-4. The IPCE trends of the Schottky photovoltaic device matched the absorption trend of Si NCs-only film. For most nanocrystal solution processes, the surfaces of nanocrystals are traditionally passivated with certain ligands to provide solubility of nanocrystals in the solvents. After nanocrystal-film formation, the ligands are usually removed to enhance the interaction between nanocrystals. However, Si NCs were found to be stable with DCB without further surface functionalization [10]. This allows Si NCs to become solution-processable immediately after production and also reduces the process cost of ligand attachment, exchange or removal steps.

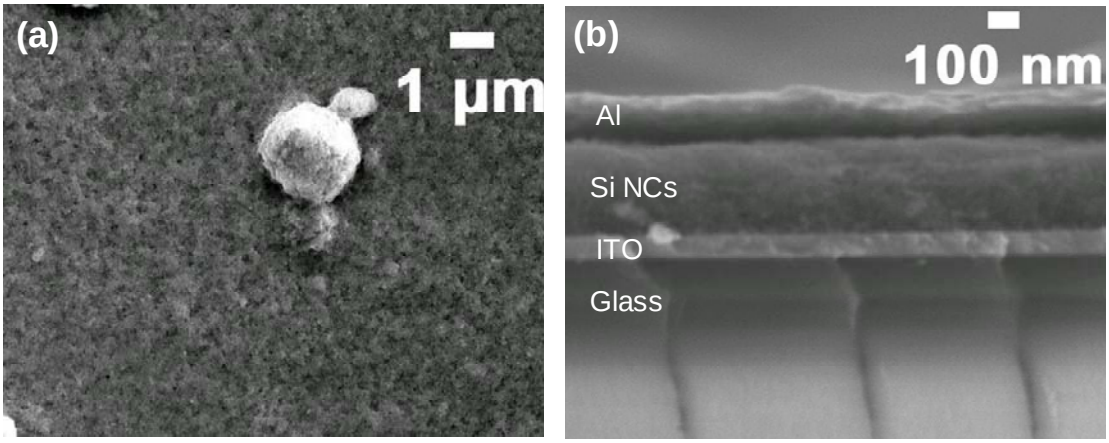

Figure 6-2. SEM of Si NCs-only photovoltaic devices. (a) Top view and (b) cross-section view.

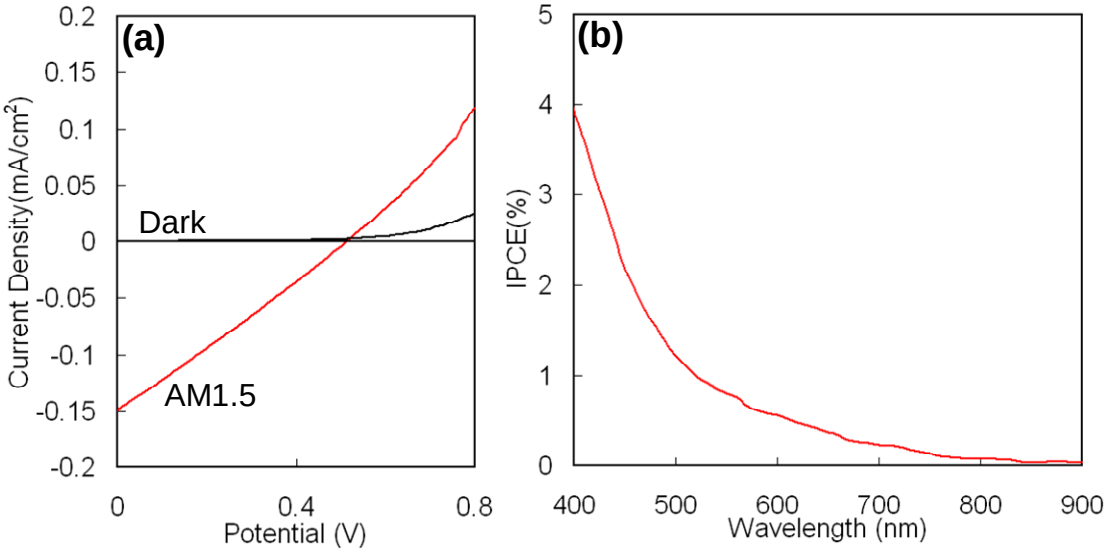

Figure 6-3. (a) Current-voltage characteristic (I-V) of a Si NCs-only photovoltaic device. The I-V characteristic of the device was recorded under 100 mW/cm^2 AM 1.5 direct conditions and shows 0.02% PCE and a fill factor of 0.26 with 0.148 mA/cm^2 short circuit-current density and 0.51 V open-circuit voltage. (b) The IPCE spectrum of the Si NCs-only device.

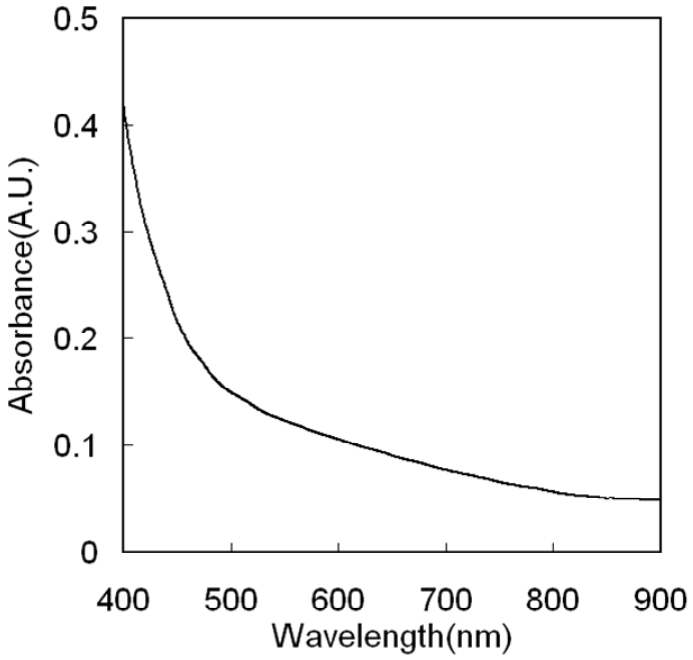

Figure 6-4. Room-temperature optical absorption spectrum of a Si NCs-only film.

6.5 Conclusion

In conclusion, the results of this study demonstrate that this solution process of Si NCs can be a new approach for silicon-based thin-film solar cell fabrication. Compared to the other nanocrystal thin-film formation processes, this process does not involve any attachment, exchange or removal of ligands, which can reduce fabrication steps and cost. The Si NCs-only photovoltaic devices were successfully made by spin-coating Si NC suspensions in a glove box. The film thickness is adjustable by varying the spin-coating times. A single layer of the Schottky photovoltaic device shows a significant photovoltaic response, which indicates that Si NC thin film is continuous without short-circuiting problems. This new process has the potential to be used not only for solar cell fabrication, but also for thin-film transistor manufacturing.

6.6 References

[1] N. S. Lewis, *MRS Bull.* **32**, 808 (2007).

[2] A. Antonio, Ed., S. Hegedus, Ed., *Handbook of Photovoltaic Science and Engineering*, John Wiley and Sons (2003).

[3] J. Chang, B. Sun, D. W. Breiby, M. M. Nielsen, T. I. Sölling, M. Giles, I. McCulloch, and H. Sirringhaus, *Chem. Mater.* **16**, 4772 (2004).

[4] H. Sirringhaus, P. J. Brown, R. H. Friend, M. M. Nielsen, K. Bechgaard, B. M. W. Langeveld-Voss, A. J. H. Spiering, R. A. J. Janssen, E. W. Meijer, P. Herwig and D. M. de Leeuw, *Nature*, **401**, 685 (1999).

[5] I. Gur, N. A. Fromer, M. L. Geier, and A. P. Alivisatos, *Scienc*e, **310**, 462 (2005).

[6] J. M. Luther, M. Law, M. C. Beard, Q. Song, M. O. Reese, R. J. Ellingson, and A. J. Nozik, *Nano Lett.* **8**, 3488 (2008).

[7] K. W. Johnston, A. G. Pattantyus-Abraham, J. P. Clifford, S. H. Myrskog, D. D. MacNeil, L. Levina, and E. H. Sargent, *Appl. Phys. Lett.* **92**, 151115 (2008).

[8] D. M. Chain, C. S. Fuller, and G. L. Pearson, *J. Appl. Phys.* **25**, 676 (1954).

[9] L. Mangolini, E. Thimsen, and U. Kortshagen, *Nano Lett.* **5**, 655 (2005).

[10] C. Y. Liu, Z. C. Holman, and U. Kortshagen, *Nano Lett.* **9**, 449 (2009).

Chapter 7

Conclusion and Future Work

7.1 Conclusion

This thesis has demonstrated a new type of hybrid solar cell using silicon nanocrystals in polymer films. Three groups of Si NCs were successfully synthesized in this thesis: Si NCs 3-5 nm in diameter, 5-9 nm in diameter, and 10-20 nm in diameter, by changing the Si NC residence time and RF power. Bare Si NCs are successfully integrated into polymer films by choosing suitable solvents. Two polymers, P3HT and MDMO-PPV, have been used as electron donors with Si NCs (electron acceptors). The hybrid cells of 50wt% 3-5 nm Si NCs/P3HT showed 1.47% PCE and a FF of 0.47, with I_{sc} of 3.8 mA/cm^2 and V_{oc} of 0.8 V. The hybrid cells made by 58wt% 3-5 nm Si NCs/MDMO-PPV cell had a 0.49% PCE and a FF of 0.4, with I_{sc} of 1.29 mA/cm^2 and V_{oc} of 0.95 V. The control devices made by P3HT only and MDMO-PPV only did not show significant photovoltaic effects. Those results indicate that Si NCs play an important role in these hybrid devices and there is efficient exciton dissociation between polymers and Si NCs.

The I_{sc} and V_{oc} of Si NCs/P3HT hybrid devices can be increased by reducing the Si NCs size due to increasing surface-area-to-volume ratio and quantum confinement. When the Si NC concentration in the polymers increases, I_{sc} rises because excitons are more likely to dissociate in the hybrid devices due to an increase in surface contact between the Si NCs and polymers. The hybrid solar cells made from MDMO-PPV are not as efficient as those created with P3HT since MDMO-PPV has a lower hole mobility and a narrower absorption spectrum than P3HT. The 3-5 nm Si NCs may not have sufficient hole injection into the MDMO-PPV because the HOMO level of MDMO-PPV is around 0.2

eV lower than that of P3HT. This inefficient hole injection may also be one of reasons causing the low efficiency of Si NCs/MDMO-PPV hybrid devices.

Although our hybrid solar cells have a large V_{oc} compared to commercial solar cells, I_{sc} is low due to the low carrier mobility, low absorption coefficient of Si NCs, and non-uniform film morphology. In hybrid solar cells, the hole mobility of the polymer and electron mobility of the nanocrystals are orders of magnitude smaller than in inorganic solar cells, which can increase the recombination probability in the hybrid film. Within the hybrid solar cells, polymers dominate the absorption and exciton generation because Si NCs, which are indirect band gap materials, have little absorption in the visible spectrum compared to polymers. The absorption coefficient of bulk Si is only one-tenth of that of polymers in the visible light region. Due to quantum confinement, the absorption coefficient of Si NCs should be smaller than bulk Si at the same wavelength. Although Si NCs have strong absorption in the UV light region, Si NCs only contribute a little to exciton generation in the device because UV light is only a small portion of the solar spectrum. Additionally, the hybrid film is only 100 nm thick, which limits the absorption from Si NCs. This is the reason why we do not observe significant current generation from Si NCs under UV light illumination. When the Si NCs concentration is too high in the film, exciton generation will be limited due to low concentration of polymer. If the Si NCs concentration is too low, the Si NCs cannot form continuous electron pathways to the electrodes and exciton recombination will increase due to a smaller exciton dissociation area. Therefore, the weight ratio of Si NCs/polymer should be balanced to have good performance.

Hybrid solar cells made with bare Si NCs have non-uniform film morphology with surface roughness in the micrometer range due to the agglomeration of Si NCs. The optimal film thickness of organic devices is around 100-200 nm. This micrometer range roughness could reduce the solar cell efficiency by increasing the film resistivity. The agglomeration of Si NCs also indicates that the distribution of Si NCs inside the film is not uniform, which can reduce the exciton dissociation efficiency.

From our experience making hybrid solar cells, we found that 10-20 nm bare Si NCs can form a stable dispersion in DCB. To verify whether this colloid can be applied in thin

film fabrication, a single layer Schottky photovoltaic device of intrinsic Si NCs was fabricated by spin-coating in a glove box. The Schottky photovoltaic device has a sandwich structure consisting of a 250 nm Si NC layer between ITO and Al electrodes. Under AM1.5D illumination, this device showed photovoltaic effects and did not short-circuit with an active area of 0.046 cm^2. These results demonstrate that bare Si NCs can be used for silicon film fabrication from solution processes without further ligand attachment, change or removal reactions, which are the most common steps for nanocrystal thin-film formation. These preliminary results indicate that Si NCs can be a good electron acceptor in hybrid solar cell applications and Si NC colloids can possibly lower the manufacturing cost of silicon-based thin-film devices.

7.2 Future Work

7.2.1 Hybrid Solar Cells

Suggestions for improvement of hybrid solar cells are focused on two aspects, solar cell processing and solar cell materials. For solar cell processing, there are two suggested methods. The first suggestion is to apply a powerful dry sonicator inside the glove box. In our solar cell processes, the main mechanism of breaking agglomerates of bare Si NCs is to sonicate the Si NCs suspension in water bath. If a powerful dry sonication process can be applied inside the glove box, Si NCs can be broken down into smaller agglomerates than by the water bath sonication and also have lower exposure to atmospheric gases. The less Si NC agglomeration there is, the more likely exciton dissociation will occur due to a higher interfacial area between the Si NCs and polymers. The second suggestion is to modify bare Si NC surfaces with weak bonding ligands which can be removed at low temperature. For example, on CdSe nanocrystals researchers can replace long ligands with short ones, such as pyridine. Pyridine can provide CdSe NCs with solubility in certain solvents and can be removed at a low temperature, around 120 °C [1]. If weak bonding ligands can be found for Si NCs, the film morphology of Si NCs/P3HT films can be improved and Si NCs can be distributed uniformly inside the P3HT, which can provide more exciton dissociation area.

From a materials aspect, there are three suggested methods to increase the efficiency of hybrid solar cells by changing the nanocrystal properties. The first method is to use Si NCs smaller than 3-5 nm. Preliminary results show that the I_{sc} and V_{oc} can be changed by changing Si NC size. If the Si NC size can be smaller than 3-5 nm, the solar cell efficiency should increase by increasing the I_{sc} and V_{oc}. According to the performance of Si NCs/polymer hybrid solar cells, polymers dominate absorption and exciton generation, and Si NCs are only electron transport mediators. The second method is to expand the absorption spectrum of hybrid devices by using nanocrystals with a strong absorption coefficient or narrow band gap. Germanium-silicon alloy (Ge-Si) nanocrystals may have good electrical properties and strong visible absorption properties from the incorporation of Ge. Additionally, Ge-Si NCs have been successfully synthesized by flowing SiH_4 and Germane (GeH_4) through a nonthermal plasma in our group [2]. To verify this concept, a 3/8 inch tube was used for Ge-Si NC synthesis. The recipes for Ge-Si synthesis are shown in Table 7-1, and the Ge/Si ratio was determined by the SiH_4/GeH_4 flow rate. XRD spectra (Figure 7-1a) of 23%, 37% and 50% Ge/Si NCs show the (111), (220), and (311) diffraction peaks of diamond cubic Ge-Si for all samples. There is a significant (111) peak shift when the germanium flow rate increases. A 50wt% (50%Ge/Si) NCs/P3HT hybrid solar cell was made and showed the photovoltaic effect under AM 1.5D one sun illumination. The I-V curve of this device before and after annealing is shown in Figure 7-1b. These preliminary results show that Ge-Si NCs are a possible candidate for hybrid solar cell applications. More studies need to be conducted by adjusting the Ge-Si NC size and concentration to understand whether the decrease of V_{oc} is from the incorporation of Ge.

The third method is to increase the V_{oc} by using high conduction band level nanocrystals. The V_{oc} is determined by the energy difference between the HOMO level of the polymer and the conduction band level of the Si NCs. If Si NCs can be doped with a small portion of carbon (C) atoms, the C-doped Si NCs may have a wider band gap than intrinsic Si NCs. Carbon doped Si NCs may be able to be made by adding methane (CH_4) into the Si NC synthesis recipes. It may be possible to manipulate the conduction band

level of the nanocrystals by changing the doping ratio. The doping ratio can be adjusted by changing the CH_4 flow rate.

100% SiH_4 (SCCM)	10%GeH_4/Ar (SCCM)	Ar (SCCM)	Pressure (Torr)	RF Power (W)	Ge/Si Ratio
1	3	70	3	150	23%
1	6	67	3	150	37%
1	10	63	3	125	50%

Table 7-1. RF plasma synthesis conditions for different ratio of Ge/Si NCs.

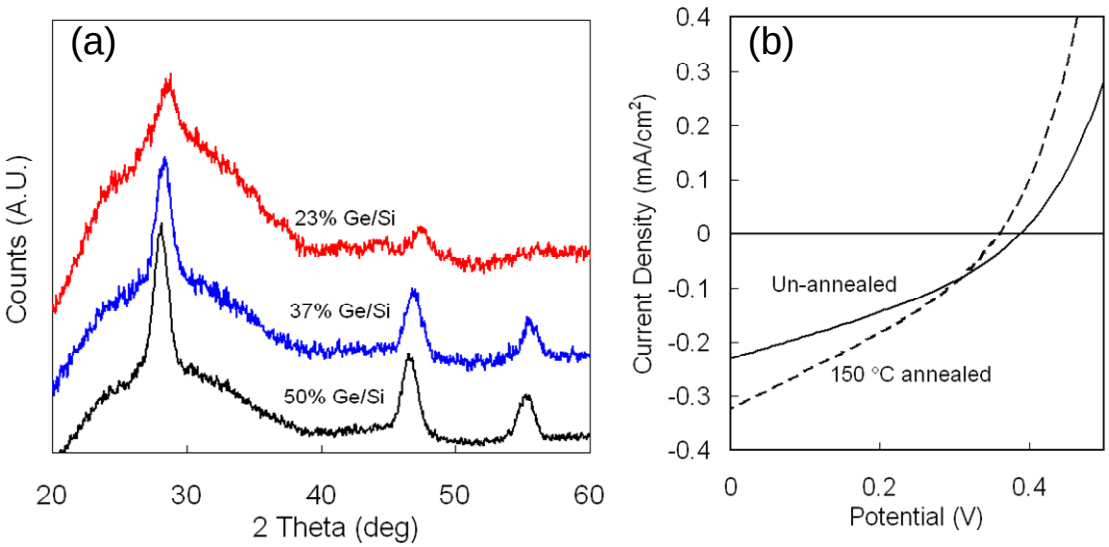

Figure 7-1. (a) XRD spectra of 23%, 37%, and 50% Ge/Si NCs. (This work was done jointly with Rebecca Anthony.) (b) The I-V curve of 50wt% (50%Ge/Si) NCs before and after annealing at 150 °C for 2 hours under AM 1.5D one sun illumination. Un-annealed and annealed devices are represented with solid and dashed lines, respectively.

7.2.2 Nanocrystals-Only Devices

An intrinsic Si NCs-only single layer device has been successfully fabricated by spin-coating a Si NC suspension onto an ITO substrate. There are two suggested devices which can be made by this process. The first one is a Si NCs-based p-n junction solar cell. Doped Si NCs have been successfully made in our group by adding phosphine (PH_3) and diborane (B_2H_6) into the plasma reactor [3]. In that paper, the authors only reported the

photoluminescence change from doped Si NCs to explain the dopant location and effect, but there are no electrical measurements to prove whether the dopants are active inside the Si NCs. To verify the conductivity improvement of doped Si NCs, doped 10-20 nm Si NCs were synthesized and spin-coated on to coplanar-electrode substrates which had three gaps: 5 μm, 10 μm, and 100 μm (Figure 7-2a). The doping concentration was determined by the flow rate ratio of SiH_4/PH_3 or SiH_4/B_2H_6. 5% phosphorus doped and 5% boron doped Si NCs are presented as 5% P doped and 5% B doped, respectively. The doped Si NC film was annealed at 400 °C for 20 minutes. The conductivity (Figure 7-2b) is shown as a function of the film cooling temperature with different dopants after the 400 °C annealing. Results indicate that dopants may be active inside the Si NCs. The doped Si NCs after annealing have higher conductivity than un-annealed doped Si NCs. To achieve p-n junction devices, the pre-annealing process should be utilized to activate the dopants inside the Si NCs. After the dopants inside the Si NCs are activated, the n-type and p-type Si NCs should be spin-coated onto the ITO substrates sequentially. Finally, an electrode should be deposited on the top of the Si NC film to complete the p-n junction device. The second device is the thin-film field-effect-transistor (FET). The architecture of FET is shown in Figure 7-3. Ge NC thin-film FETs were successfully fabricated by my colleague, Zachary Holman. If Si thin-film FETs can be fabricated from the Si NC suspensions, the manufacturing cost of transistors can be reduced in the future.

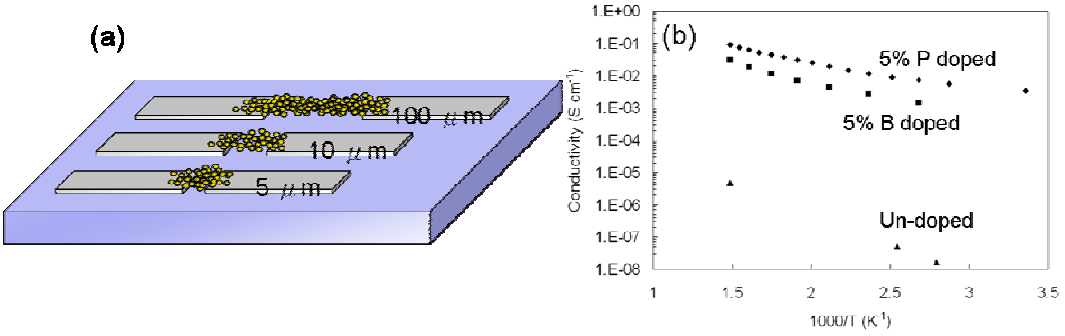

Figure 7-2. (a) Design of conductivity measurement substrate with coplanar-electrodes which had three gaps: 5 μm, 10 μm, and 100 μm. (b) The conductivity of 5% P doped, 5% B doped is shown as a function of the film cooling temperature after the 400 °C annealing. 5% P doped, 5% B doped and un-doped Si NCs are represented with diamond, square and triangle dots, respectively. (This work was done jointly with Ryan Gresback.)

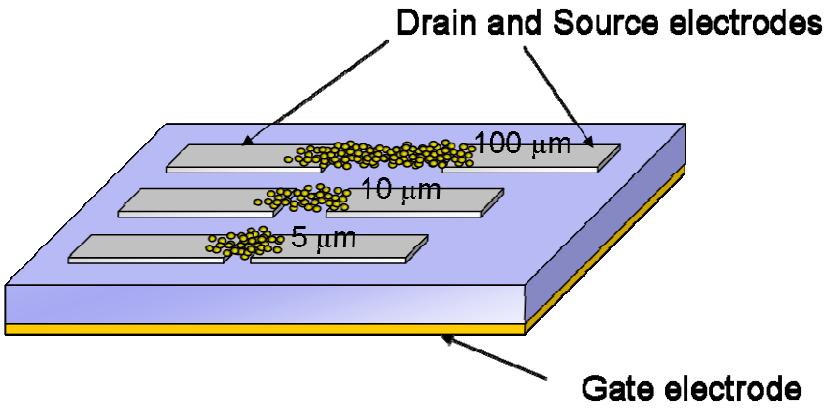

Figure 7-3. Silicon NC thin-film FET device architecture.

7.3 References

[1] W. U. Huynh, J. J. Dittmer, and A. P. Alivisatos, *Science*, **295**, 2425 (2002).

[2] X. D. Pi, and U. Kortshagen, *Nanotechnology*, **20**, 295602 (2009).

[3] X. D. Pi, R. Gresback, R. W. Liptak, S. A. Campbell, and U. Kortshagen, *Appl. Phys. Lett.* **92,** 123102 (2008).

Bibliography

A. A. D. T. Adikaari, D. M. N. M. Dissanayake, R. A. Hatton, and S. R. P. Silva, *Appl. Phys. Lett.* **90**, 203514 (2007).

A. A. R. Watt, D. Blake, J. Warner, E. A. Thomsen, and E. L. Tavenner, *J. Phys. D: Appl. Phys.* **38**, 2006 (2005).

A. Antonio, Ed., S. Hegedus, Ed., *Handbook of Photovoltaic Science and Engineering*, John Wiley and Sons (2003).

A. J. Nozik, *Physica E*, **14**, 115 (2002).

A. Maria, P. Cyr, E. Klem, L. Levina, and E. H. Sargent, *Appl. Phys. Lett.* **87**, 213112 (2005).

A. N. Goldstein, C. M Echer, and A. P. Alivisatos, *Science*, **256**, 1425 (1992).

A. P. Alivisatos, *J. Phys. Chem.* **100**, 13226 (1996).

A. R. Kortan, R. Hull, R. L. Opila, M.G. Bawendi, M. L. Steigerwald, P.J. Carroll, and L. E. Brus, *J. Am. Chem. Soc.* **112**,1327 (1990).

A. Watt, E. Thomsen, P. Meredith, and H. Rubinsztein-Dunlop, *Chem. Commun.* **20,** 2334 (2004).

B. O'regan, and M. Grätzel, *Nature*, **353**, 737 (1991).

B. R. Saunders, and M. L. Turner, *Adv. Colloid Interfac.* **138**, 1 (2008).

C. B. Murray, D.J. Norris, and M.G. Bawendi, *J. Am. Chem. Soc.* **115**, 8706 (1993).

C. J. Brabec, A. Cravino, D. Meissner, N. S. Sariciftci, T. Fromherz, M. T. Rispens, L. Sanchez, and J. C. Hummelen, *Adv. Funct. Maters.* **11**, 374 (2001).

C. Kittel, *Introduction to Solid State Physics*, John Wiley & Sons, (2005).

C. M. Ramsdale, J. A. Barker, A. C. Arias, J. D. MacKenzie, R. H. Friend, and N. C. Greenham, *J. Appl. Phys.* **8**, 4266 (2002).

C. Melzer, E. J. Koop, V. D. Mihailetchi, and P. W. M. Blom, *Adv. Funct. Mater.* **14**, 865 (2004).

C. Y. Kwong, A. B. Djurisic, P. C. Chui, K. W. Cheng, and W. K. Chan, *Chem. Phys. Lett.* **384**,372 (2004).

C. Y. Kwong, W. C. H. Choy, A. B. Djurišić, P. C. Chui, K. W. Cheng, and W. K. Chan, *Nanotech.* **15**, 1156 (2004).

C. Y. Liu, Z. C. Holman, and U. Kortshagen, *Nano Lett.* **9**, 449 (2009).

D. Cui, J. Xu, T. Zhu, G. Paradee, S. Ashok, and M. Gerhold, *Appl. Phys. Lett.* **88**, 183111 (2006).

D. M. Chain, C. S. Fuller, and G. L. Pearson, *J. Appl. Phys.* **25**, 676 (1954).

D. Vanmaekelbergh, and P. Liljeroth, *Chem. Soc. Rev.* **34**, 299 (2005).

E. Arici, N. S. Sariciftci, and D. Meissner, *Adv. Funct. Mater.* **13**, 165 (2003).

G. Lanzani, L. Rossi, S. Stagira, S. D. Silvestri, and F. Garnier, *Opt. Mater.* **9** , 445 (1998).

G. Li, V. Shrotriya, Y. Yao, and Y. Yang, *J. appl. Phys.* **98**, 043704 (2005).

G.. Yu, J. Gao, J. C. Hummelen, F. Wudl, and A. J. Heeger, *Science*, **270**, 1789 (1995).

H. Sirringhaus, P. J. Brown, R. H. Friend, M. M. Nielsen, K. Bechgaard, B. M. W. Langeveld-Voss, A. J. H. Spiering, R. A. J. Janssen, E. W. Meijer, P. Herwig, and D. M. de Leeuw, *Nature*, **401**, 685 (1999).

H. Sirringhaus, P. J. Brown, R. H. Friend, M. M. Nielsen, K. Bechgaard, B. M. W. Langeveld-Voss, A. J. H. Spiering, R. A. J. Janssen, E. W. Meijer, P. Herwig, and D. M. de Leeuw, *Nature*, **401**, 685 (1999).

H. W. Kroto, J. R. Heath, S. C. O'Brien, R. F. Curl, and R. E. Smalley, *Nature,* **318**, 162 (1985).

http://polymer.matscieng.sunysb.edu/images/js03.gif

http://www.newport.com/Introduction-to-Solar-Radiation/411919/1033/catalog.aspx

I. Gur, N. A. Fromer, C. P. Chen, A. G. Kanaras, and A. P. Alivisatos, *Nano Lett,* **7**, 409 (2007).

I. Gur, N. A. Fromer, M. L. Geier, and A. P. Alivisatos, *Scienc*e, **310**, 462 (2005).

J. Chang, B. Sun, D. W. Breiby, M. M. Nielsen,T. I. Sölling, M. Giles, I. McCulloch, and H. Sirringhaus, *Chem. Mater.* **16**, 4772 (2004).

J. J. M. Halls, C. A. Walsh, N. C. Greenham, E. A. Marseglia, R. H. Friend, S. C. Moratti, and A. B. Holmes, *Nature*, **376**, 498 (1995).

J. Kanicki, and P. Fedorko, *J. Phys. D: Appl. Phys.* **17**, 805 (1984).

J. Liu, Y. Shi, and Y. Yang, *Adv. Funct. Maters.* **11**, 420 (2001).

J. M. Luther, M. Law, M. C. Beard, Q. Song, M. O. Reese, R. J. Ellingson, and A. J. Nozik, *Nano Lett.* **8**, 3488 (2008).

J. Rostalski, and D. Meissner, *Sol. Energy Mater. Sol. Cells*, **61**, 87 (2000).

J. S. Kim, M. Granstrom, R. H. Friend, N. Johansson, W. R. Salaneck, R. Daik, W. J. Feast, and F. Cacialli, *J. Appl. Phys.* **84**, 6859 (1998).

J. Tsukamoto, H. Ohigashi, K. Matsumura, and A. Takahashi, *J. Appl. Phys.* **20**, L127–L129 (1981).

K. W. Johnston, A. G. Pattantyus-Abraham, J. P. Clifford, S. H. Myrskog, D. D. MacNeil, L. Levina, and E. H. Sargent, *Appl. Phys. Lett.* **92**, 151115 (2008).

L. E. Brus, *J. Chem. Phys.* **90**, 2555 (1986).

L. H. Spherling, *Introduction to Physical Polymer Science*, Wiley-interscicenc (2001).

L. J. A. Koster, W. J. van Strien, W. J. E. Beek, P. W. M. Blom, *Adv. Funct. Mater.* **17**, 1297 (2007).

L. Mangolini, E. Thimsen, and U. Kortshagen, *Nano Lett.* **5**, 655 (2005).

M. A. Loi, S. Toffanin, M. Muccini, M. Forster, U. Scherf, and M. Scharber, *Adv. Funct. Mater.* **17**, 2111 (2007).

M. A. Reed, R.T. Bate, K. Bradshaw, W. M. Duncan, W. R. Frensley, J. W. Lee, and H. D. Shih, *J. Vac. Sci. Technol. B*, **4**, 358(1986).

M. Drees, K. Premaratne, W. Graupner, J. R. Heflin, R. M. Davis, D. Marciu, and M. Miller, *Appl. Phys. Lett.* **81**, 4607 (2002).

M. G. Bawendi, P. J. Carroll, W. L. Wilson, and L. E. Brus, *J. Chem. Phys.* **96**, 946 (1992).

M. G. Bawendi, W. L. Wilson, L. Rothberg, P. J. Carroll, T. M. Jedju, M. L. Steigerwald, and L. E. Brus, *Phys. Rev. Lett.* **65**,1623 (1990).

M. L. Chabinyc, R. A. Street, and J. E. Northrup, *Appl. Phys. Lett.* **90**, 123508 (2007).

M. S. A. Abdou, F. P. Orfino, Y. Son, and S. Holdcroft, *J. Am. Chem. Soc.* **119**, 4518 (1997).

N. C. Greenham, X. Peng, and A. P. Alivisatos, *Phys. Rev. B*, **54**, 17628 (1996).

N. S. Lewis, *MRS Bull.* **32**, 808 (2007).

N. S. Sariciftci, D. Braun, C. Zhang, V. I. Srdanov, A. J. Heeger, G. Stucky, and F. Wudl, *Appl. Phys. Lett.* **62**, 585 (1993).

N. S. Sariciftci, L. Smilowitz, A. J. Heeger, and F. Wudl, *Science*, **258**, 1474 (1992).

N. T. Binh, M. Gailberger and H. Bässler, *Synth. Met.* **47**, 77 (1992).

P. W. M. Blom, M. J. M. de Jong, and M. G. van Munster, *Phys. Rev. B*, **55**, R656 (1997).

R. J. Kline, *Adv. Mater.* **15**, 1519 (2003).

R. Rossetti, J. L. Ellison, J. M. Gibson, and L. E. Brus, *J. Chem. Phys.* **80**, 4464 (1984).

R. W. Murray, *Acc. Chem. Res.* **1**, 313 (1968).

S. Adachi, *Optical Constants of Crystalline and Amorphous Semiconductors: Numerical Data and Graphical Information*, Springer, 29 (1999).

S. Barth, and H. Bässler, *Phys. Rev. Lett.* **79**, 4445 (1997).

S. E. Shaheen, R. Radspinner, N. Peyghambarian, and G. E. Jabbour, *Appl. Phys. Lett.* **79**, 2996 (2001).

S. Glenis, G.. Horowitz, G.. Tourillon, and F. Garnier, *Thin Solid Films*, **111**, 93 (1984).

S. Günesa, K. P. Fritz, H. Neugebauer, N. S. Sariciftci, S. Kumar, and G. D. Scholes, *sol. Energy Mater. Sol. Cells*, **91**, 420 (2007).

S. H. Lim, T. G. Bjorklund, F. C. Spano, and C. J. Bardeen, *Phys. Rev. Lett.* **92**, 107402 (2004).

S. Lee, G. D. Moon ,and U. Jeong, *J. Mater. Chem.* **6**, 669 (2009).

S. S. Sun, and N. S. Sariciftci, *Organic Photovoltaics: Mechanisms, Materials, and Devices*, Taylor & Francis, 535 (2005).

S. Schmitt-Rink, D.A.B. Miller, and D.S. Chemla, *Phys. Rev. B*, **35** ,8113 (1987).

T. van Buuren, L. N. Dinh, L. L. Chase, W. J. Siekhaus, and L. J. Terminello, *Phys. Rev. Lett.* **80**, 3803 (1998).

T. Vossmeyer, L. Katsikas, M. Giersig, I. G. Popovic, K. Diesner, A. Chemseddine, A. Eychmueller, and H. Weller, *J. Phys. Chem.* **98**, 7665 (1994).

V. D. Mihailetchi, H. Xie, B. D. Boer, L. J. A. Koster, and P. W. M. Blom, *Adv. Funct. Mater.* **16**, 699 (2006).

V. D. Mihailetchi, J. K. J. van Duren, P. W. M. Blom, J. C. Hummelen, R. A. J. Janssen, J. M. Kroon, M. T. Rispens, W. J. H. Verhees, and M. M. Wienk, *Adv. Funct. Mater.* **13**, 43 (2003).

V. D. Mihailetchi, J. Wildeman, and P. W. M. Blom, *Phys. Rev. Lett.* **94**, 126602 (2005).

V. D. Mihailetchi, P. W. M. Blom, J. C. Hummelen, and M. T. Rispens, *J. Appl. Phys.* **94**, 6849 (2003).

V. Gowrishankar, S. R. Scully, A. T. Chan, M. D. McGehee, Q. Wang, and H. M. Branz, *J. Appl. Phys.* **103**,064511 (2008).

V. Gowrishankar, S. R. Scully, and M. D. McGehee, *Appl. Phys. Lett.* **89**, 252102 (2006).

V. L. Colvin, M. C. Schlamp, and A. P. Alivisatos, *Nature*, **370**, 354 (1994).

W. J. E. Beek , M. M. Wienk , M. Kemerink , X. N. Yang , R. A. J. Janssen , *J. Phys. Chem. B*, **109**, 9505 (2005).

W. J. E. Beek, M. M. Wienk, and R. A. J. Janssen, *Adv. Funct. Mater.* **12**, 1009 (2004).

W. J. E. Beek, M. M. Wienk, and R. A. J. Janssen, *Adv. Funct. Mater.* **16**, 1112 (2006).

W. Krätschmer, L. D. Lamb, K. Fostiropoulos, and D. R. Huffman, *Nature*, **347**, 354 (1990).

W. Ma, C. Yang, X. Gong, K Lee, and A. J. Heeger, *Adv. Funct. Mater.* **15**, 1617 (2005).

W. Martienssen, Ed.; M. D. Lechner, Ed., *Static Dielectric Constants of Pure and Binary Liquid Mixtures*, Landolt-Börstein series, **17**, Supplement to IV/6, Springer (2008).

W. U. Huynh, J. J. Dittmer, and A. P. Alivisatos, *Science*, **295**, 2425 (2002).

W. U. Huynh, J. J. Dittmer, W. C. Libby, G. L. Whiting, and A. P. Alivisatos, *Adv. Funct. Mater.* **13**, 73 (2003).

X. D. Pi, and U. Kortshagen, *Nanotechnology*, **20**, 295602 (2009).

X. D. Pi, R. Gresback, R. W. Liptak, S. A. Campbell, and U. Kortshagen, *Appl. Phys. Lett.* **92,** 123102 (2008).

Y. Bai, Y. Cao, J. Z., M. Wang, R. Li, P. Wang, S. M. Zakeeruddin, and M. Grätzel, *Nat. Mater.* **7**, 626 (2008).

Y. C. Huang, Y. C. Liao, S. S. Li, M. C. Wu, C. W. Chen, and W. F. Su, *Sol. Energ. Mat. Sol. C.* **93**, 888 (2009).

Y. Fang, S. A. Chen, and M. L. Chu, *Synth. Met.* **52**, 261 (1992).

Y. Kim, S. A. Choulis, J. Nelson, D. D. C. Bradley, S. Cook, J. R. Durrant , *Appl. Phys. Lett.* **86**, 063502 (2005).

Y. Ohsawa and T. Saji, *J. Chem. Soc. Chem. Commun.* **10**, 781 (1992).

Y. Zhao, G. Yuan, P. Roche, M. Leclerc, *Polymer*, **11**, 2211(1995).

Z. G. Soos, M. H. Hennessy, and G. Wen, *Chem. Phys.* **227**, 19 (1998).

Appendix

A.1 Copyright Permissions

Chapter 3 has been published as Chin-Yi Liu, Zachary C. Holman, and Uwe R. Kortshagen, "Hybrid solar cells from P3HT and silicon nanocrystals," *Nano Lett*. **9**, 449 (2009). Nano Letters is an American Chemical Society (ACS) journal. The ACS grants copyright permission to students to include in their theses and dissertations their own articles, or portions thereof, that have been published in ACS journals or submitted to ACS journals for publication, The ACS's policy on theses and dissertations can be found at www.pubs.acs.org/page/copyright/permissions.html for proof of permission to include Chapter 3 in this thesis.